Spring 2013

Structural Driving Factors for the Coupled Electron and Proton Transfer Reactions in Mitochondrial Cytochrome BC1 Complex: Binding Geometries of Substrates and Protonation States of Ionizable Amino Acid Side Chains Near Qi and Qo Sites

Bao Linh Tran Nguyen

Follow this and additional works at: https://dsc.duq.edu/etd

Recommended Citation

Nguyen, B. (2013). Structural Driving Factors for the Coupled Electron and Proton Transfer Reactions in Mitochondrial Cytochrome BC1 Complex: Binding Geometries of Substrates and Protonation States of Ionizable Amino Acid Side Chains Near Qi and Qo Sites (Doctoral dissertation, Duquesne University). Retrieved from https://dsc.duq.edu/etd/980

STRUCTURAL DRIVING FACTORS FOR THE COUPLED ELECTRON AND

PROTON TRANSFER REACTIONS IN MITOCHONDRIAL CYTOCHROME BC1

COMPLEX: BINDING GEOMETRIES OF SUBSTRATES AND PROTONATION

STATES OF IONIZABLE AMINO ACID SIDE CHAINS NEAR Qi AND Qo SITES

A Dissertation

Submitted to the Department of Chemistry and Biochemistry

Bayer School of Natural and Environmental Sciences

Duquesne University

In partial fulfillment of the requirements for

the degree of Doctor of Philosophy

By

Bao-Linh Tran Nguyen

May 2013

STRUCTURAL DRIVING FACTORS FOR THE COUPLED ELECTRON AND

PROTON TRANSFER REACTIONS IN MITOCHONDRIAL CYTOCHROME BC1

COMPLEX: BINDING GEOMETRIES OF SUBSTRATES AND PROTONATION

STATES OF IONIZABLE AMINO ACID SIDE CHAINS NEAR Qi AND Qo SITES

By

Bao-Linh Tran Nguyen

Approved February 28th, 2013

_____
Ralph A. Wheeler, Ph.D.
Professor and Chair
Department of Chemistry and Biochemistry
(Committee Chair)

_____
Michael Cascio, Ph.D.
Associate Professor of Chemistry and
Biochemistry
(Committee Member)

_____
Jeffry D. Madura, Ph.D.
Professor of Chemistry and Biochemistry
(Committee Member)

_____
Alberto Striolo, Ph.D.
Associate Professor of Chemical,
Biological & Materials Engineering
University of Oklahoma
(External Reviewer)

_____
David W. Seybert, Ph.D.
Dean, Bayer School of Environmental
and Natural Sciences
Professor of Chemistry and Biochemistry

ABSTRACT

STRUCTURAL DRIVING FACTORS FOR THE ELECTRON COUPLED PROTON

TRANSFER REACTIONS IN MITOCHONDRIAL CYTOCHROME BC1 COMPLEX:

BINDING GEOMETRIES OF SUBSTRATES AND PROTONATION STATES OF

IONIZABLE AMINO ACID SIDE CHAINS NEAR Qi AND Qo SITES

By

Bao-Linh Tran Nguyen

May 2013

Dissertation supervised by Ralph A. Wheeler, Ph.D.

Coupled electron and proton transfer (CEPT) events are fundamental for many

bioenergetic conversions that involve redox reactions. Understanding the details

underlying CEPT processes will advance our knowledge of (1) how nature regulates

energy conversion; (2) our strategies for achieving renewable energy sources; (3) how to

cope with CEPT dysfunction diseases. Studies of the detailed mechanism(s) of CEPT in

biological systems is challenging due to their complex nature. Consequently,

controversies between the concerted and sequential mechanism of CEPT for many

systems remain. This dissertation focuses on the bovine mitochondrial cytochrome bc1

complex. CEPT in the bc1 complex operates by a modified "Q-cycle"(1) and catalyzes

electron transfer from ubiquinol (QH2), to cyt c via an iron sulfur cluster (ISC) and to the

low potential hemes of cyt b, where it reduces ubiquinone (UQ). The electron transfer is

coupled to the translocation of protons across the mitochondrial inner membrane, generating a proton gradient that drives ATP synthesis. Although the Q-cycle is widely accepted as the model that best describes how electrons and protons flow in bc1, detailed binding geometries at the Qo site (QH2 oxidation site) and Qi site (UQ reduction site) remain controversial. The binding geometries play critical roles in the thermodynamic and/or kinetic control of the reaction and protonatable amino acid side chains can participate in the proton transfer. The central focuses of this dissertation are molecular dynamics simulations of cofactor binding geometries near the Qo and Qi sites, calculations of the pKa values of ionizable amino acid side chains implicated in cofactor binding, especially the ISC-coordinated histidines, and implications for the proposed mechanism(s) of CEPT. For the first time, pKa values of the ISC-coordinated histidines are differentiated. The computed pKa values of 7.8±0.5 for His141 and 9.1±0.6 for His161 agree well with experiment (7.63±0.15 and 9.16±0.28). Thus, His161 should be protonated at physiological pH and cannot be the first proton acceptor in the QH2 oxidation. Water mediated hydrogen bonds between substrate models and the protein and water accessibility to the Qo and Qi sites were maintained in simulations, implying that water molecules are likely the proton donors and acceptors.

ACKNOWLEDGEMENT

I have been looking forward to writing this section of my dissertation!

First, I would like to thank my parents. They are two very ordinary Vietnamese who are kind, smart, hardworking and God-fearing; who value tradition and education; with whom I am blessed to have spent the last year of my time in graduate school. To mom and dad: it has truly been an adventure being your second daughter. The journey has been eventful, remarkable, endearing and I cherish every bit of it. Thank you for bring me to life. Thank you for nurturing me physically and mentally. Thank you for teaching me to be kind, hardworking, and fearful of God. Thank you for believing in me, being proud of me, having endless patience with me and loving me unconditionally. I would like to thank my little brother Viet Duc, for his encouragement and his enthusiasm in helping me with scripting and writing codes; my sister Bao Anh and her family, my younger brother Viet Tanh and his family for loving me unconditionally and always being there for me. I would like to thank the people who have come through my life and impacted it in some way during my significant five years of grad school. I would like to thank Garry Chapman Jr. for his support and caring in the early years of my graduate career. I would like to thank my dear friend Candice O'Brien Morvant, who is 1100 miles away and yet manages to support me emotionally. Thanks for checking up on me, watching me for every baby step I take in life and career. It is truly a blessing to have you in my life. I would like to thank Adam Campbell for being the geeky friend that every nerd needs. Your love for quantum mechanics and the wave function is beyond my understanding. "The force is strong with this one" as I often think of you. Also, thanks for giving me

I would like to thank Dr. Alberto Striolo for agreeing to be my outside reader, for meeting up with me while you were in Pittsburgh for the AIChE meeting. Thank for introducing me to the chemical engineering professors with the hope of helping me find a postdoctoral position. I appreciate your generosity. I would like to thank Dr. Michael Cascio for agreeing to be on my committee; for making time to educate me on sequence alignment; for introducing me to one of our guest speakers and practically giving me a chance to have an on-site interview for a postdoctoral position. Thank you for your time and generosity in helping with my science. I would like to thank Dr. Jeffry D. Madura. In my little perfect world, you are my co-advisor. Thank you for your time and patience. Thanks for never kicking me out of your office (I don't know how you do it with the frequency that I visit!). Thanks for allowing me to almost run Tera Station 1 down with my data. Thank you for your books (some of which I don't really want to return but I promise I will). Thanks for asking me to give a short presentation to Montgomery Pettitt when he was here for a talk although it was on such a short notice (less than 24 hours) which was not cool, by the way. However, you are forgiven because that presentation has led to a great postdoctoral opportunity. Thank you for allowing me to pick at your brain, to challenge you and to learn from you. Thank you for nourishing me to be scientifically mature. Most importantly, thank for keeping me sane. (You still owe me a shot of Kraken!)

Last but not least, I would like to thank Dr. Ralph A. Wheeler, my PhD advisor. Without you, none of this work would have happened. Until eternity, I am grateful. You have taught me to think critically, to ask the "good" questions (so "good" that finding the answer is almost always impossible at the moment), and to be persistent in finding

answers. The answers are out there and we have the tools to get them eventually, you say. Thanks for believing in me and my ability when I stopped believing in myself. Thanks for encouraging me when I seem to have no courage left. Thanks for being patient with me when I run out of patience for myself. Thanks for pushing me intellectually as hard as I would go. And thanks for accepting my limits. Thanks for allowing me to sit in your office as we go over the corrections of my dissertation. Thank for dragging me to Subway so I have to eat real food and not just sustain my life on coffee and sugar. You have taught me everything intellectually, professionally and even personally on some aspects of life. I have learned how to talk as a scientist, i.e. almost no absolute statements (I did it!) because there is a possibility with a measurable or computable probability for almost everything, you say. My biggest enlightenment is my acceptance that I will not know everything and I won't try to do everything myself in my perfect ways. I humbly accept that what I know is marginal, compared to what I don't. And I am fine as long as I contribute a few critical pieces to solve the whole puzzle.

TABLE OF CONTENTS

LIST OF FIGURES

LIST OF ABBREVIATIONS AND SYMBOLS

1. Coupled electron and proton transfer: CEPT

2. Electron coupled proton transfer: ECPT

3. Proton coupled electron transfer: PCET

4. Electron transfer: ET

5. Proton transfer: PT

6. Bovine cytochrome bc1 complex: cyt bc1

7. Ubiquinol: QH2

8. Ubiquinone: UQ

9. Semiquinone: SQ

10. Iron-Sulfur Protein: ISP

11. Iron-Sulfur Cluster: ISC

12. Ubiquinol oxidation site: Qo site

13. Ubiquinone reduction site: Qi site

14. Stigmatellin: SMA

15. High and low potential b-type hemes: bH and bL, respectively

16. ATP: Adenosine Triphosphate

17. Molecular Dynamics: MD

18. Constant pH molecular dynamics: CPHMD

19. Replica exchange: REX

20. Free Energy Perturbation: FEP

21. Quantum Mechanics/Molecular Mechanics: QM/MM

CHAPTER 1

COUPLED ELECTRON AND PROTON TRANSFER REACTIONS IN THE

MITOCHONDRIAL CYTOCHROME BC1 COMPLEX

1.1. The origin of the coupled electron and proton transfer reactions

The coupled electron and proton transfer events are fundamental for biological energy

transduction and thus establish a foundation for man-made energy-related systems. It has

been well established that biological systems such as proteins and enzymes utilize energy

through biomass conversion in such a way that light energy is converted into a trans-

membrane electrochemical gradient (proton gradient and electrical potentials) that may

be referred to as the proton-motive force (1, 2). The protonmotive force is then used for

almost all living activities of a cell including ion and metabolite transport, ATP synthesis,

biomolecule synthesis, and cell motility (2-5). All biological energy conversion can be

categorized in two types of events. One event uses the photosynthetic reaction center to

convert energy captured from sunlight into chemical energy that fuels all living activities

in photosynthetic organisms. The second event uses the respiratory chain to convert

energy from food (products directly or indirectly from photosynthesis) to chemical

energy in the form of ATP in non-photosynthetic organisms. Understanding this

phenomenon in great detail is in itself an intellect triumph. Yet, such understanding will

also advance our strategies toward achieving renewable energy sources such as fuel cells

and artificial photosynthesis.

This introduction will provide a general theoretical framework for the coupled electron

and proton transfer (CEPT) reactions before limiting the focus to biological energy

conversion machinery, the mitochondrial cytochrome bc1 complex. There are two broad

classes of the CEPT reaction mechanisms: concerted and sequential. In the concerted reaction, both electron transfer (ET) and proton transfer (PT) occur at the same time in one step (EPT) without a stable intermediate. In the sequential mechanism, the reaction occurs in two steps: an ET followed by a PT (ET/PT), or a PT followed by an ET (PT/ET). In this dissertation, the slash in ET/PT and PT/ET denotes two consecutive events in the sequential mechanism, whereas EPT denotes the concerted ET and PT in one step. The term proton coupled electron transfer (PCET) was first introduced by Meyer in 1981(6) to describe a general reaction that involves both proton transfer and electron transfer events (6-9). Although there is no well-established nomenclature for the sequential and concerted PCET mechanism other than author's definitions, the term PCET often denotes concerted electron-coupled proton transfer (4, 10-12). This dissertation instead uses CEPT for general coupled electron and proton transfer events with no implication of a concerted or sequential mechanism, nor any implication of whether ET is followed by PT or vice versa.
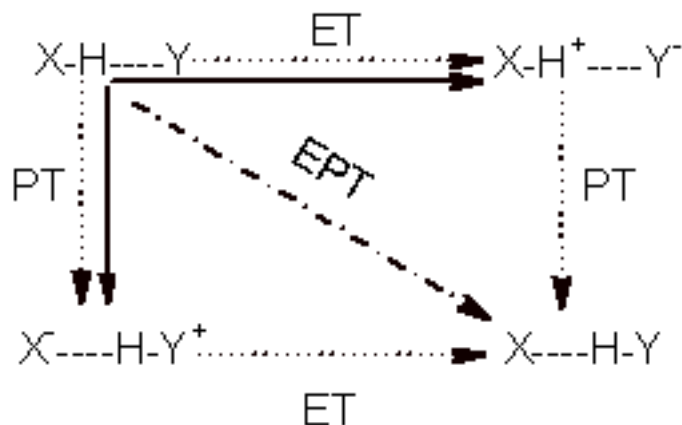
Figure 1.1: A four-state scheme for a coupled one electron and one proton transfer. Initially oxidized and protonated X-H becomes a reduced and deprotonated X, while reduced and unprotonated Y becomes an oxidized and protonated H-Y. Dotted arrows represent the ET and PT events. The bold dotted arrow represents both electron and proton transfer (EPT) in one step to the same site. The solid arrow represents concerted ECPT to different sites.

1.1.1. Theory of coupled electron and proton transfer reactions

Let us consider a simple case of one electron and one proton transfer from X, an electron and proton donor, to Y, an electron and proton acceptor (Figure 1.1). In the initial state, both the electron and proton are on the donor site, reduced and protonated: X-H---Y. In the final state, both electron and proton are on the acceptor site, X is now oxidized and deprotonated: X---H-Y. In a concerted fashion, the electron and proton can transfer to the same site (diagonal arrow EPT) or to different sites (solid arrows). When both the electron and proton transfer to the same site, it is noteworthy to remember that the concerted CEPT mechanism is different from the hydrogen atom transfer (HAT) reaction.

3

HAT is often considered to be a sub-mechanism of concerted ECPT. HAT is beyond the scope of this work and will not be discussed. In a sequential fashion, the electron and proton transfer can occur in an ET-induced PT or a PT-induced ET mechanism. The chemical and physical background of each case will be discussed in detail in the following sections in order to understand discussions regarding bioenergetic activities of the enzyme later in the dissertation.
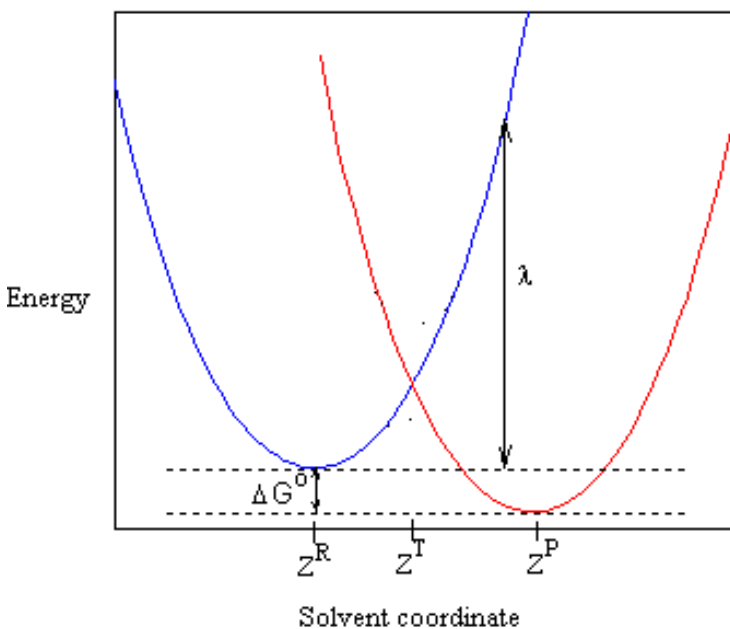
Figure 1.1.1: Marcus theory for electron transfer

Figure 1.1.1 describes the idea of Marcus theory in which an ET occurs over a fixed internuclear distance (10, 13). The electron transfers from the donor to the acceptor upon reorientation of solvent coordinates while the nuclear coordinate remains frozen. When the nuclear coordinate is at the equilibrium for the reactant (Z^R), there exists poor overlapping between the reactant and the product electronic wave functions. At the transition state, the nuclear coordinate is at the intersection (Z^T), thus electronic energies are degenerate for both reactant and product Consequently, optimal overlapping occurs and the electron can tunnel through the energy barrier. After electron transfer, the nuclear

4

coordinate can adopt the equilibrium position for the product well (Z^P). The Marcus theory explains ET in term of the electrostatic contribution from solvent to the free energy. The rate constant and the activation energy for the ET are expressed in the equation below:

$$k = \frac{2\pi}{\hbar} V_{12}^2 \left(4\pi\lambda k_B T\right)^{1/2} \exp\left(\frac{\Delta G^{\mp}}{k_B T}\right)$$

$$\Delta G^{\mp} = \frac{\left(\Delta G^{\circ} + \lambda\right)^2}{4\lambda}$$

where V_{12} is the coupling between diabatic states, λ is the reorganization energy of the inner solute sphere and the outer solvent sphere, $\Delta G^{\ddagger}$ is the activation energy and ΔG° is the free energy of the reaction. In this theory, it is assumed that the solute mode is not coupled to solvent, an assumption that is not applicable for proton transfer because the proton is highly coupled to solvent. Later, Hammes-Schiffer and coworkers developed a theory for the CEPT in terms of the non-adiabatic transitions between the reactant and product electron-proton vibronic states (10), which depend on two variables, the proton and electron coordinates. This theory includes vibrational states involving motion of the proton and can be modeled for the reactant and product electronic states.

1.1.2. Concerted electron coupled proton transfer

Consider a simple concerted one electron coupled one proton transfer reaction, as shown in figure 1.1, in which both the electron and proton are transferred in one kinetic step to the same site without a stable intermediate. Because the electron behaves quantum mechanically, it can be delocalized on either X, the donor, or Y, the acceptor, and thus the reaction can be described in terms of the reactant or product states. The reactant state may be represented as X-H----Y and the product state may be represented by X----H-Y.

Collective solvent coordinate
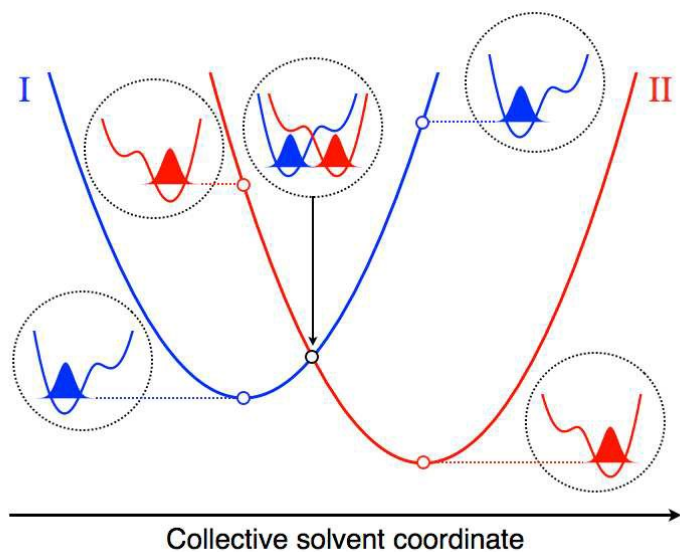
Figure 1.1.2: (Adopted from reference 10) Concerted CEPT is described in term of vibronic states.

The blue and red parabolas describe the electronic states of the reactant (state I) and product (state II), respectively. Concerted CEPT is described in term of reactant (electron delocalized on the donor) and product (electron delocalized on the acceptor) vibronic states. The excited states with much higher energy are neglected in concerted CEPT, thus no stable intermediates are involved.

The reactant (blue, I) and product (red, II) vibronic states are described in terms of both the electronic states and the proton vibrational state that is calculated from that same electronic state. These vibronic states will depend parametrically on other nuclear coordinates. The concerted CEPT mechanism is proposed to proceed in the following order: the system starts in thermal equilibrium; the proton polarizes the solvent and impacts the reactant and product energy surfaces; reorganization of the solvent results in

6

a non-adiabatic transition onto the product surface; final thermal relaxation on the product surface restores equilibrium.

1.1.3. Sequential electron coupled proton transfer

In sequential CEPT, stable intermediates are involved in two ways. First, ET may precede PT. In this case, the reactant state will have predominantly X-H----Y character, the intermediate will be represented by X-H$^+$----Y$^-$ and the product state will have predominantly X----H-Y character. In the second case, PT precedes ET. In this case, the reactant state will be predominantly X-H----Y, the intermediate will be represented by X$^-$ ----H$^+$-Y and the product state will be predominantly X----H-Y. In either case, it is generally assumed that the first proton/electron transfer step is irreversible, i.e., if the proton transfers first, it stays long enough for the electron to arrive at the final state. This assumption can be true if the first transfer step (PT) is downhill in energy or the second transfer step (ET) is faster than the reverse step for the first transfer. In biological systems, both the separate ET and PT steps are generally uphill in energy (14, 15). Thus, the intermediate may not have a long enough lifetime for the second transfer event (ET) to complete the CEPT reaction. With that being said, the remaining question is whether ET or PT is faster. Typically, for similar activation energies, the PT rate constant is much higher than that for ET (8). However, in proteins, PT often requires multiple intermediate steps including a network of water molecules connected through hydrogen bonds between donors and acceptor (16, 17). Moreover, the dynamics of mobile water in the interior of a protein is much different than that in bulk solvent. Consequently, it can take a much longer time to complete a PT than an ET reaction (18).

1.1.4. Sequential versus concerted proton transport via a water hydrogen bond network

For a concerted PT in protein, the system spends most of the time waiting for a reorientation that leads to the formation of the hydrogen bond network, immediately followed by a delocalized soliton transfer, in which all proton transfer events occur at the same time along the hydrogen bond network (19). This process should be very fast. In contrast, a sequential "gated" PT in protein will require a water hydrogen bond network to form prior to a localized charge transfer via a single hydrogen bond along the network. This reorientation contributes to the activation energy. It is unclear at the moment whether the long distance proton transport in many proteins, including the mitochondrial cytochrome bc1 complex, is a gated sequential or concerted mechanism.

In summary, any detectable intermediate(s) will provide proof for a sequential CEPT reaction. On the other hand, the lack of any detectable intermediates(s) cannot be used as proof for a concerted mechanism. Providing evidence for a concerted reaction remains challenging especially for such reactions in biological systems. Most reasonable evidence often comes from studies of the energetics of charge transfer reactions. Redox potential and pKa values are often experimentally measured or computationally modeled to indicate that a single proton transfer or a single electron transfer is thermodynamically unstable, whereas a proton transfer in concert with an electron transfer is more thermodynamically favorable (20). Even with such evidence, it is still debatable whether CEPT reactions in enzymatic systems truly occur by a concerted mechanism.

1.2. Electron coupled proton transfer in the mitochondrial cytochrome bc1 complex

1.2.1. The mitochondrial electron transport chain
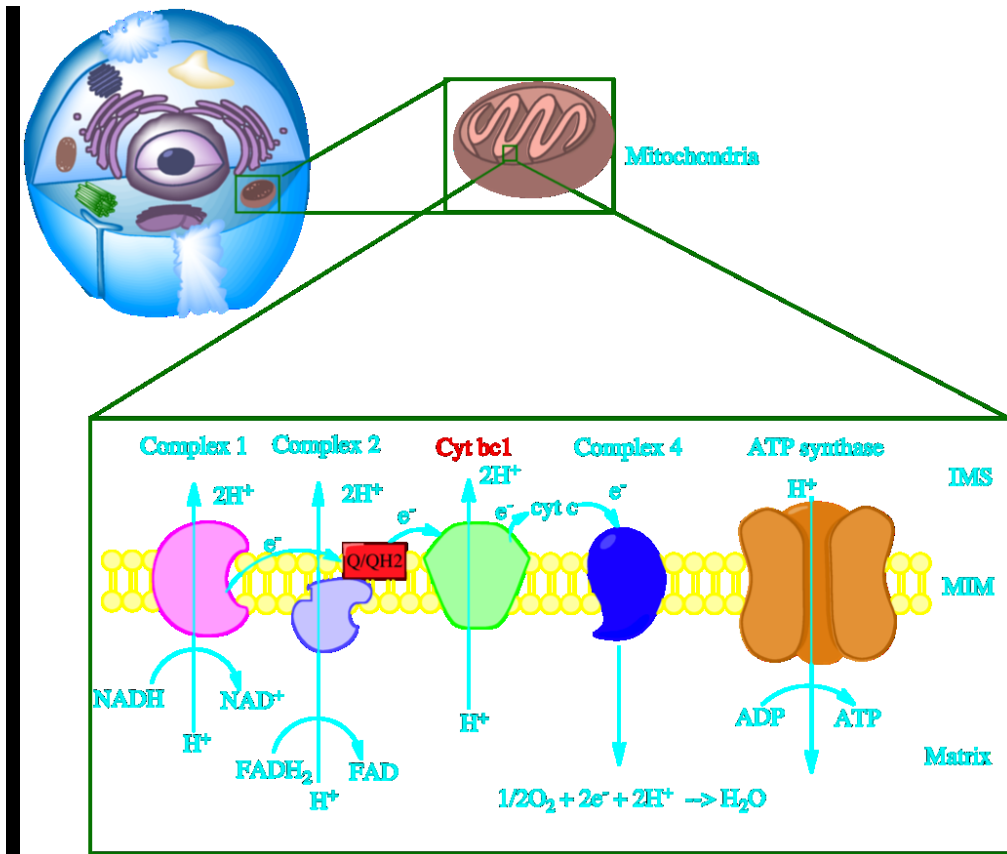
Figure 1.2.1: The mitochondrial electron transport chain

The mitochondrial electron transport chain with multiple protein complexes catalyzes electron coupled proton transfer reactions across the mitochondrial inner membrane.

The mitochondrial electron transport chain is located in the inner mitochondrial membrane of eukaryotes. It consists of four protein complexes (complexes 1 to 4) that catalyze electron transfer reactions coupled to proton transport across the inner

membrane. These complexes also function to convert the redox potential into electrochemical potential and a transmembrane proton gradient that drives ATP synthesis. The coupled electron and proton transfer (CEPT) event is fundamental for energy conversion processes in biological systems. The chemical processes underlying CEPT are basically oxidation and reduction reactions. Understanding the detailed mechanism(s) of CEPT processes in respiration will advance (1) our knowledge of how nature regulates energy conversion efficiently; (2) our strategies for achieving renewable energy sources such as fuel cells, solar cells, artificial photosynthetic and energy conversion devices; (3) our response to mitochondrial dysfunction diseases such as neurodegenerative diseases, myocardial ischemia/reperfusion, and bone and skeletal diseases. For decades, however, studies of the detailed mechanisms of CEPT in biological systems have faced many challenges due to the complex nature of macromolecules. Consequently, the concerted (electron-proton transfer simultaneously) or sequential (electron transfer following by proton transfer) nature of CEPT underlying many systems remains controversial. Moreover, the redox dependent conformational changes and proton exchange paths remain unclear. This dissertation focuses on how the cytochrome bc1 complex, complex 3, binds electron transfer cofactors prior to catalyzing CEPT reactions in the intermediate step of the mitochondrial Electron Transport Chain (ETC) (Figure 1.2.1). Working with the other complexes shown in Figure 1.2.1, the cyt bc1 complex converts the redox potential into an electrochemical gradient and a protonmotive force across the inner membrane that drives ATP synthesis.

1.2.2. Structure and functions of the bovine mitochondrial cytochrome bc1 complex
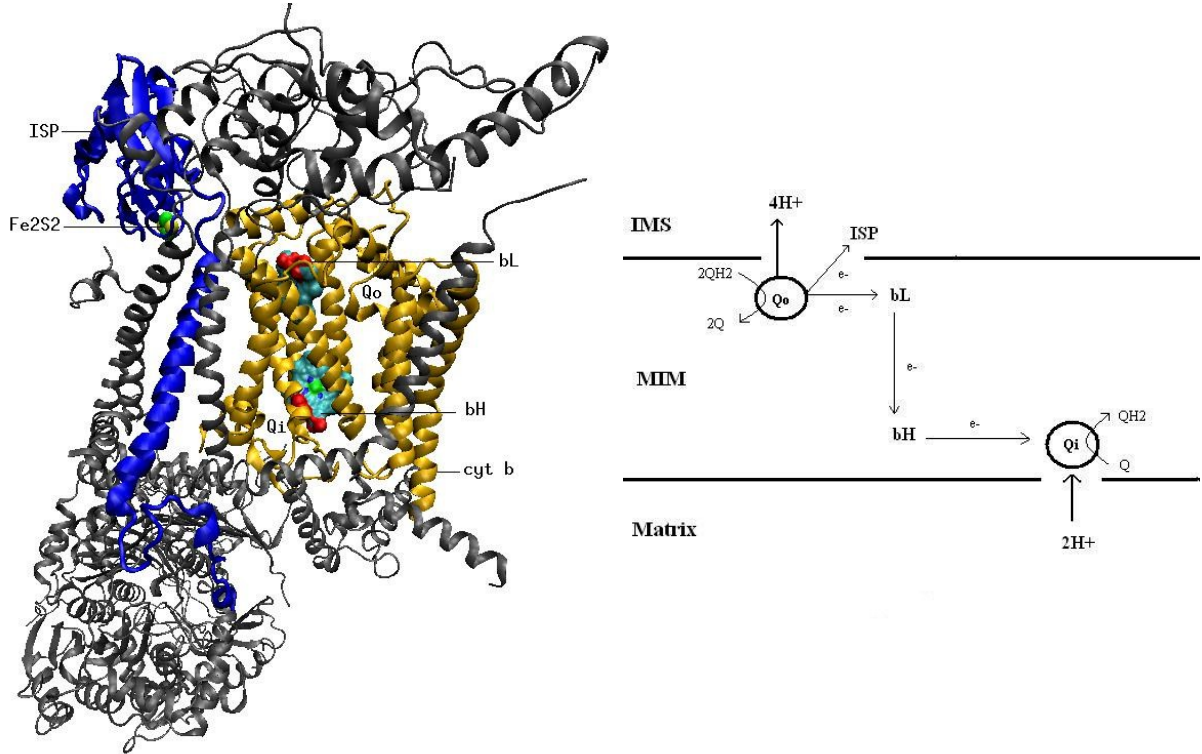
Figure 1.2.2: The core catalytic subunits of the cytochrome bc1 complex and the Q-cycle

The core catalytic subunits of the cytochrome bc1 complex span the mitochondrial inner membrane (MIM). The cytochrome b subunit is shown in gold and the iron-sulfur protein (ISP) is shown in blue. Fe2S2 denotes the iron-sulfur cluster of the Rieske ISP, located near the inner membrane space (IMS). bL and bH denote the locations of the low potential and high potential b-type hemes, respectively, near the catalytic centers Qo and Qi. The Q-cycle schematically describes how electrons and protons flow in the cytochrome bc1 complex. (Figure is made from PDB code 1PP9 using VMD.)

The cytochrome bc1 complex (hereafter cyt bc1 complex) is commonly found in prokaryotes, most bacteria, and in the mitochondria of eukaryotes. In algae and higher plants, there exists a cyt bc1 complex analogue, the cytochrome b6f complex. They are both essential proteins for respiratory and photosynthesis electron transport, coupled to ATP production across all organisms (1). The cyt bc1 catalytic center in all species involves three subunits: cyt b, which has two metal centers, high and low potential hemes bH and bL respectively; cytochrome c1 with a metal center, heme c; and the Rieske Iron-Sulfur Protein (ISP) subunit with an iron sulfur cluster (ISC)(1, 2). These metal centers provide electron transfer bridges between the ubiquinone (UQ) oxidation and ubiquinol (QH2) reduction sites and cyt c. The binding site of QH2 to the cyt bc1 complex is referred to as the Qo (electron out) site and that of UQ is the Qi (electron in) site. They are both located in cytochrome b. Figure 1.2.2 shows the catalytic subunit cytochrome b with the relevant metal centers.

1.2.3. Malfunctions of cyt bc1 and their consequences

Because of its function as an electron transfer protein, the cyt bc1 complex is also a major source of reactive oxygen species (ROS) (21, 22). It is possible for a semiquinone (SQ) intermediate radical to be formed when electrons shuttle through UQ/QH2 and the metal centers (21), or when the bifurcated reaction at the Qo site is disrupted (21, 23). This radical is reactive and will react with any oxygen species (O_2 or H_2O) nearby to form ROS that can harm the cells. Under normal conditions, the efficiency of cyt bc1 surpasses any bypass reactions that could cause wasteful electron transfer. Additionally, the cyt bc1 complex's conformational dynamics ensure that reactive SQ intermediates are shielded from oxygen species by maximizing efficiency in electron transfer to cyt c. General

defects in the function of the mitochondrial cyt bc1 complex result in shutting off the electron transfer chain (ETC) and, ultimately, cell death. In particular, functional defects caused by inhibitors at the Qo site not only disrupt the ETC, but also result in ROS production. It is believed that the ROS are commonly found in oxidatively stressed cells, resulting in apoptosis induction (24). Therefore, any defect in the bifurcated electron transfer process at the Qo site likely causes ROS production in mitochondrial cytochrome bc1 (24-26). Naturally, the cyt bc1 complex is a desirable target for anti-biotic (26), anti-fungal (27), anti-malaria, and anti-pneumonia therapeutics (28-30).

1.3. Tale of the Q-cycle: what it does and doesn't do in the cytochrome bc1 complex

The cyt bc1 complex catalyzes the bifurcated electron transfer from ubiquinol to the high potential cytochrome c and to the low potential cytochrome b, where the electron reduces ubiquinone in two turnovers to give a ubiquinol. These electron transfer events are coupled to the translocation of protons across the mitochondrial inner membrane, generating a proton gradient that drives ATP synthesis. Mitchell suggested that this type of proton coupled electron transfer reaction operated by a prototypical "Q-cycle".
In 1976, it was Mitchell's brilliant idea to use the Q-cycle (31) (Figure 1.2.2) to explain how electrons and protons are transferred in the cyt bc1 complex corresponding to the net chemical reaction:

$$Q + 2cyt.c + 4H^+ \leftrightarrow QH_2 + 2cyt.c^+ + 2H^+ \quad (1)$$
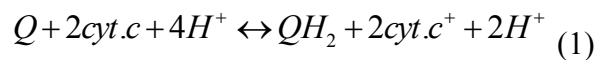
The Q-cycle describes a bifurcated electron transfer mechanism in which a QH2 molecule is oxidized to generate two electrons at the Qo site. The first electron is transferred to the high potential cyt c via the ISC. The second electron is transferred to

13

the low potential cytochrome b via heme bH and bL, where it reduces UQ to a stable semiquinone; when the second QH2 molecule is oxidized at the Qo site, the process repeats to give a fully reduced QH2 at the Qi site. For a complete reduction of one UQ at the Qi site (including the uptake of two protons), there must be oxidation of two QH2 molecules at the Qo site (releasing four protons). Thus the net result is two protons translocated across the mitochondrial inner membrane. This bifurcated electron coupled proton transfer establishes the electrochemical gradient and the membrane potential that is used by ATP synthase to make ATP (32).

Although the Q-cycle is widely accepted by workers in the field as the model that best describes how electrons and protons flow in the cytochrome bc1 complex, many structural features near the ubiquinol reduction site (Qo) and the ubiquinone oxidation site (Qi) important to understand details of the Q-cycle remain unclear. These detailed binding geometries and dynamics play an essential role in controlling the chemical reaction mechanism, thermodynamically and kinetically, in such ways that the reaction occurs most sufficiently. One profound controversy concerning the cyt bc1 complex is the mechanism of the QH2 oxidation at the Qo site. The fact that there is no known crystal structure with a bound ubiquinol species and no definitive proof of a semiquinone intermediate(s) at any significant concentration near the Qo site (21, 33, 34) make it currently impossible to establish a clear and unambiguous mechanism. Although there are published X-ray diffraction structures of cyt bc1 complexes with some occupancy of a natural uqbuinone bound at the Qi site (with less than 50% occupancy), due to different hydrogen bonding patterns among these structures a consensus has not been reached for the mechanism of UQ reduction at the Qi site.

14

1.3.1. Mechanism at the Qo site: Concerted versus sequential

Crofts et al. proposed that the first electron transfer is coupled to a proton transfer to the ISC via a hydrogen bond between deprotonated His161 and QH2. They proposed that the proton is transferred first, thus producing a neutral semiquinone radical (QH•) at the catalytic site (35). The formation of this unstable intermediate would most definitely contribute to the energy barrier, explaining why the first electron transfer is the rate limiting step (36). In this mechanism, it is critical that the QH2 serves as a hydrogen bond donor to the unprotonated His161 that ligates the ISC. Moreover, the authors needed to provide a well-reasoned explanation for how the cyt bc1 complex avoids any bypass reactions, since the radical intermediate would be so reactive that it could act as an indiscriminate reductant and perform wasteful electron transfer. Therefore severe constraints on the redox states of the metal centers (ISC and heme bL), the protonation state(s) of amino acid side chains, and the conformational movement are required for this type of mechanism to be valid (37). Osyczka et al. suggested a simple solution to the problem of such rigid structural constraints by introducing a mobile water molecule that can easily rearrange its conformation as well as its protonation state depending on the redox states of the metal centers, in order to form hydrogen bond(s) with the SQ intermediates (37). Trumpower et al., on the other hand, proposed a double concerted proton coupled electron transfer without any stable intermediates. This hypothesis proposed that the two electrons are transferred simultaneously to the ISP and cytochrome b via a quinol-imidazolate-carboxylate complex without the formation of a semiquinone intermediate (38, 39). The fact that there is no known structure with any bound UQ or QH2 at the Qo site makes it currently impossible to find a consensus among these

different hypotheses. It thus remains debatable whether the coupled electron and proton transfer during QH2 oxidation is in a concerted or sequential mechanism. Chapter 3 of this dissertation will discuss more on the role of the QH2 as a hydrogen bond donor to the unprotonated His161 that ligates the ISC and the role of water molecules near the Qo site. Before discussing simulations to model the binding sites and geometries of UQ in the Qi site and QH2 in the Qo site, this work addresses the protonation states of ionizable amino acid side chains near these two electron transfer cofactor binding sites including the histidines ligand the ISC (chapter 2).

1.3.2. Mechanism at the Qi site: Sequential vs. Concerted

Because of the bifurcated electron transfer at the Qo site, the heme bH can only transfer one electron at a time to the Qi site and it is generally accepted that UQ is reduced at the Qi site via a two electron-gated mechanism (40-42). According to this mechanism, the first electron transfer from heme bH reduces the UQ to a stable semiquinone (SQ), then to a QH2 when the second turnover at the Qo site occurs. It was discussed earlier that the presence of a stable intermediate can give solid proof for the sequential electron coupled proton transfer reaction. Various studies had detected SQ at the Qi sites (40, 43, 44). Therefore, a consensus has been established that the coupled electron and proton transfer to the UQ at the Qi site proceeds by a sequential mechanism. Although the detectable SQ is strong proof for the sequential mechanism of ECPT in the Qi site, the challenge of elucidating the mechanistic details of the proton transfer and the sources of proton donors remains. Various available crystal structures have different hydrogen bonding patterns at the Qi site (41, 45-47). Most structures agree on the two potential proton donors His201 and Asp228 via their hydrogen bonds to UQ. However, it is still unclear whether these

hydrogen bonds are directly formed with the carbonyl oxygen on the UQ or indirectly via

a water molecule. The role of water molecules as proton donors will be challenging to

test and validate. Chapter 4 of this dissertation will discuss more on the role of water

molecules near the Qi site.

References

1. Mitchell P. The protonmotive Q cycle: A general formulation. FEBS Lett. 1975;59(2):137-9.

2. Trumpower BL, Gennis RB. Energy transduction by cytochrome complexes in mitochondrial and bacterial respiration: The enzymology of coupling electron transfer reactions to transmembrane proton translocation. Annu Rev Biochem. 1994;63:675-716.

3. Okamura MY, Feher G. Proton transfer in reaction centers from photosynthetic bacteria. Annu Rev Biochem. 1992;61:861-96.

4. Cukier RI, Nocera DG. Proton-coupled electron transfer. Annu Rev Phys Chem. 1998;49:337-69.

5. Babcock GT, Wikstrom M. Oxygen activation and the conservation of energy in cell respiration. Nature (London). 1992;356(6367):301-9.

6. Binstead RA, Moyer BA, Samuels GJ, Meyer TJ. Proton-coupled electron transfer between [ru(bpy)2(py)OH2]2+ and [ru(bpy)2(py)O]2+. A solvent isotope effect (kH2O/kD2O) of 16.1. J Am Chem Soc. 1981;103(10):2897-9.

7. Huynh MHV, Meyer TJ. Proton-coupled electron transfer. Chem Rev (Washington, DC, U S). 2007;107(11):5004-64.

8. Hammes-Schiffer S, Stuchebrukhov AA. Theory of coupled electron and proton transfer reactions. Chem Rev (Washington, DC, U S). 2010;110(12):6939-60.

9. Mayer JM. Simple marcus-theory-type model for hydrogen-atom transfer/proton-coupled electron transfer. J Phys Chem Lett. 2011;2(12):1481-9.

10. Hammes-Schiffer S. Theoretical perspectives on proton-coupled electron transfer reactions. Acc Chem Res. 2001;34(4):273-81.

11. Georgievskii Y, Stuchebrukhov AA. Concerted electron and proton transfer: Transition from nonadiabatic to adiabatic proton tunneling. J Chem Phys. 2000;113(23):10438-50.

12. Cukier RI. A theory that connects proton-coupled electron-transfer and hydrogen-atom transfer reactions. J Phys Chem B. 2002;106(7):1746-57.

13. Marcus RA. The theory of oxidation-reduction reactions involving electron transfer. I. J Chem Phys. 1956;24:966-78.

14. Paddock ML, Feher G, Okamura MY. Proton and electron transfer to the secondary quinone (QB) in bacterial reaction centers: The effect of changing the electrostatics in the vicinity of QB by interchanging asp and glu at the L212 and L213 sites. Biochemistry. 1997;36(46):14238-49.

15. Graige MS, Paddock ML, Bruce JM, Feher G, Okamura MY. Mechanism of proton-coupled electron transfer for quinone (QB) reduction in reaction centers of rhodopseudomonas sphaeroides. J Am Chem Soc. 1996;118(38):9005-16.

16. Cukierman S. Et tu, grotthuss! and other unfinished stories. Biochim Biophys Acta, Bioenerg. 2006;1757(8):876-85.

17. Swanson JMJ, Maupin CM, Chen H, Petersen MK, Xu J, Wu Y, et al. Proton solvation and transport in aqueous and biomolecular systems: Insights from computer simulations. J Phys Chem B. 2007;111(17):4300-14.

18. Karpefors M, Aedelroth P, Namslauer A, Zhen Y, Brzezinski P. Formation of the "peroxy" intermediate in cytochrome c oxidase is associated with internal proton/hydrogen transfer. Biochemistry. 2000;39(47):14664-9.

19. Stuchebrukhov AA. Mechanisms of proton transfer in proteins: Localized charge transfer versus delocalized soliton transfer. Phys Rev E Stat Nonlin Soft Matter Phys. 2009;79(3 Pt 1):031927.

20. Mayer JM. Proton-coupled electron transfer: A reaction chemist's view. Annu Rev Phys Chem. 2004;55:363-90.

21. Cape JL, Bowman MK, Kramer DM. A semiquinone intermediate generated at the qo site of the cytochrome bc1 complex: Importance for the q-cycle and superoxide production. Proc Natl Acad Sci U S A. 2007;104(19):7887-92.

22. Droese S, Brandt U. The mechanism of mitochondrial superoxide production by the cytochrome bc1 complex. J Biol Chem. 2008;283(31):21649-54.

23. Zhang L, Yu L, Yu C. Generation of superoxide anion by succinate-cytochrome c reductase from bovine heart mitochondria. J Biol Chem. 1998;273(51):33972-6.

24. Muller F, Crofts AR, Kramer DM. Multiple Q-cycle bypass reactions at the qo site of the cytochrome bc1 complex. Biochemistry. 2002;41(25):7866-74.

25. Yin Y, Yang S, Yu L, Yu C. Reaction mechanism of superoxide generation during ubiquinol oxidation by the cytochrome bc1 complex. J Biol Chem. 2010;285(22):17038-45.

26. Berry EA, Huang L, Lee D, Daldal F, Nagai K, Minagawa N. Ascochlorin is a novel, specific inhibitor of the mitochondrial cytochrome bc1 complex. Biochim Biophys Acta, Bioenerg. 2010;1797(3):360-70.

27. Fernandez-Ortuno D, Tores JA, de Vicente A, Perez-Garcia A. Mechanisms of resistance to QoI fungicides in phytopathogenic fungi. Int Microbiol. 2008;11(1):1-9.

28. Looareesuwan S, Chulay JD, Canfield CJ, Hutchinson DBA. Malarone (atovaquone and proguanil hydrochloride): A review of its clinical development for treatment of malaria. Am J Trop Med Hyg. 1999;60(4):533-41.

29. Farnert A, Lindberg J, Gil P, Swedberg G, Berqvist Y, Thapar MM, et al. Evidence of plasmodium falciparum malaria resistant to atovaquone and proguanil hydrochloride: Case reports. Bmj. 2003;326(7390):628-9.

30. Kessl JJ, Lange BB, Merbitz-Zahradnik T, Zwicker K, Hill P, Meunier B, et al. Molecular basis for atovaquone binding to the cytochrome bc1 complex. J Biol Chem. 2003;278(33):31312-8.

31. Mitchell P. Possible molecular mechanisms of the protonmotive function of cytochrome systems. J Theor Biol. 1976;62(2):327-67.

32. Maloney PC, Kashket ER, Wilson TH. Protonmotive force drives ATP synthesis in bacteria. Proc Natl Acad Sci U S A. 1974;71(10):3896-900.

33. Zhang H, Osyczka A, Dutton PL, Moser CC. Exposing the complex III qo semiquinone radical. Biochim Biophys Acta, Bioenerg. 2007;1767(7):883-7.

34. Samoilova RI, Kolling D, Uzawa T, Iwasaki T, Crofts AR, Dikanov SA. The interaction of the rieske iron-sulfur protein with occupants of the Q0-site of the bc1 complex, probed by electron spin echo envelope modulation. J Biol Chem. 2002;277(7):4605-8.

35. Crofts AR, Holland JT, Victoria D, Kolling DRJ, Dikanov SA, Gilbreth R, et al. The Q-cycle reviewed: How well does a monomeric mechanism of the bc1 complex account for the function of a dimeric complex?. Biochim Biophys Acta, Bioenerg. 2008;1777(7-8):1001-19.

36. Hong S, Ugulava N, Guergova-Kuras M, Crofts AR. The energy landscape for ubihydroquinone oxidation at the Q0 site of the bc1 complex in rhodobacter sphaeroides. J Biol Chem. 1999;274(48):33931-44.

37. Osyczka A, Moser CC, Dutton PL. Fixing the Q cycle. Trends Biochem Sci. 2005;30(4):176-82.

38. Trumpower BL. A concerted, alternating sites mechanism of ubiquinol oxidation by the dimeric cytochrome bc1 complex. Biochim Biophys Acta, Bioenerg. 2002;1555(1-3):166-73.

39. Snyder C, Trumpower BL. Mechanism of ubiquinol oxidation by the cytochrome bc1 complex: Pre-steady-state kinetics of cytochrome bc1 complexes containing site-directed mutants of the rieske iron-sulfur protein. Biochim Biophys Acta, Bioenerg. 1998;1365(1-2):125-34.

40. Dikanov SA, Samoilova RI, Kolling DRJ, Holland JT, Crofts AR. Hydrogen bonds involved in binding the qi-site semiquinone in the bc1 complex, identified through deuterium exchange using pulsed EPR. J Biol Chem. 2004;279(16):15814-23.

41. Gao X, Wen X, Esser L, Quinn B, Yu L, Yu C, et al. Structural basis for the quinone reduction in the bc1 complex: A comparative analysis of crystal structures of mitochondrial cytochrome bc1 with bound substrate and inhibitors at the qi site. Biochemistry. 2003;42(30):9067-80.

42. Lange C, Hunte C. Crystal structure of the yeast cytochrome bc1 complex with its bound substrate cytochrome c. Proc Natl Acad Sci U S A. 2002;99(5):2800-5.

43. Kolling DRJ, Samoilova RI, Holland JT, Berry EA, Dikanov SA, Crofts AR. Exploration of ligands to the qi site semiquinone in the bc1 complex using high-resolution EPR. J Biol Chem. 2003;278(41):39747-54.

44. Salerno JC, Osgood M, Liu Y, Taylor H, Scholes CP. Electron nuclear double resonance (ENDOR) of the QcÂ·- ubisemiquinone radical in the mitochondrial electron transport chain. Biochemistry. 1990;29(30):6987-93.

45. Huang L, Cobessi D, Tung EY, Berry EA. Binding of the respiratory chain inhibitor antimycin to the mitochondrial bc1 complex: A new crystal structure reveals an altered intramolecular hydrogen-bonding pattern. J Mol Biol. 2005;351(3):573-97.

46. Hunte C, Koepke J, Lange C, Rossmanith T, Michel H. Structure at 2.3 Ã… resolution of the cytochrome bc1 complex from the yeast saccharomyces cerevisiae co-crystallized with an antibody fv fragment. Structure (London). 2000;8(6):669-84.

47. Esser L, Elberry M, Zhou F, Yu C, Yu L, Xia D. Inhibitor-complexed structures of the cytochrome bc1 from the photosynthetic bacterium rhodobacter spheroides. J Biol Chem. 2008;283(5):2846-57.

CHAPTER 2

pKa VALUES OF IONIZABLE AMINO ACID SIDE CHAINS OF THE IRON-SULFUR PROTEIN AND CYTOCHROME B, FROM THE BOVINE CYTOCHROME BC1 COMPLEX AND IMPLICATIONS FOR THE MECHANISM OF COUPLED ELECTRON AND PROTON TRANSFER

Abstract:

Cytochrome bc1 (cyt bc1) is a protein complex found in the inner mitochondrial membrane of eukaryotes and functions as a critical part of the respiratory electron transport chain. Malfunctions of cyt bc1 in human result in myopathies, whereas cyt bc1 is an attractive drug target in bacteria and fungi. Among several competing proposals for the mechanism of electron-coupled proton transfer in cyt bc1 are one requiring a deprotonated His161 (ligated to the Rieske iron-sulfur cluster) or one requiring a deprotonated Glu 271 of cytochrome b to function as the first proton acceptor and thus initiate the oxidation of substrate ubiquinol to ubiquinone. Although pKa values of Glu271 (5.2-5.7), as well as His 141/His161 ligands of the iron-sulfur cluster have been measured (7.63 ± 0.15 /9.16 ± 0.28) and calculated (6.9/8.8), no published study of pKa values in mammalian cyt bc1 has successfully established whether His161 should be deprotonated at physiological pH. This contribution describes constant pH molecular dynamics (CPHMD) simulations to calculate pKa values for all ionizable amino acid side chains of the iron-sulfur protein, cytochrome b, and cytochrome c from the bovine cyt bc1 complex. CPHMD simulations show pKa values of 5.1, 7.8 ± 0.5 and 9.1 ± 0.6 for Glu271, His141, and His161, respectively. Free energy perturbation simulations verify

that His161's pKa value shifts up more than that of His141 upon moving the iron-sulfur cluster from water into the protein. Fluctuations of Cys160 into hydrogen-bonding distance of the Nε atom of His161 provides a dynamical rationale for the higher pKa of His161 and a reason why calculations on the static protein might not appropriately model the His161 shift to a higher pKa. Calculated pKa shifts thus imply that the concentration of deprotonated His161 is extremely low at physiological pH and His161 is unlikely to serve as the initial proton acceptor. In contrast, Glu271 is deprotonated and may function as a proton acceptor at physiological pH.

2.1. Introduction:

2.1.1. Mitochondrial cytochrome bc1 complex:

The mitochondrial cytochrome (cyt) bc1 complex and its homologous cyt b6f complex are essential proteins for respiratory and photosynthetic electron transport chain coupled ATP production across all organisms (1). Because of its function as an electron transfer protein, the cyt bc1 complex is also a major source of reactive oxygen species (ROS) (2, 3). It is possible for a semiquinone (SQ) intermediate radical to be formed when electrons shuttle through ubiquinone/ubiquinol (UQ/QH2) and the metal centers (2), or when the bifurcated reaction at the Qo site is disrupted (2, 4). This radical is reactive and will react with any oxygen species (O_2 or H_2O) nearby to form ROS that can harm the cells. Under normal conditions, the efficiency of cyt bc1 surpasses any bypass reactions that could cause wasteful electron transfer. Additionally, the cyt bc1 complex's conformational dynamics ensure that reactive SQ intermediates are shielded from oxygen species by maximizing efficiency in electron transfer to cyt c. General defects of the mitochondrial cyt bc1 complex result in shutting off the electron transfer chain (ETC) and, ultimately,

cell death. In particular, inhibition at the Qo site not only disrupts the ETC, but also results in ROS production. It is believed that the ROS are commonly found in oxidatively stressed cells, resulting in apoptosis induction (3). Therefore, any defect in the bifurcated electron transfer at the Qo site is likely to cause ROS production in mitochondrial cytochrome bc1 (3, 5, 6). The cyt bc1 complex is also a desirable target for anti-biotic (7), anti-fungal (8), anti-malaria, and anti-pneumonia therapeutics (9-11).

A modified Q-cycle (Figure 1.2.2) describes the bifurcated electron transfer mechanism. For a complete reduction of one UQ at the Qi site (uptake of two protons), there must be oxidation of two QH2 molecules at the Qo site (release of four protons) and thus the net result is two protons translocated across the mitochondrial inner membrane. The Q-cycle is widely accepted to describe the bifurcated electron coupled proton transfer across the mitochondrial inner membrane, thus establishing the electrochemical gradient and the membrane potential used by ATP synthase to make ATP (12). It remains uncertain, however, whether QH2 oxidation at the Qo site proceeds by a concerted or a sequential mechanism.

2.1.2. Protonation states of the ionizable amino acid side chains near the Qi site

It is widely accepted that amino acid side chains near the Qi site are highly conserved among most species. In the bovine cyt bc1 complex numbering system, they are His201, Asp228, and Ser205 (13-16). In the yeast structure, Lys227 was also proposed to play a role in substrate binding. The His201 and Asp228 residues are proposed to act as proton donors for the UQ reduction, i.e., they must be protonated (14, 15). Lys227, with its highly flexible side chain, was suggested to fetch a water proton donor from the matrix

27

side into the Qi pocket (16). Near physiological pH (~7), if the residues are fully solvent-exposed, it is likely that both His201 (pKa ~6) and Asp228 (pKa ~4) are deprotonated while Lys227 is protonated. In cyt bc1, however, these residues are buried and thus the protein environment may have an effect on the pKa values. We report in this work the calculated pKa values of these residues using constant pH molecular dynamics (CPHMD) simulations (17). Once amino acid side chain protonation states are established, the following chapters report simulations to define UQ binding geometries and interactions with amino acid side chains and discuss their mechanistic and biological implications.

2.1.3. Protonation states of His141, His161 and Glu271 near the Qo site

Although structures of the cyt bc1 complex have been extensively studied using X-ray crystallography, to our knowledge, there is no known structure with any ubiquinol species near the Qo site. Therefore, investigations of QH2 binding geometries are typically inferred from X-ray crystallographic studies with various bound inhibitors (14-16, 18, 19). The competitive inhibitor of QH2, stigmatellin (SMA), received the most attention because it showed two hydrogen bonds: one to the Glu271 of cyt b and one to the His161 ligand of the ISC. Thus, an obvious and educated extrapolation is that these hydrogen bonds also stabilize the substrate at the Qo binding site. It was widely accepted that a hydrogen bond forms between the epsilon nitrogen NE2 of deprotonated His161 and a second hydrogen bond forms between a carboxylic oxygen of Glu271 and the second head group hydroxyl oxygen of the QH2 (directly or via a water molecule). These interactions are proposed to stabilize the substrate at the Qo site. This binding geometry would also allow His161 and Glu271 to serve as proton acceptors in QH2 oxidation (20-22). Crofts et al. proposed a sequential mechanism with the first electron transfer to the

ISC, following the first proton transfer to deprotonated His161. Therefore, His161 deprotonation is a critical condition for the QH2 oxidation to occur (21-23). Trumpower, on the other hand, proposed that a hydroxyl hydrogen of QH2 replaces a proton of the imidazole nitrogen of His161 during the electron transfer in a concerted fashion (20) i.e., His161 was initially protonated before interaction with QH2.

Covian et al. performed kinetic studies of the binding affinities of ubiquinone analogues (decylbenzoquinone and decylbenzoquinol) and proposed that an acidic residue at the Qo site with pKa ≈ 5.7, possibly Glu271, had to be deprotonated in order for the catalytic reaction to occur. In this hypothesis, Glu271 was the first proton acceptor and the protonation state of His161 had no significant role in the initial electron coupled proton transfer from QH2 (24, 25). One way to provide additional information regarding the protonation states of His161 and Glu271 is to calculate the pKa values of these residues in the protein environment. For this reason (and other reasons that were discussed elsewhere in literature (26, 27)), the pKa values of His161 and His141 of the ISP are of great interest and have been studied experimentally (26) and computationally (28).

For the oxidized ISC, experimental measurements reported two pKa values linked to the redox potential of the Riseke ISP: 7.63 ± 0.15 and 9.16 ± 0.28 for the bovine ISP (26); and 7.85 ± 0.15 and 9.6 ± 0.12 for a bacterial ISP *(Thermus Thermophilus)* (29). While it might be tempting to assign the lower pKa values to one specific iron-ligated histidine residue in cyt bc1 (His141 or His161 in bovine and His134 or His154 in bacteria), experimental assignment of these pKa values to individual iron-ligated histidines remains challenging. The paramagnetic nature of the Rieske ISC broadens not only ^{1}H NMR signals but also ^{15}N signals from both delta nitrogen atoms on the imidazole rings of the

iron-ligated histidines. Moreover, the electronic spin coupling between the two high spin irons (Fe^{3+}) results in an electron paramagnetic resonant silent ground state (30, 31). Therefore, His141 and His161 are rendered virtually indistinguishable by NMR and attempts to assign individual pKa values to each histidine have so far proven extremely difficult. Nevertheless, in the bovine cyt bc1 complex, His161 is often assumed to have the lower pKa value, suggesting that it serves as a hydrogen bond acceptor from QH2 and can act as the first proton acceptor, as discuss above. In contrast, for the related bacterial ISP (*Thermus Thermophilus*), with almost identical structure near the ISC, a ^{15}N NMR titration study originally assigned the lower pKa value (~7) to His134 (His 141 in bovine cyt bc1), but subsequent experiments by the same group were interpreted to imply that His154 (His161 in bovine) has the lower pKa. The more recent experiments were thus interpreted to suggest that His154 (His161 in bovine) plays the role of the proton acceptor in QH2 oxidation (32). Thus, the assignment of individual pKa values for each iron-ligated histidine is controversial, has important mechanistic implications, and is therefore attractive for computational studies.

For the oxidized ISC, combined density functional theory and continuum electrostatics (DFT-CE) methods reported two apparent pKa values of 6.9 and 8.8 for the singly and doubly deprotonated states of the ligand histidines (28). These values are in agreement with the experimentally measured values of 7.63 ± 0.15 and 9.16 ± 0.28 for two ionizable groups that are linked to the redox transition of the Rieske protein (oxidized) (26). In the quantum chemical method, a DFT treatment applied to the ISC center with a continuum electrostatics (CE) environment to model the protein and a novel decoupled site representation (33) to account for multiple titratable interacting sites in proteins. The

DFT-CE method was adopted to account for the electronic effects that could perturb the pKa values of the two iron-ligated histidines. The titration method was developed to account for more than one site that can titrate. Despite the quantum chemical studies to address the issue, the pKa calculations based on DFT-CE omitted protein conformational dynamics. Additionally, while trying to account for the strong electronic effects that perturb the pKa values of the iron-ligated histidines using quantum treatments, the macroscopic pKa's obtained from this method are the overall pKa's of all possible microscopic deprotonated states of the entire system. Therefore both histidines contribute to the approximation of the two reported apparent pKa values, i.e., calculated pKa values cannot be assigned to an individual histidine. In contrast, the molecular dynamics simulations reported here implicitly assume that the symmetrical iron-sulfur cluster perturbs both His141 and His161 to the same degree and it is the protein environment that distinguishes His 141 and His161. Moreover, molecular dynamics simulations include the conformational dynamics of the local protein environment around His141 and His161 omitted from the DFT-CE calculations. Finally, free energy perturbation simulations (34) were performed to confirm pKa shifts calculated by using the CPHMD method. Our hypothesis is therefore that the conformational dynamics of the local protein environment near these two histidines are different and can distinguish the pKa values of His141 and His161.

2.2. Material and methods

2.2.1. Molecular dynamics

For this work, the starting structure for MD simulations includes the ISC with the ISP head domain that was truncated from a bovine cytochrome bc1 complex crystal structure,

obtained from the Protein Data Bank (http://www.rcsb.org/pdb/home/home.do), PDB ID

1PP9 (15). The 1PP9 structure was selected because of its relatively high resolution of

2.1Å and a low R-value of 0.25. We used VMD (35)

(http://www.ks.uiuc.edu/Research/vmd/) to prepare the starting structure. The

CHARMM27 force field parameters (36) for protein with an improved treatment for the

backbone by including the dihedral cross term map (37) were used. All missing hydrogen

atoms were added. The proteins' N-termini and C-termini were capped with acetylate and

amidate, respectively. Heavy atoms missing from the X-ray crystal structure were placed

using the CHARMM computer program (36). All undefined atoms from the X-ray

structure were deleted. The system was solvated with TIP3P water (38) to a distance of

10Å from any atom of the protein in each direction. A one femtosecond time step was

used in isothermal-isobaric (constant NPT) simulations with temperature maintained at

300K using Langevin dynamics with a damping coefficient of 5.0 ps^{-1} and with the

pressure maintained at 1 atm, using a Langevin piston. The cutoff for electrostatic and

van der Waals potentials was 12Å with a switching function on and a switching cutoff of

10Å. Periodic boundary conditions were applied with the Particle Mesh Ewald (PME)

(39) grid spacing of 1.0Å for a full system periodic electrostatic potential. The NAMD

(40) and CHARMM (36) standard energy minimization steps were performed preceding

dynamics steps for equilibration and for data collection.

2.2.2. Constant pH molecular dynamics

The CPHMD method was used to calculate the unprotonated fraction (S^{unprot}) of the

population from the probability of finding a state being protonated or unprotonated. The

S^{unprot} at different pH values and their corresponding pHs were fit to the Henderson-

Hasselbalch equation in order to calculate the pKa. The CPHMD method combines sampling of both multiple conformations and multiple protonation states in order to account for the coexistence of the protonated and un-protonated states if there is more than one titrating residue. The hybrid Hamiltonian in CPHMD propagates along both spatial and continuous titration coordinates and is thus intended to take into account of any pH-coupled conformational dynamics.

CPHMD was used in this work to calculate the pKa values of the iron-ligated histidines and the other ionizable amino acid side chains in the cyt bc1 complex. CPHMD in CHARMM was developed to study the pKa shifts of a model free amino acid in a protein with multiple titratable groups, titrating between protonated and unprotonated states, in response to a specific pH (17). In this work, simulations using the CPHMD method were done to calculate pKa shifts for all ionizable amino acid residues in the ISP including His141, His161, and Glu271. These simulations were done independently from those using the FEP method. Keeping in mind our goal of distinguishing the two histidine pKa values and our assumption that the symmetrical ISC electronic effects on the two histidine ligands are virtually identical, the pKa value of a free histidine in water was used as the model for CPHMD simulations. Since the experimental pKa value of a more appropriate model of the ISC coordinated by two cysteines and two histidines is unavailabale, we used FEP to calculate pKa shifts for the ISC in protein compared to water, to validate the CPHMD results qualitatively.

CPHMD uses a continuous perturbation variable lambda (between 0 and 1) to define the protonated state (lambda=0) and the unprotonated state (lambda=1). CPHMD can specify the particular residues to be titrated and takes into account the effect of any

conformational changes of the protein on the protonation state of the titrating residue, since lambda is propagated along with the coordinates during the simulations. The fraction of the unprotonated state, S^{unprot}, is calculated through the probability of finding a state either protonated or unprotonated. Fitting of the S^{unprot} to the Henderson-Hasselbach equation yields pKa values:

$$S^{unprot} = \frac{1}{1+10^{(pKa-pH)}} \quad (1)$$

A Replica Exchange (REX) (41) algorithm was incorporated into the CPHMD simulations to overcome the difficulties associated with having multiple local minima in MD simulations of a protein (42). In this study, REX-CPHMD simulations were performed with 16 replicas, using temperatures ranging from 298K to 450K. The replicas with adjacent temperatures were allowed to exchange and the spatial and titration coordinates were saved every 1000 dynamics steps. Langevin dynamics were applied on all replicas. Simulations used the GBSW implicit solvent model with the same parameters described by Khandogin et al. (42). Extensive tests of the REX-CPHMD calculations of pKa values are published and show that pKa values calculated after one nanosecond of simulation time are comparable to those obtained after 10ns of simulation time (43). Furthermore, typical errors for histidine pKa values calculated by the REX-CPHMD method are ~0.6 pKa units (44). Simulations with REX-CPHMD were therefore performed at pH 7, 8 and 9 for one nanosecond each. The standard REX-CPHMD protocol, where configurations are sampled over the entire 1ns simulation time, was followed. The fraction of the population in the unprotonated state (S^{unprot}) is obtained

as shown in the equation below, where ρ^U is the probability of finding the unprotonated state, and ρ^P is the probability of finding the protonated state.

$$S^{unprot} = \frac{\rho^U}{\rho^U + \rho^P} = \frac{1}{1 + \rho^P / \rho^U} \quad (2)$$

2.2.3. Free Energy Perturbabtion

2.2.3.1. Thermodynamic cycle for calculating pKa shifts

We propose a protocol to calculate the pKa shifts of amino acids ligands to the ISC in the protein environment relative to a model ISC in water using Free Energy Perturbation (FEP) theory. MD simulations reported here use FEP theory to calculate the change in free energy of deprotonating an imidazole ligand in a model including two imidazole and two methanethiolate ligands to an oxidized model ISC in water and the ISC (with its two histidine and two cysteine ligands) in the protein, according to the thermodynamic cycle in Figure 2.2.3.1.

Simulations were thus performed to calculate the change in free energy for the deprotonation of an ISC model in solvent ($\Delta G_{(aq)}$) and in the protein ($\Delta G_{(protein)}$) using FEP, according to the thermodynamic cycle described in Figure 2.2.3.1 In this thermodynamic cycle, the free energy of the solvated proton would cancel and thus $\Delta\Delta G = \Delta G(protein - \Delta G(aq)$ calculated from this thermodynamic cycle gives the difference in free energy for deprotonating the iron-ligated imidazoles in water and the iron-ligated histidines in the protein. The change in free energy for deprotonation can be related to the equilibrium constant for acid dissociation K_a

$$\Delta G_{(protein)} = -RT \ln K_a^{protein} \, (3)$$

$$\Delta G_{(aq)} = -RT \ln K_a^{aq} \, (4)$$

$$\Delta G_{(protein)} - \Delta G_{(aq)} = -RT\left(\ln K_a^{protein} - \ln K_a^{aq}\right) = -RT \ln\left(\frac{K_a^{protein}}{K_a^{aq}}\right)(5)$$

$$\frac{K_a^{protein}}{K_a^{aq}} = -\frac{1}{RT} \exp\left(\Delta G_{(protein)} - \Delta G_{(aq)}\right)(6)$$

From the difference in the change in free energy for His141 or His161 deprotonation in solution and in the protein, the pKa shifts for each residue can also be calculated from

$$\Delta pKa = \frac{1}{\ln(10)RT}\left(\Delta G_{(protein)} - \Delta G_{(aq)}\right)(7)$$

Substituting equation (7) into equation (6) gives the fraction of unprotonated histidines in protein and in water

$$\frac{K_a^{protein}}{K_a^{aq}} = 10^{-\Delta pKa}(8)$$

$$AH_{(aq)} \underset{}{\overset{\triangle G_{(aq)}}{\rightleftharpoons}} A^{-}{}_{(aq)} + H^{+}{}_{(aq)}$$

$$AH_{(protein)} \underset{\triangle G_{(protein)}}{\overset{}{\rightleftharpoons}} A^{-}{}_{(protein)} + H^{+}{}_{(aq)}$$
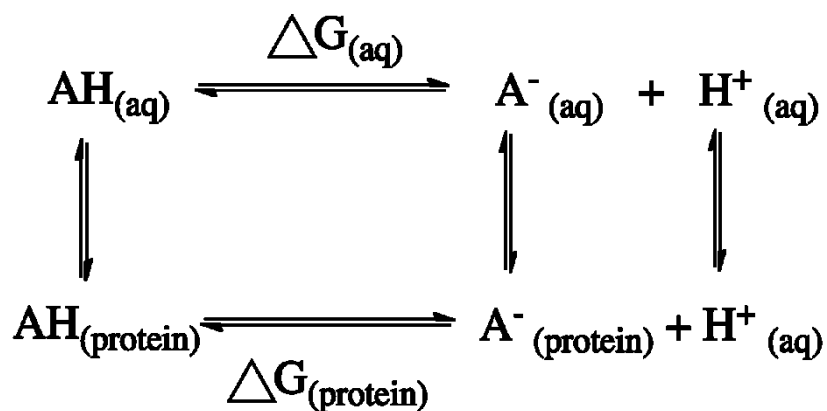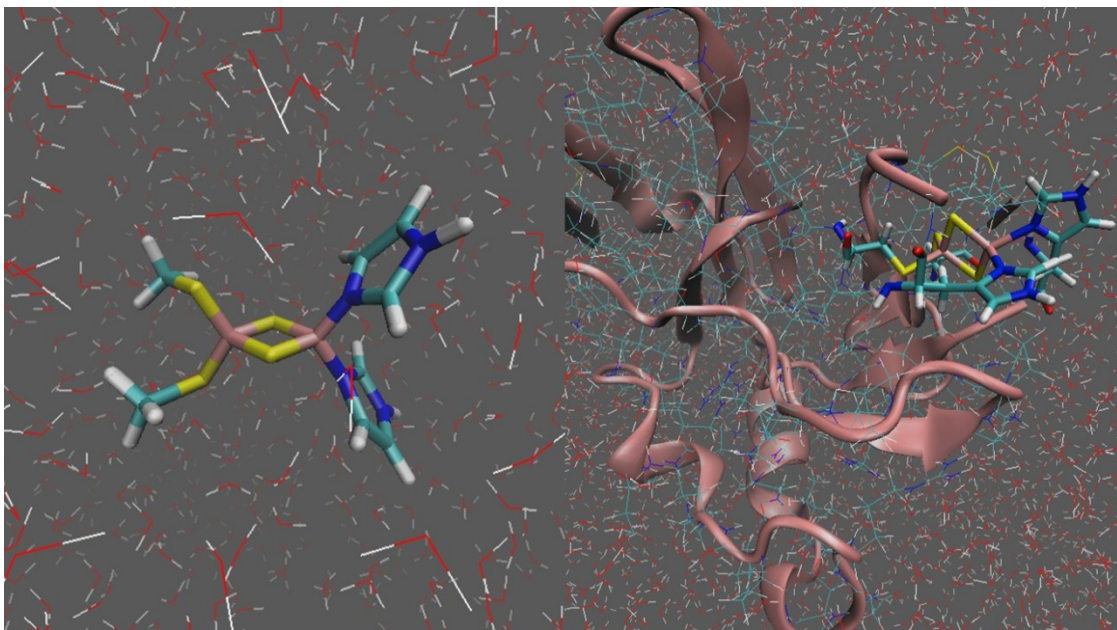
Figure 2.2.3.1: The thermodynamic cycle described in FEP simulation

The thermodynamic cycle used with FEP simulations, where AH is the ISC model in the fully protonated form. The change in free energy upon deprotonation of this model in aqueous solution ($\Delta G_{(aq)}$) was subtracted from the change in free energy upon deprotonation of His141 and His161 in the protein ($\Delta G_{(protein)}$) to yield the differences in free energy for deprotonation of either His141 or His161 in the protein relative to their deprotonation free energy in water. In this thermodynamic cycle, the free energy of

hydration of the proton in water appears in both the top and bottom reactions of the cycle and cancels.

2.2.3.2. Model for the ISC center
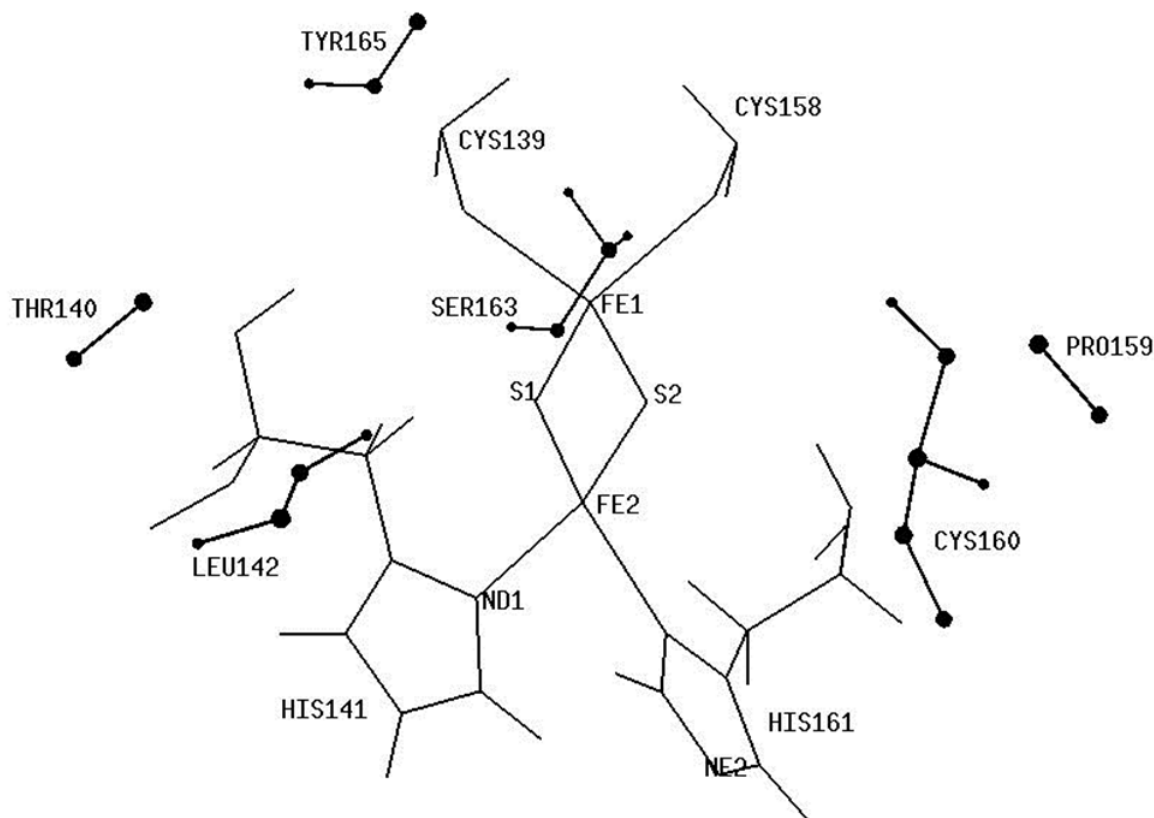
Figure 2.2.3.2: Atoms of the oxidized ISC center

Atoms of the oxidized ISC center whose published charges were obtained from geometry optimizations using a DFT-CE method for the oxidized ISC, deprotonated His161, and protonated His141(27). The dashed lines show atoms within hydrogen bonding distance between the ISC and neighboring residues, and among these residues themselves.

The Rieske ISC center model for FEP simulations consists of two histidine side chain imidazole rings, two methanethiolate groups, and an ISC [2Fe-2S] (Figure 2.2.3.1). The

38

iron-ligated imidazole rings represented His141 and His161 side chains and both were protonated at the epsilon nitrogen (NE2). One iron of the [2Fe-2S] cluster was ligated at the delta nitrogen (ND1) atoms of both imidazole rings and one iron of the [2Fe-2S] cluster was ligated by the methanethiolate sulfur atom. Partial charges for the ISC center were obtained from the calculations of Ullmann et al. (28), using the DFT method for the oxidized ISC in cyt bc1, with a total charge of zero for the protonated state and a total charge of negative one for the deprotonated state.

For this model of the Rieske ISC center, the two (freely rotating) imidazole rings are symmetrically located along the iron-iron axis and are therefore chemically identical. Deprotonation of either imidazole ring in water is indistinguishable and thus yields the same result. Therefore, average charges from all atoms of the two protonated iron-ligated residues were used and scaled to zero charge for the protonated state of the ISC center model. Similarly, average charges from all atoms of the two deprotonated iron-ligated residues were scaled to negative one for the deprotonated state of the ISC center model. Although we are aware that the partial charges themselves may not fully account for the electronic effects introduced by the ISC that perturb the pKa values of the imidazole ring compared to a free histidine, we assume that these effects perturb both symmetry-equivalent imidazole rings to the same degree. This allows us focus on the effects of structural and dynamical differences in the protein environment near His141 and His161. When transferring the ISC center model into the protein, the rest of the ISP, including the ligand residues' hydrogen bond partners are included and the protein dynamics are fully incorporated. Figure 2.2.3.2 shows atoms whose charges were obtained from published quantum calculations: the ISC, all atoms of His141 and His161, the beta carbon atom, its

hydrogen atoms HB1, HB2 and the SG atom of Cys139 and Cys158, and atoms of the

neighboring residues that formed hydrogen bonds with them. FEP calculations for

deprotonation of the ISC model described above in water and for deprotonation of

His141 and His161 in the protein were then performed.

2.2.3.3.   Theoretical framework for Free Energy Perturbation:

FEP uses a coupling parameter λ to describe the transformation between an initial

reference state ($\lambda=0$) and a final target state ($\lambda=1$) by a series of small, incremental,

reversible transformations between nonphysical intermediate states. In this case, $\lambda=0$

corresponds to the neutral protonated state and $\lambda=1$ corresponds to the charged

deprotonated state. The free energy, therefore, is a continuous function of λ along the

deprotonation path and the change in free energy upon deprotonation can be evaluated as

an ensemble average:

$$\Delta G_{0\to1} = -k_B T \sum_{k=1}^{N} \ln\left\langle \exp\left(-\frac{\Delta U}{k_B T}\right)\right\rangle_k \quad (9)$$

where k_B is the Boltzmann constant, T is temperature, ΔU is the potential energy

difference between intermediate states k and k+1, N is number of intermediate states and

$\langle...\rangle_k$ denotes the ensemble average over configurations sampled at state k. One hundred

thousand NAMD standard minimization steps were performed, followed by 1 ns of

equilibration of the solvated protein in a box of water. FEP with soft core potential

simulations of 40 non-linear intermediate states with lambda windows narrower near the

two end points were performed for a total of 40 ns. Each window included 500,000

equilibration steps and 500,000 ensemble average sampling steps. It is an established

practice for FEP calculations to perturb the system in both forward and reverse directions

(45). Results from both reference and target equilibrium ensembles were then combined

using the ParseFEP (46) plugin in VMD to calculate the change in free energy. ParseFEP

provides a toolkit to combine bidirectional FEP data sets (evaluated for perturbations in

forward and reverse directions) and quantify convergence of FEP calculations by

estimating the statistical errors from variances of the estimated free energy.

2.3. Results and discussion

2.3.1. pKa shifts of ionizable amino acid side chains in the Rieske ISP

Table 2.1 compares our calculated pKa values of ionizable residues in the Rieske ISP

other than His141, His161, or Glu271, obtained from CPHMD simulation, to the pKa

values obtained from DFT-CE methods (28). These residues have pKa values that are

within 1 pKa unit of the published values calculated by using DFT-CE methods. The

average difference is 0.5 pKa unit, and is within the typical error range of the CPHMD

method (43). All of these acidic residues are in the unprotonated form in the protein.

Residue Glu131 has the highest pKa, shifted down by only 1.5 pKa unit compared to its

value in water. Conformational dynamics shows that Glu131 is completely exposed to the

solvent and prefers its charged, deprotonated state.

Table 2.1: pKa values of the acidic amino acid side chains in the Rieske ISP						
	GLU75	ASP80	GLU83	ASP107	GLU109	GLU113
CPHMD	4.4	4.0	3.5	4.1	4.8	3.4
DFT-CE(27)	4.6	3.6	3.7	3.3	3.8	2.6
RESID	GLU125	GLU131	ASP152	GLU181	GLU186	ASP190
CPHMD	4.0	2.9	3.4	3.4	3.7	4.3
DFT-CE(27)	3.4	3.3	3.6	4.1	3.9	4.9

2.3.2. pKa shifts of ionizable amino acid side chains near the Qo and Qi sites

Tables 2.2 and 2.3 show pKa values for ionizable residues near the Qo and Qi sites of the cytochrome b subunit, respectively, when there are no bound substrates. The calculated pKa value for Glu271 is 5.1, in good agreement with the experimentally measured pKa of 5.2 - 5.7 by Covian et al (24). Thus, in the protein the Glu271 is unprotonated and fully capable of acting as a proton acceptor for QH2 oxidation at the Qo site. Our calculated values thus support the hypothesis by Covian et al. (24) that residue Glu271 may be the first proton acceptor for QH2 oxidation at the Qo site in bovine cyt bc1 complex.

Table 2.2: pKa values of the acidic amino acid side chains in the cytochrome b subunit near the Qo site

	GLU271	HIS267	GLU162	ASP254	GLU252	ASP171
CPHMD	5.1	7.4	4.9	4.6	3.8	3.5
EXP	5.2 - 5.7[a]					

[a] The experimentally measured pKa values of 5.2 and 5.7 for Glu271, measured from the effects of pH on the binding affinity of the quinone analogues decylbenzoquinone and decylbenzoquinol, respectively(24)

Table 2.3: pKa values of the acidic amino acid side chains in the cytochrome b subunit near the Qi site

	HIS201	**LYS227**	**ASP228**
CPHMD	6.7	8.9	3.9

The calculated pKa values for His201, Asp228, and Lys227 are 6.7, 3.9 and 8.9, respectively. A free histidine side chain in solution has pKa value ~6.0 (47). Thus, His201 has its pKa shifted up by 0.7 pKa unit, so it is almost certainly singly protonated in the protein under physiological pH. Meanwhile, the singly protonated His201 can form a direct hydrogen bond to the carbonyl oxygen on the UQ head group. Residue Asp228 has the same pKa value as that of an aspartic acid side chain in water, consistent with our

simulations showing that Asp228 is exposed to solvent. Lastly, Lys227 has a calculated downward pKa shift of 1.5 pKa units comparing to the pKa of a lysine in water implying that Lys227 is buried in the protein interior. A recent study of interactions between the inhibitor antimycin and various amino acids near the Qi site, including Lys227, reported water occupancy of less than 30% near Lys227 in the bovine cyt bc1 complex (48). This result together with our computed pKa value for Lys227, shows that Lys227 is buried in the protein and does not likely play the role of fetching water moleculesfrom solution to the Qi site to serve as proton donors, which is consistent with proposals from previous studies of the yeast complex (13). Thus the computed pKa values allow us to assign the singly protonated state to His201, the protonated state to Lys227 and the deprotonated state to Asp228 for the initial UQ binding geometries in the MD simulations reported in chapter 4.

2.3.3. pKa shifts of the iron-ligated His141 and His161

2.3.3.1. CPHMD simulations

From our CPHMD simulations, we obtained the individual, distinct pKa values of 7.8 ± 0.5 for His141 and 9.1 ± 0.6 for His161, for the oxidized ISC in the protein environment. Our results are in good agreement with experimentally measured values in the bovine ISP (7.6 and 9.2) (26) and in *Thermus thermophilus* (7.8 and 9.6) (29), a bacterial protein with an almost identical structure near the ISC. The reported standard deviations show that the present results are within statistical error of the experimental measurements (7.63 ± 0.15 and 9.16 ± 0.28), indicating a very good precision. Furthermore, the computed pKa of His161 shows a smaller absolute error than that of His141. Because of the nature of the CPHMD method, it is easier and more accurate to compute the pKa value of

44

His161 than His141 since it is slightly more solvent-exposed (42). Our result of a higher

pKa for His161 and a lower pKa for His141 contradicts the hypothesis that a

deprotonated His161 accepts the first proton of QH2 in a sequential mechanism for

electron-coupled proton transfer.

2.3.3.2.   FEP calculations

Figure 2.3.3.2.1 shows the probability distributions from forward and reverse simulations

for the deprotonation of the imidazole ligated to the ISC center model in water. Good

overlap between the distributions for simulations in the forward and reverse directions

indicates convergence with respect to simulation time within each window. Figure

2.3.3.2.2 show the summary of the bidirectional FEP simulations for the deprotonation of

the aqueous Rieske ISC center model. For the change in free energy, there is excellent

overlap of the energies in both directions. The changes in internal energy can be

approximated and show good agreement in the forward and backward reactions. The

changes in entropy can also be estimated from the extended FEP formalism, however

entropies are intrinsically harder to approximate and thus less accurate than free energies.
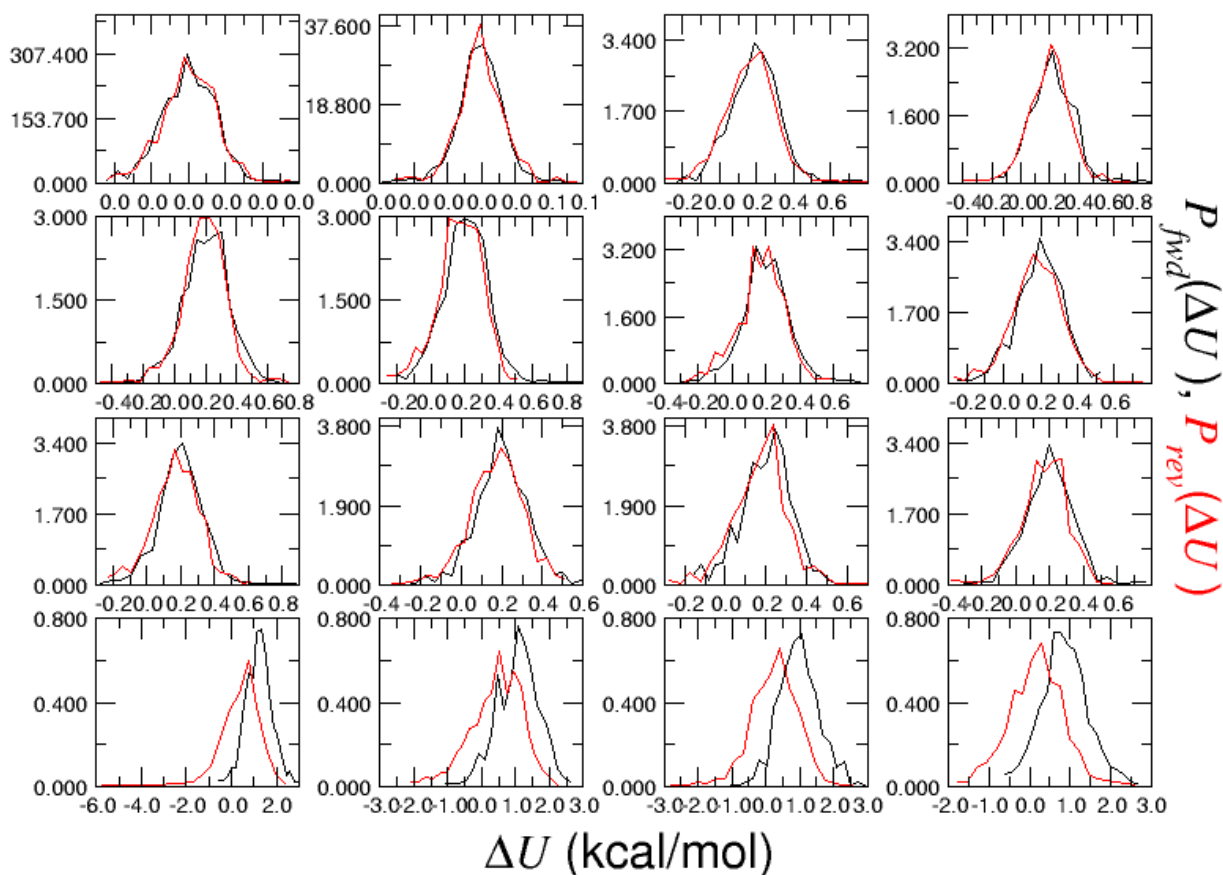
Figure 2.3.3.2.1: Probability distributions for the deprotonation of the ISC center model
Probability distributions of 16 nonlinear windows (λ=0 to λ=0.5) for the deprotonation of
an imidazole ligand to the ISC center model in water. The forward and reverse reactions
are shown in black and red, respectively. More overlap between distributions calculated
for perturbations in the forward and reverse directions corresponds to better sampling,
thus indicating convergence with respect to simulation time within each window.
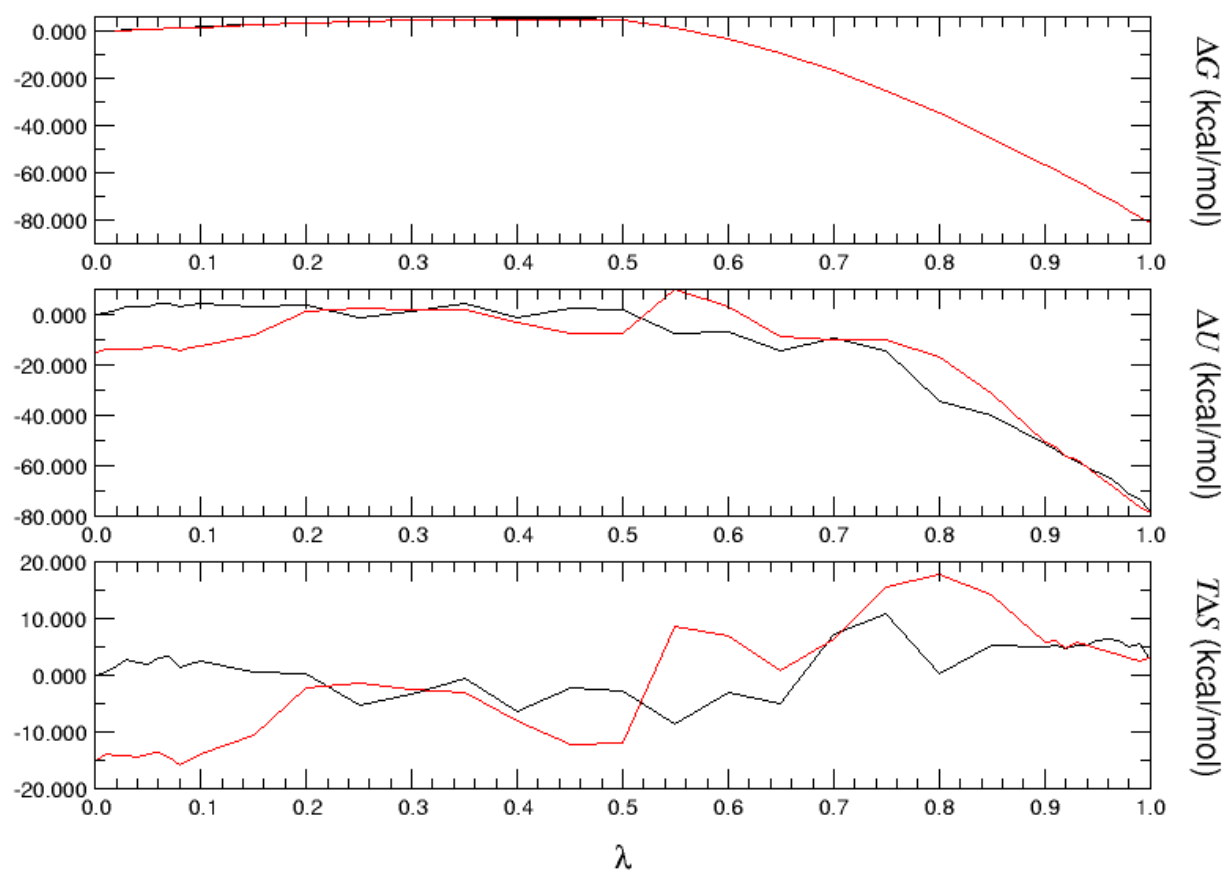
Figure 2.3.3.2.2: Summary of the bidirectional FEP simulations for the deprotonation of the Rieske ISC center model

The forward and reverse reactions are shown in black and red, respectively. For the change in free energy, there is excellent overlapping of the energies in both directions. The changes in internal energy can be approximated and show good agreement in the forward and backward reactions. The changes in entropy can also be estimated from the extended FEP formalism, however entropies are intrinsically harder to approximate and thus less accurate than free energies.

FEP calculations for the deprotonation of an imidazole ring in the oxidized ISC center model in water returned a free energy change of -82.2 ± 0.1 kcal/mol. FEP calculations for the deprotonation of His141 (while His161 is protonated) of the cluster in the protein resulted in a free energy change of -79.8 ± 0.1 kcal/mol and deprotonation of His161 (while His141 is protonated) in the protein resulted in a free energy change of -77.9 ± 0.1 kcal/mol. The free energy differences for deprotonating the His141 and His161 side chains in the protein environment, with full protein dynamics incorporated, relative to the free energy of His deprotonation in water are $\Delta\Delta G = 2.4 \pm 0.1$ and 4.3 ± 0.1 kcal/mol, respectively. Consequently the pKa's of His141 and His161 coordinated to the ISC in the protein shift up from the pKa values of the ISC center model in water by +1.7 and +3.1 pKa units, respectively. Thus, FEP simulations imply that the pKa of His161 is higher than that of His141 in cyt bc1.

It is widely known and accepted that in the oxidized ISC, both iron-ligated histidines are partially protonated and thus titrate over a wide range of pH (26, 49). Our FEP calculations show that His141 and His161 can titrate over the pH range 7.7 < pH < 9.1 with at least one histidine remaining protonated. The titration curve of the two residues can then be divided into three regions as showed in scheme 1: (1) at low pH (< 6.5), both His141 and His161 are protonated; (2) at intermediate pH (7.7 < pH < 9.1), one of the iron-ligated His is protonated; and (3) at high pH (> 9.1) both histidines are deprotonated. From our FEP simulations, the largest concentration of ISC centers appears to be singly deprotonated above physiological pH, but below a pH of approximately 9.

pH < 6.5

$$[2\text{Fe-2S}]^0_{ox} \begin{smallmatrix} \text{His141-H} \\ \\ \text{His161-H} \end{smallmatrix} \quad + e^- \longrightarrow [2\text{Fe-2S}]^{-1}_{red} \begin{smallmatrix} \text{His141-H} \\ \\ \text{His161-H} \end{smallmatrix}$$

7.6 < pH < 9.1

$$[2\text{Fe-2S}]^0_{ox} \begin{smallmatrix} \text{His141}^- \\ \\ \text{His161-H} \end{smallmatrix} \quad + e^- + H^+ \longrightarrow [2\text{Fe-2S}]^{-1}_{red} \begin{smallmatrix} \text{His141-H} \\ \\ \text{His161-H} \end{smallmatrix}$$

$$[2\text{Fe-2S}]^0_{ox} \begin{smallmatrix} \text{His141-H} \\ \\ \text{His161}^- \end{smallmatrix} \quad + e^- + H^+ \longrightarrow [2\text{Fe-2S}]^{-1}_{red} \begin{smallmatrix} \text{His141-H} \\ \\ \text{His161-H} \end{smallmatrix}$$

pH > 9.1

$$[2\text{Fe-2S}]^0_{ox} \begin{smallmatrix} \text{His141}^- \\ \\ \text{His161}^- \end{smallmatrix} \quad + 2e^- + 2H^+ \longrightarrow [2\text{Fe-2S}]^{2-}_{red} \begin{smallmatrix} \text{His141-H} \\ \\ \text{His161-H} \end{smallmatrix}$$

Scheme 1: Three pH ranges (pH < 6.5, 7.6 < pH < 9.1 and pH > 9.1) of the titration curve for the iron-ligated histidines of the Rieske ISP. Both His141 and His161 can titrate over a large pH range. The protein most likely spends a significant time in the singly deprotonated state at physiological pH, which is required for the Rieske ISP to accept a proton and electron.

Our FEP results confirm CPHMD simulations implying that if one of the iron-ligated histidines is deprotonated at physiologically pH, it is His141 and not His161. To test how likely it is for both His161 and His141 to be deprotonated, FEP calculations for the deprotonation of the second imidazole ring (after the first ring has been deprotonated) were also performed for the oxidized ISC center model in water. The calculated free energy change is -115.8 ± 0.4 kcal/mol. FEP calculations for the analogous deprotonation

of His161 while His141 is deprotonated result in a free energy change of -76.3 ± 0.2 kcal/mol. The free energy differences for deprotonating the His161 while His141 is unprotonated, in the protein environment, with full protein dynamics incorporated, relative to the free energy of that same deprotonation in water are $\Delta\Delta G = +39.5 \pm 0.4$ (kcal/mol). Thus, it is energetically very costly to deprotonate His161 after His141 is already deprotonated in the protein. Substitution of the calculated value of $\Delta\Delta G$ into equation (7) yields a shift of $\Delta pKa = 28.8$. Thus, the fraction of ISC cluster with both His161 and His141 deprotonated in the protein, obtained by substituting this calculated value of ΔpKa into equation (8), is negligible and equal to

$$\frac{K_a^{prot}}{K_a^{aq}} = 10^{-\Delta pKa} = 10^{-28.8}$$

In summary, our FEP results, with protein dynamics fully incorporated, give pKa shifts of +1.7 and +3.1 for His141 and His16, respectively. FEP simulations also show that fraction of deprotonated His161 and His141 is negligible, implying that at least one histidine must remain protonated at physiological pH.

Different pKa shifts for His141 and His161 partially attributed to conformational dynamics of the protein near the ISC

In our FEP simulations to remove a proton from either His141 or His161, we observe that both residues are fully exposed to water, although the local environment around His141 is more hydrophobic than the environment of His161. In particular, His141 remains within 3.0Å of Pro175 and Pro177 throughout the simulation. The more hydrophobic environment of His141energetically favors the neutral form, i.e, the form deprotonated at Nε. Moreover, in the X-ray diffraction structure used to initiate our simulations, and also used for published DFT-CE calculations, (50) the backbone nitrogen atom of Cys160 is

3.71Å from the sulfur on Cys158 and 5.73Å from the $N\varepsilon$ atom of His161. We observe, however, that during our FEP simulations the Cys160 side chain moves to within ~3.25Å of the $N\varepsilon$ of His161, while also maintaining a distance less than ~3.7Å from the sulfur atom of the iron-ligated Cys158. The Cys160 side chain maintained these distances for almost the entire 40 ns of simulation time.

Figure 2.3.2.2.3a shows multiple snapshots of the Cys160 side chain near the ISC center inside the protein and Figure 2.3.2.2.3c shows the distances from Cys160 to Cys161 and Cys158 throughout the FEP simulations to deprotonate His141. As His141 is alchemically transformed from the protonated to deprotonated states, the $N\varepsilon$ of His161 remains within a hydrogen bonding distance (≤ 3.25Å) of the Cys160 sulfur atom, a contact that most likely stabilizes the protonated state of His161. At the same time, Cys160 maintains its close distance (3.7Å) to the Cys158 sulfur atom. These conformational dynamics observed in simulations to deprotonate His141 are also consistent with our results from the FEP simulations to deprotonate His161. As His161 alchemically transforms from the protonated to deprotonated form, the $N\varepsilon$ of His161 moves away from the Cys160 sulfur atom. In the time between 17 ns and 32 ns, the two atoms maintain a separation greater than 4Å and their separation fluctuates dramatically. Upon deprotonation of His161, Cys160 also moves further away from Cys158. Figure 2.3.3.2.3b shows multiple snapshots of the Cys160 side chain near the ISC center inside the protein and Figure 2.3.3.2.3d shows the distances from Cys160 to Cys161 and from Cys160 to Cys158 throughout the FEP simulation to deprotonate His161. The dynamics of Cys160 side chain thus provides a qualitative, dynamical reason why His161 has a higher pKa than His141 in the protein environment.
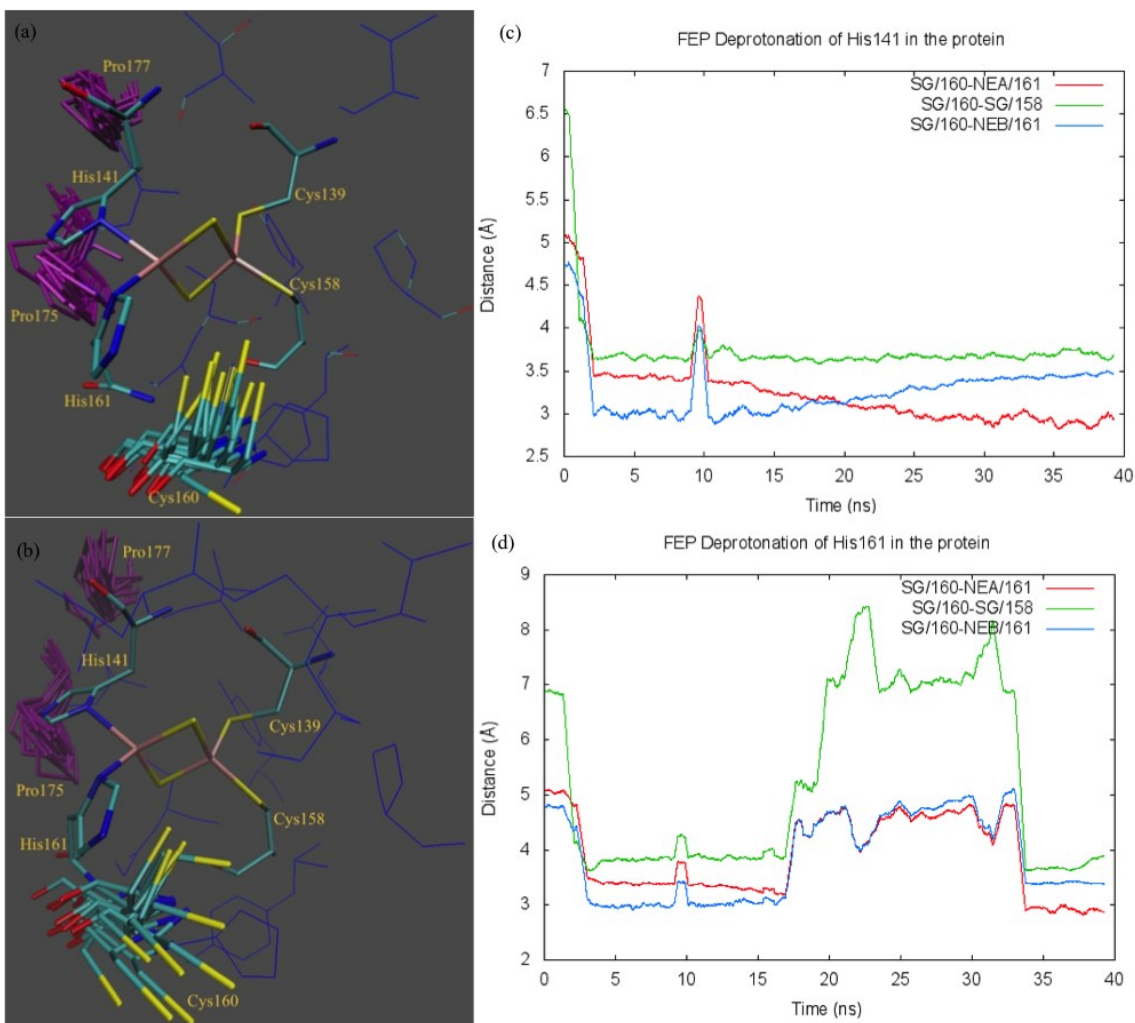
Figure 2.3.3.2.3: Multiple frames from trajectories for Cys160, Pro175, and Pro177 from

FEP simulations

Multiple frames from FEP simulation to deprotonate His141 (2.3.2.2.3a) and His161

(2.3.3.2.3b) show Cys160, Pro175 (purple), and Pro177 (purple). In the FEP simulation

to deprotonate His141, the Cys160 sulfur atom remains within hydrogen bond distance

(<3.5Å) of the Nε on His161 and helps stabilize His161 in the protonated form, while

maintaining a close distance to Cys158 (2.3.2.2.3c). In the FEP simulation to deprotonate

His161, Cys160 moves away from both the deprotonated His161 and the Cys158 and

these distances fluctuate dramatically (2.3.2.2.3d).

52

2.3.4. Implications for the mechanism(s) of QH2 oxidation: function in terms of His161 protonation states

Our pKa calculations using both the CPHMD and FEP methods result in a higher pKa for the iron-ligated His161 than for His141. The pKa value of His161 is approximately 9 implying that His161 is protonated at physiological pH. Our simulations therefore do not support the hypothesis of Crofts et al. (21-23) of a sequential proton coupled electron transfer mechanism that requires a deprotonated His161 to serve as hydrogen bond acceptor, stabilize QH2 as a hydrogen bond donor, and act as the first proton acceptor in QH2 oxidation. On the other hand, our CPHMD simulations provide a pKa value of 5.1 for the Glu271 so that Glu271 is most likely deprotonated at physiological pH. Our results therefore support the kinetic study of Covian et al. (24, 25) that an acidic amino acid with pKa ~5.2-5.7 must be deprotonated in order for the initial QH2 oxidation to occur and this acidic amino acid is most probably Glu271 of cytochrome b.

2.4. Conclusions

Our titrations in the protein using the CPHMD method report the pKa values of amino acid side chains near the Qi and Qo binding sites and for the first time differentiate the iron-ligated histidines of the ISP. The computed pKa value of residue Glu271 of cytochrome b near the Qo site in the protein environment is 5.1. The result is in good agreement with the experimentally measured pKa values of 5.2 and 5.7, measured from the effects of pH on the binding affinity of the quinone analogues decylbenzoquinone and decylbenzoquinol, respectively (24). Our result provide supporting evidence for the authors' hypothesis that an acidic amino acid residue, probably Glu271, near the Qo site has to be deprotonated for the QH2 oxidation to occur. We confirm that the unprotonated

acidic amino acid residue is Glu271. is the simulations imply that the Glu271 can play the role of the first proton acceptor in the QH2 oxidation at the Qo site.

The computed pKa values for His201, Asp228 and Lys227 near the Qi binding site are 6.7, 3.9 and 8.9, respectively. Thus, in the protein at physiological pH, His201 is mostly singly protonated and certainly capable of playing the role of hydrogen bond donor to the UQ. Our results also give direct evidence that Asp228 in the protein near pH 7 is deprotonated and thus cannot act as a hydrogen bond donor. However, with water accessibility to the site, Asp228 is very likely to form a water-bridged hydrogen bond to UQ bound in the Qi site. The computed pKa value for Lys227 is 8.9 and provides direct evidence that Lys227 is protonated in the protein at pH near 7. However, a pKa shift of -1.5 pKa units comparing to a free lysine in water implies that Lys227 is buried in the protein and not likely to play a role in fetching water molecule(s) from solvent to the Qi site as suggested by Gao et al., (16) but consistent with the proposal by Lange et al. in the yeast complex (13).

We also differentiate the pKa values of the iron-ligated histidines of the Rieske ISP for the first time, using CPHMD. The computed pKa value for His141 is 7.8 ± 0.5 and that for His161 is 9.1 ± 0.6. Our results are in good agreement of the experimentally measured pKa values of 7.63 ± 0.15 and 9.16 ± 0.28 (26) and the pKa values of 6.9 and 8.8 (28) calculated by using DFT-CE methods, although neither published study was able to assign pKa values to specific, individual histidines. FEP simulations of the Rieske ISP reported here show that pKa shifts of the His141 and His161 ligands to the Rieske iron-sulfur cluster, upon moving the cluster from water to the protein are 1.7 ± 0.1 and 3.1 ± 0.1, respectively. These results provide additional evidence supporting our CPHMD

simulations that His161 indeed has a higher pKa than His141 in the protein. Structural analysis of the dynamics trajectory partially attributes the higher pKa of His161 to hydrogen bonding contacts between the Nε atom of His161 and the sulfur atom of Cys160. Assigning the lower pKa value to His141 and not His161 supports proposals that the protonation state of the residue with a measured pKa of ~7.5 (His141) is independent of the ubiquinol binding affinity at the Qo site (24). Although we acknowledge that proton transfer does not necessarily occur from the most thermodynamically stable state, our results appear to contradict the sequential mechanism of QH2 oxidation initiated by proton transfer to a deprotonated His161 at the Qo site (21-23)

Acknowledgements

References

1. Gray MW, Burger G, Lang BF. The origin and early evolution of mitochondria. Genome Biol. 2001;2(6):REVIEWS1018.

2. Cape JL, Bowman MK, Kramer DM. A semiquinone intermediate generated at the qo site of the cytochrome bc1 complex: Importance for the q-cycle and superoxide production. Proc Natl Acad Sci U S A. 2007;104(19):7887-92.

3. Droese S, Brandt U. The mechanism of mitochondrial superoxide production by the cytochrome bc1 complex. J Biol Chem. 2008;283(31):21649-54.

4. Muller F, Crofts AR, Kramer DM. Multiple Q-cycle bypass reactions at the qo site of the cytochrome bc1 complex. Biochemistry. 2002;41(25):7866-74.

5. Zhang L, Yu L, Yu C. Generation of superoxide anion by succinate-cytochrome c reductase from bovine heart mitochondria. J Biol Chem. 1998;273(51):33972-6.

6. Yin Y, Yang S, Yu L, Yu C. Reaction mechanism of superoxide generation during ubiquinol oxidation by the cytochrome bc1 complex. J Biol Chem. 2010;285(22):17038-45.

7. Berry EA, Huang L, Lee D, Daldal F, Nagai K, Minagawa N. Ascochlorin is a novel, specific inhibitor of the mitochondrial cytochrome bc1 complex. Biochim Biophys Acta, Bioenerg. 2010;1797(3):360-70.

8. Fernandez-Ortuno D, Tores JA, de Vicente A, Perez-Garcia A. Mechanisms of resistance to QoI fungicides in phytopathogenic fungi. Int Microbiol. 2008;11(1):1-9.

9. Looareesuwan S, Chulay JD, Canfield CJ, Hutchinson DBA. Malarone (atovaquone and proguanil hydrochloride): A review of its clinical development for treatment of malaria. Am J Trop Med Hyg. 1999;60(4):533-41.

10. Farnert A, Lindberg J, Gil P, Swedberg G, Berqvist Y, Thapar MM, et al. Evidence of plasmodium falciparum malaria resistant to atovaquone and proguanil hydrochloride: Case reports. Bmj. 2003;326(7390):628-9.

11. Kessl JJ, Lange BB, Merbitz-Zahradnik T, Zwicker K, Hill P, Meunier B, et al. Molecular basis for atovaquone binding to the cytochrome bc1 complex. J Biol Chem. 2003;278(33):31312-8.

12. Maloney PC, Kashket ER, Wilson TH. Protonmotive force drives ATP synthesis in bacteria. Proc Natl Acad Sci U S A. 1974;71(10):3896-900.

13. Lange C, Nett JH, Trumpower BL, Hunte C. Specific roles of protein-phospholipid interactions in the yeast cytochrome bc1 complex structure. Embo J. 2001;20(23):6591-600.

14. Hunte C, Koepke J, Lange C, Rossmanith T, Michel H. Structure at 2.3 Ã… resolution of the cytochrome bc1 complex from the yeast saccharomyces cerevisiae co-crystallized with an antibody fv fragment. Structure (London). 2000;8(6):669-84.

15. Huang L, Cobessi D, Tung EY, Berry EA. Binding of the respiratory chain inhibitor antimycin to the mitochondrial bc1 complex: A new crystal structure reveals an altered intramolecular hydrogen-bonding pattern. J Mol Biol. 2005;351(3):573-97.

16. Gao X, Wen X, Esser L, Quinn B, Yu L, Yu C, et al. Structural basis for the quinone reduction in the bc1 complex: A comparative analysis of crystal structures of mitochondrial cytochrome bc1 with bound substrate and inhibitors at the qi site. Biochemistry. 2003;42(30):9067-80.

17. Lee MS, Salsbury FR, Jr., Brooks CL,III. Constant-pH molecular dynamics using continuous titration coordinates. Proteins: Struct , Funct , Bioinf. 2004;56(4):738-52.

18. Esser L, Quinn B, Li Y, Zhang M, Elberry M, Yu L, et al. Crystallographic studies of quinol oxidation site inhibitors: A modified classification of inhibitors for the cytochrome bc1 complex. J Mol Biol. 2004;341(1):281-302.

19. Iwata S, Lee JW, Okada K, Lee JK, Iwata M, Rasmussen B, et al. Complete structure of the 11-subunit bovine mitochondrial cytochrome bc1 complex. Science (Washington, D C). 1998;281(5373):64-71.

20. Trumpower BL. A concerted, alternating sites mechanism of ubiquinol oxidation by the dimeric cytochrome bc1 complex. Biochim Biophys Acta, Bioenerg. 2002;1555(1-3):166-73.

21. Crofts AR, Barquera B, Gennis RB, Kuras R, Guergova-Kuras M, Berry EA. Mechanism of ubiquinol oxidation by the bc1 complex: Different domains of the quinol

binding pocket and their role in the mechanism and binding of inhibitors. Biochemistry. 1999;38(48):15807-26.

22. Crofts AR, Hong S, Ugulava N, Barquera B, Gennis R, Guergova-Kuras M, et al. Pathways for proton release during ubihydroquinone oxidation by the bc1 complex. Proc Natl Acad Sci U S A. 1999;96(18):10021-6.

23. Crofts AR. The cytochrome bc1 complex: Function in the context of structure. Annu Rev Physiol. 2004;66:689,733, 4 plates.

24. Covian R, Moreno-Sanchez R. Role of protonatable groups of bovine heart bc1 complex in ubiquinol binding and oxidation. Eur J Biochem. 2001;268(22):5783-90.

25. Covian R, Trumpower BL. The rate-limiting step in the cytochrome bc1 complex (ubiquinol-cytochrome c oxidoreductase) is not changed by inhibition of cytochrome b-dependent deprotonation: Implications for the mechanism of ubiquinol oxidation at center P of the bc1 complex. J Biol Chem. 2009;284(21):14359-67.

26. Link TA, Hagen WR, Pierik AJ, Assmann C, Von Jagow G. Determination of the redox properties of the rieske [2Fe-2S] cluster of bovine heart bc1 complex by direct electrochemistry of a water-soluble fragment. Eur J Biochem. 1992;208(3):685-91.

27. Baymann F, Robertson DE, Dutton PL, Maentele W. Electrochemical and spectroscopic investigations of the cytochrome bc1 complex from rhodobacter capsulatus. Biochemistry. 1999;38(40):13188-99.

28. Ullmann GM, Noodleman L, Case DA. Density functional calculation of pKa values and redox potentials in the bovine rieske iron-sulfur protein. JBIC, J Biol Inorg Chem. 2002;7(6):632-9.

29. Zu Y, Couture MM-, Kolling DRJ, Crofts AR, Eltis LD, Fee JA, et al. Reduction potentials of rieske clusters: Importance of the coupling between oxidation state and histidine protonation state. Biochemistry. 2003;42(42):12400-8.

30. Gurbiel RJ, Doan PE, Gassner GT, Macke TJ, Case DA, Ohnishi T, et al. Active site structure of rieske-type proteins: Electron nuclear double resonance studies of isotopically labeled phthalate dioxygenase from pseudomonas cepacia and rieske protein from rhodobacter capsulatus and molecular modeling studies of a rieske center. Biochemistry. 1996;35(24):7834-45.

31. Bertrand P, Guigliarelli B, Gayda JP, Beardwood P, Gibson JF. A ligand-field model to describe a new class of iron-sulfur (2Fe-2S) clusters in proteins and their synthetic analogs. Biochim Biophys Acta, Protein Struct Mol Enzymol. 1985;831(2):261-6.

32. Lin I, Chen Y, Fee JA, Song J, Westler WM, Markley JL. Rieske protein from thermus thermophilus: 15N NMR titration study demonstrates the role of iron-ligated histidines in the pH dependence of the reduction potential. J Am Chem Soc. 2006;128(33):10672-3.

33. Onufriev A, Case DA, Ullmann GM. A novel view of pH titration in biomolecules. Biochemistry. 2001;40(12):3413-9.

34. Zwanzig RW. High-temperature equation of state by a perturbation method. I. nonpolar gases. J Chem Phys. 1954;22:1420-6.

35. Humphrey W, Dalke A, Schulten K. VDM: Visual molecular dynamics. J Mol Graphics. 1996;14(1):33,8, plates, 27-28.

36. Brooks BR, Bruccoleri RE, Olafson BD, States DJ, Swaminathan S, Karplus M. CHARMM: A program for macromolecular energy, minimization, and dynamics calculations. J Comput Chem. 1983;4(2):187-217.

37. MacKerell AD, Jr., Feig M, Brooks CL,III. Improved treatment of the protein backbone in empirical force fields. J Am Chem Soc. 2004;126(3):698-9.

38. Jorgensen WL, Chandrasekhar J, Madura JD, Impey RW, Klein ML. Comparison of simple potential functions for simulating liquid water. J Chem Phys. 1983;79(2):926-35.

39. Essmann U, Perera L, Berkowitz ML, Darden T, Lee H, Pedersen LG. A smooth particle mesh ewald method. J Chem Phys. 1995;103(19):8577-93.

40. Phillips JC, Braun R, Wang W, Gumbart J, Tajkhorshid E, Villa E, et al. Scalable molecular dynamics with NAMD. J Comput Chem. 2005;26(16):1781-802.

41. Sugita Y, Okamoto Y. Replica-exchange molecular dynamics method for protein folding. Chem Phys Lett. 1999;314(1,2):141-51.

42. Khandogin J, Brooks CL,III. Toward the accurate first-principles prediction of ionization equilibria in proteins. Biochemistry. 2006;45(31):9363-73.

43. Wallace JA, Wang Y, Shi C, Pastoor KJ, Nguyen B, Xia K, et al. Toward accurate prediction of pKa values for internal protein residues: The importance of conformational relaxation and desolvation energy. Proteins: Struct , Funct , Bioinf. 2011;79(12):3364-73.

44. Khandogin J, Brooks CL,III. Constant pH molecular dynamics with proton tautomerism. Biophys J. 2005;89(1):141-57.

45. Pohorille A, Jarzynski C, Chipot C. Good practices in free-energy calculations. J Phys Chem B. 2010;114(32):10235-53.

46. Liu P, Dehez F, Cai W, Chipot C. A toolkit for the analysis of free-energy perturbation calculations. J Chem Theory Comput. 2012;8(8):2606-16.

47. Shepherd RE. Association of imidazoles and L-histidine with the pentacyanoiron(II) and -(III) moieties. J Am Chem Soc. 1976;98(11):3329-35.

48. Kokhan O, Shinkarev VP. All-atom molecular dynamics simulations reveal significant differences in interaction between antimycin and conserved amino acid residues in bovine and bacterial bc1 complexes. Biophys J. 2011;100(3):720-8.

49. Zu Y, Fee JA, Hirst J. Complete thermodynamic characterization of reduction and protonation of the bc1-type rieske [2Fe-2S] center of thermus thermophilus. J Am Chem Soc. 2001;123(40):9906-7.

50. Iwata S, Saynovits M, Link TA, Michel H. Structure of a water soluble fragment of the 'rieske' iron-sulfur protein of the bovine heart mitochondrial cytochrome bc1 complex determined by MAD phasing at 1.5 A resolution. Structure. 1996;4(5):567-79.

CHAPTER 3

NON-POLAR CONTACTS, RATHER THAN HYDROGEN BONDS, BIND

UBIQUINOL NEAR THE Q_O SITE

Abstract

The cytochrome bc1 complex is essential for the mitochondrial respiration chain. It

operates by a prototypical "Q-cycle" and catalyzes electron transfer from ubiquinol

(QH2) to cytochrome c, coupled to the translocation of protons, generating a proton

gradient that drives ATP synthesis. Although the Q-cycle is widely accepted as the model

that best describes how electrons/protons flow in the cyt bc1 complex, QH2 has never

been captured at the Qo site in X-ray diffraction structures, thus structural driving factors

of many intermediate steps remain controversial. We used molecular dynamic

simulations to exam the binding geometries of QH2. Among several competing proposals

for the mechanism of the coupled electron and proton transfer in cyt bc1 is one based on

an X-ray structure with bound Stigmatellin (SMA) requiring a deprotonated His161

(ligated to the Rieske iron-sulfur cluster) to form a hydrogen bond to the Ubiquinol and

Glu271 of cytochrome b. To test the hypothesis that deprotonated His161 is hydrogen-

bonded to ubiquinol, we placed a QH2 model in the Qo site by overlapping the SMA in a

way to form hydrogen bonds to the deprotonated epsilon nitrogen of His161 and the

carboxylate oxygen of Glu271. Equilibrated structures show no hydrogen bond to the

QH2. Instead we identify a pocket of non-polar residues formed by alpha helices within

4Å of the QH2 and their nonpolar side chains define a binding pocket for QH2. The role

of mobile water molecules in breaking the hydrogen bonds from QH2 to amino acid side chains near the Qo site will be discussed.

3.1. Introduction

3.1.1. Mitochondrial cytochrome bc1 complex operates by a modified Q-cycle

The mitochondrial cyt bc1 complex catalyzes the bifurcated electron transfer from ubiquinol at the Qo site to the high potential cytochrome c and to the low potential cytochrome b, where the electrons reduce ubiquinone to ubiquinol at the Qi site, in two turnovers. The electron transfer coupled to the translocation of protons across the mitochondrial inner membrane generates a proton gradient that drives ATP synthesis. This type of proton coupled electron transfer reaction was suggested by Mitchell to operate by a prototypical "Q-cycle" (1).
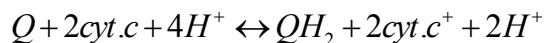
$$Q + 2cyt.c + 4H^+ \leftrightarrow QH_2 + 2cyt.c^+ + 2H^+$$

A modified Q-cycle (Figure 1.2.2) is necessary to describe the bifurcated electron transfer mechanism. For a complete reduction of one UQ at the Qi site (uptake of two protons), there must be two oxidation events of QH2 at the Qo site (release of four protons) and thus the net result is two protons translocated across the mitochondrial inner membrane. Thus, there are several possible scenarios: (1) after oxidation of QH2 to UQ, UQ will have to exit the Qo site and exchange with another QH2 in the QH2/UQ pool or (2) there must be two bound QH2 molecules at the Qo site for one turnover of UQ; or (3) the most recent work by Mulkidjanian (2) proposes an activated Q-cycle for a dimer model, in which there is a continuously bound semiquinone (Q•-) at the Qi site of one monomer and a reduced heme bL near the Qo site of the other monomer. The oxidation of each

QH2 at the Qo site then yields a UQ at the Qi site and two proton transfers across the membrane. Regardless which scenario may be true, the Q-cycle accounts for the bifurcated electron coupled proton transfer across the mitochondrial inner membrane (3). It remains uncertain, however, whether each proton and electron transfer to oxidize QH2 at the Qo site proceeds by a concerted or a sequential mechanism.

3.1.2. Structure of cytochrome b

The cytochrome b of the cyt bc1 complex consists of eight trans-membrane helices (Figure 3.1.2) named A to H and four loops connecting them: AB, CD, DE and EF. The CD loop consists of two short helices cd1 and cd2. The AB and EF loops each have one helix and the DE loop has no secondary structure (4). These helices form two helical bundles spanning the membrane. The first helical bundle has five helices (A-E) and contains the two b-type hemes. The second bundle has three helices F-H (4-6). This contribution will discuss the binding of QH2 near the Qo site that rests at the interface between the ISP and cytochrome b and embedded toward the interior of the second helical bundle in cytochrome b.
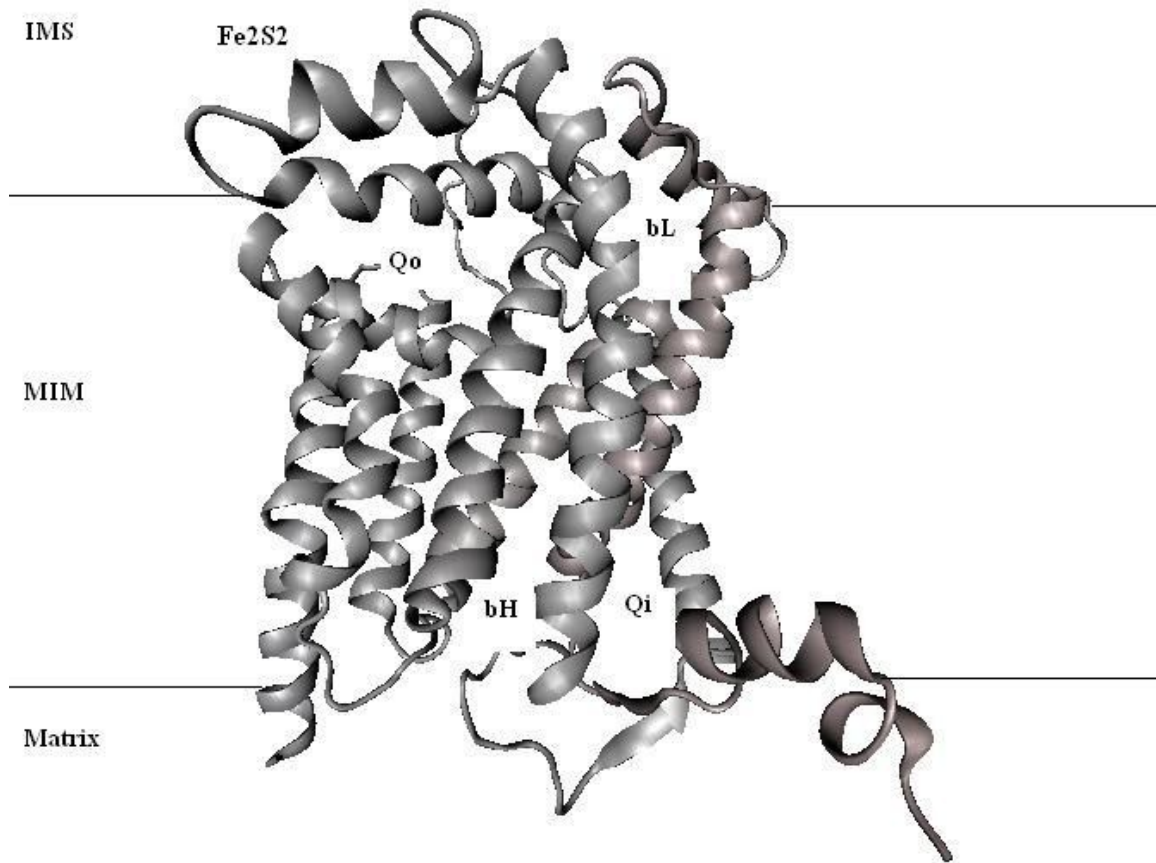
Figure 3.1.2: The cytochrome bc1 complex spans the mitochondrial inner membrane (MIM). Fe2S2 denotes where the iron-sulfur cluster of the Rieske protein is located, near the inner membrane space (IMS). bL and bH denote the locations of the low potential and high potential b-type hemes, respectively, and the catalytic centers are Qo and Qi. (PDB code 1PP9. Graphic representation was prepared with VMD (7).)

We should mention that the cyt bc1 complex not only functions as an electrons transfer protein, but also as a major source of reactive oxygen species (ROS) (8, 9). It is hypothesized that semiquinone (SQ) intermediate radicals can form when electrons

shuttle through UQ/QH2 and the metal centers, or when the bifurcated reaction at the Qo site is disrupted (8, 10). This radical is very reactive and will react with any oxygen species (O_2 or H_2O) nearby to form ROS that can harm the cells. Under normal conditions, the efficiency of cyt bc1 surpasses any bypass reactions that might result in a wasteful electron transfer. It is naturally to think that the cyt bc1 complex conformational dynamics are responsible for ensuring that the reactive SQ is shielded from the oxygen species by maximizing the efficiency in electron transfer to cyt c. General defects of the mitochondrial cyt bc1 complex certainly result in shutting off the electron transfer chain (ETC) and, ultimately, cell death. Particularly, inhibitors at the Qo site not only disrupt the ETC but also result in ROS production. It is believed that the ROS are commonly found in oxidatively stressed cell, inducing apoptosis (9). Therefore, any defect of the bifurcated electron transfer at the Qo site is likely the cause of ROS production in mitochondrial cytochrome bc1 (9, 11, 12). The cyt bc1 complex is therefore a desirable target for anti-fungal (13), anti-malaria and anti-pneumonia therapeutics (14-16).

3.1.3. Qo site defined by X-ray structures with various bound inhibitors

Although the structures of cyt bc1 complexes have been extensively studied using X-ray crystallography, to our knowledge there is no known structure with any ubiquinol species at the Qo site. Instead, ivestigations of the QH2 binding geometries using X-ray crystallographic studies with various bound inhibitors were conducted to infer the binding site and geometry of QH2 (5, 6, 17-19). The competitive inhibitor of QH2, stigmatellin (SMA), has received the most attention and shows two hydrogen bonds, one to the Glu271 of cyt b and one to His161 of the ISP. Not only was such a complex observed in X-ray crystallographic studies, but one study using FTIR spectroscopy was

68

consistent with such hydrogen bonding (20). Based on the structure of SMA bound near the Qo site of cyt bc1, it has been inferred that QH2 binds in the same location. This binding site places one hydroxyl group of QH2 within a hydrogen bonding distance of the epsilon nitrogen of His161and the other hydroxyl group of QH2 within hydrogen bonding distance of a carboxylic oxygen of Glu271, either directly or through a water molecule in contact with the side chain of Glu271. This binding geometry would presumably allow His161 and Glu271 to serve as proton acceptors in the QH2 oxidation. This hypothesis is commonly accepted in both concerted and sequential mechanisms of electron-coupled proton transfer (21, 22). For example, Crofts et al. proposed a sequential mechanism with deprotonated His161 as the first proton acceptor (22-24). In contrast, Trumpower proposed that a hydrogen bond from a hydroxyl group of QH2 replaces a proton on the epsilon nitrogen of His161 in the first step of the mechanism (21) and Covian et al. proposed that Glu271 is the first proton acceptor in a concerted reaction and no hydrogen bond between His161 and QH2 is required to stabilize QH2 binding (25, 26). Direct evidence that the deprotonation of His161 is required for QH2 oxidation and that a hydrogen bond exists between deprotonated His161 and ubiquinol is lacking. The current work investigates the putative hydrogen bond between the deprotonated His161 of the ISP and the hydroxyl hydrogen atom of QH2, as well as the hydrogen bond between deprotonated Glu271 of cyt b and the second hydroxyl hydrogen atom of QH2.

3.1.4. Structure-based hypotheses for the coupled electron and proton transfer mechanism near the Qo site

At the moment, it is commonly agreed among workers in the field that a modified Q-cycle describes the electron/proton flow in cyt bc1. Details of the QH2 oxidation

mechanism at the Qo site, as well as the QH2 binding site and geometry near the Qo binding pocket are still subjects of intense debate. Extensive kinetic and thermodynamic studies have provided data that can be interpreted to support several different mechanistic hypotheses, whereas direct structural data remain elusive.

Proposed mechanisms of Electron Coupled Proton Transfer

A variety of mechanisms for electron-coupled proton transfer (ECPT) in cyt bc1 have been proposed based on published structural, thermodynamic, and kinetic data. The various proposed mechanisms differ in important details and often require different structural features. Crofts et al. proposed, for example, that the first electron-coupled proton transfer to the ISC occurs via a hydrogen bond between deprotonated His161 and QH2, thus producing, after subsequent electron transfer, a neutral semiquinone radical (QH•) at the catalytic site. This intermediate then transfers a proton to the Glu271 carboxylate group. This action triggers the movement of the semiquinone intermediate to a position closer to the heme bL and an electron is subsequently transferred to reduce cytochrome b (22-24). This hypothesis proposed that QH2 oxidation initiates with QH2 docked and engaged in two hydrogen bonds, one to deprotonated His161 and one to deprotonated Glu271. The protonation state of His161 and the hydrogen bond it forms with the substrate are critical for this mechanism. Moreover, the authors needed to provide a well-reasoned explanation for how the cyt bc1 complex avoids any bypass reactions, since the putative semiquinone radical intermediate would be so reactive as a reductant that it would readily perform wasteful electron transfer. Crofts et al. proposed a gating mechanism in which the protonated Glu271 would rotate out of the Qo site to deliver its proton to a water molecule in the aqueous phase. These actions lead to the

movement of the anionic semiquinone radical (QH•-) to a position near heme bL, the

proximal domain (22, 23, 27). The authors suggested that such movement requires

conformational changes, thus contributing to the high activation energy of the second

electron transfer step and preventing the radical(s) from reacting in bypass reactions with

oxygen species. In this hypothesis, the anionic radical can only move closer to the

oxidized heme bL because, if bL were in a reduced state, it could further reduce the

semiquinone, resulting in unproductive electron transfer. In addition to that apparent

problem, the ISC were now reduced, and if the anionic radical would exert coulombic

repulsion, and push away from the reduced heme bL and toward the ISC, it can re-

oxidized the ISC, also resulting in a wasteful electron transfer. This type of gating model

requires particular redox states for the ISC, the semiquinone and the heme bL to allow

productive electron transfer and prevent wasteful electron transfer in short circuit

reactions. The mechanism proposed by Crofts et al. requires not only constraints on the

oxidation states of the metal centers (ISC and heme) but also on the protein

conformation. Although it is a complicated task to control the electron transfer by this

double-gated mechanism, the specific details proposed provide multiple opportunities to

test the mechanism.

A competing mechanism for QH2 oxidation has been proposed by Trumpower and co-

workers. Their hypothesis proposes that two electrons are transferred simultaneously to

the ISP and cytochrome b via a quinol-imidazolate-carboxylate complex without the

formation of a semiquinone intermediate (21, 28, 29). The quinol-imidazolate-

carboxylate complex is formed by two concerted component reactions: (1) a ubiquinol

hydroxyl group replacing a proton on the epsilon nitrogen of His161 (His181 in yeast) of

the ISP and (2) this quinol-imidazolate then forms a hydrogen bond to residue Glu271 of

cytochrome b. Although the authors realized that the lack of evidence for a semiquinone

intermediate at significant concentrations could not be taken as evidence for a concerted

mechanism, they showed evidence that could fit well with the concerted mechanism.

Their kinetic studies of the reduction rates in the presence and absence of ubiquinone

showed a reciprocal relationship between the high and low potential redox components

i.e., the energy from reduction of the ISC drove the reduction of heme bL (29). Other

kinetic studies by Covian and co-workers (30) showed that the pH dependent activity of

cyt bc1 can be fit with three ionizable groups, His161 and His141 of the ISP, as well as

Glu271 of cyt b. The same authors also concluded that the "Hydrogen bonding to His161

is not the main stabilizing force for the binding of quinine, quinol, and inhibitors" (25).

Moreover, Covian and Trumpower's mutation study of E271Q (eliminating the proton

acceptor Glu271, they argued), showed no change in the activation energy of QH2

oxidation (26). The argument was made that once the proton acceptor function of Glu271

was eliminated, no movement of semiquinone could occur and the rate of the second

electron transfer would slow significantly enough to become rate-limiting. Therefore, no

change in activation energy was interpreted to disprove Crofts et al.'s proposal that

protonation of Glu271 allows movement of the unstable semiquinone to a position close

to heme bL (27) prior to the second electron transfer.

A third hypothesis, by Covian et al. (25, 26, 31) proposed a concerted mechanism similar

to the mechanism proposed by Trumpower et al., but differing in the initiation step for

QH2 oxidation. Covian and co-workers proposed that the first proton is transferred to

Glu271, followed by an electron coupled proton transfer to the ISC, followed by another

electron transfer to reduce cytochrome b and complete the oxidation of a QH2 molecule (25).

Finally, Osyczka et al proposed a concerted two electron transfer without a semiquinone intermediate. Their proposal differs from previously proposed concerted mechanisms because Osyczka et al. proposed 'soft proton management' i.e. proton transfer is mediated by hydrogen bond patterns among mobile water molecules (32, 33). One of the two essential conditions that favor a concerted mechanism over the sequential mechanism is the availability of proton donors and acceptors at the Qo site. While the three proposed mechanisms described above all suggest that Glu271 serves as a proton acceptor (21-25, 30, 34), Osyczka et al. (22, 35) argue that Glu271 (Glu295 in bacteria) might not play the role of the proton acceptor because mutations of Glu271 have little kinetic effects (mutation of E271D has no kinetic effects; E271Q and E271N has modest kinetic effects), show no phenotypic impairment, and display no change in QH2 oxidation activation energy (26). They proposed that bridging water molecules form hydrogen bonds with Glu271 and thus provide "soft proton management".

In summary, it is generally agreed that the Qo binding geometry involves two hydrogen bonds, one to the epsilon nitrogen of His161 in the Iron-Sulfur Protein (ISP) and the other to a carboxyl oxygen of Glu271 of cytochrome b (figure 3.2.1.1). Under this assumption and the assumption that both His161 and Glu271 are deprotonated, they can certainly act as proton acceptors during ubiquinol oxidation. While there is not much doubt about the deprotonation state of Glu271 at physiological pH, the protonation states of the His161 side chain can be challenged. His161 ligates the Iron-Sulfur-Cluster (ISC) together with His141. The two His ligands are symmetrically disposed about the ISC, so they differ

only by virtue of the different protein environments. Additionally, the paramagnetic nature of the ISC broadens ^1H and ^{15}N NMR signals from nitrogen atoms on both ligand histidines, making it a challenge to measure individual pKa values for His161 and His141. Moreover, both His141 and His161 are highly exposed to solvent, and therefore likely to be charged (protonated) and participate in the proton transfer network with water molecules. It is also important to highlight that upon binding of SMA, protein conformations change. Several studies had shown that SMA induced large conformational changes in the cyt bc1complex (18, 36, 37), decreased its mobility (36), and increased order within the ISP soluble domain (37). Meanwhile the hydrogen bonding exhibited in the SMA binding geometry is not necessarily the same as in ubiquinol binding geometries. Therefore, without structural information addressing the QH2 binding geometries at the Qo site, no consensus about the structural factors that promote QH2 oxidation at the Qo site can be reached, and thus the mechanism of QH2 oxidation remains inconclusive. To address structural issues related to the competing electron transfer mechanisms outlined above, our simulations reported here describe the various roles of amino acid side chains, particularly those capable of hydrogen bonding, on the binding site(s) and geometries of QH2 in the Qo binding pocket.

3.2 Material and methods:

3.2.1 Preparation of initial structure and force field
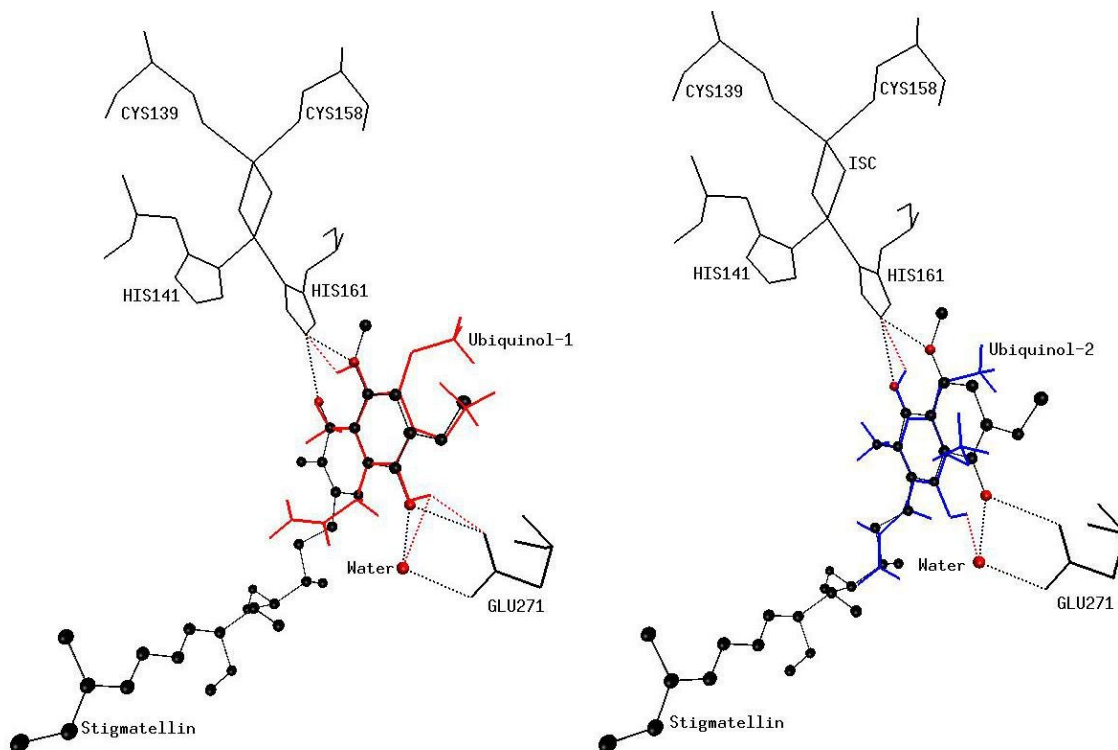
Figure 3.2.1.1 QH2 model overlaps bound stigmatellin (SMA) at the Qo site.

SMA is shown in black, in a ball-and-stick representation. The black dashed lines show

hydrogen bonds from atoms of SMA to the His161 of ISP, Glu271 of cytochrome b and a

water molecule. The Ubiquinol(1) model representing one proposed geometry (solid red

line) was placed by overlapping one of SMA's two fused rings in a way to form hydrogen

bonds to the NE2 atom of His161 and the OE1 atom of Glu271 (red dashed lines). The

Ubiquinol(2) model representing the second proposed geometry (blue line) was placed to

overlap the second of SMA's fused rings in a way to form a hydrogen bond to the NE2 of

His161 and a hydrogen bond to the OE2 atom of Glu271 via a water bridge (red dashed lines). (See text for details).

The starting structure used for MD simulations includes the catalytic core subunits: cytochrome b with two iron-containing hemes and the iron sulfur protein (ISP) head domain with an iron-sulfur cluster (ISC). These subunits were truncated from a bovine cytochrome bc1 complex crystal structure obtained from the Protein Data Bank (http://www.rcsb.org/pdb/home/home.do), PDB ID 1PP9 (38). The 1PP9 structure was selected because of its well defined nature with a resolution of 2.1Å and an R-value of 0.25. We used VMD (7) (http://www.ks.uiuc.edu/Research/vmd/) to prepare the starting structure. The N-terminal and C-terminal were capped with acetylate and amidate, respectively. All hydrogen atoms and heavy atoms missing from the X-ray crystal structure were placed using standard procedures in the CHARMM program and the CHARMM/CMAP force field parameters (39) were used for all atoms of the protein and heme groups. All undefined atoms from the X-ray structure were deleted. Residue His161 of the ISP is deprotonated and residue His141 is protonated at the epsilon nitrogen (NE2). Since both His 141 and 161 ligate one of the iron atoms of the ISC [2Fe-2S] via their delta nitrogens (ND1), a bond connecting the ND1 atom on each residue to the iron atom of the ISC was built using the PATCH command (Figure 3.2.1.1). The partial charges for the ISC center including the ligand residues and their hydrogen bond partners were obtained from the geometry optimization of Ullmann et al., using the DFT-CE method for the oxidized ISC when His161 was deprotonated and His141 was protonated (40). Figure 3.2.1.2 shows atoms with charges obtained from quantum calculation: the ISC, all

atoms of His141 and His161, the beta carbon atom, its hydrogen atoms HB1, HB2 and the SG atom of Cys139 and Cys158, and atoms of the neighboring residues that formed hydrogen bond with them.
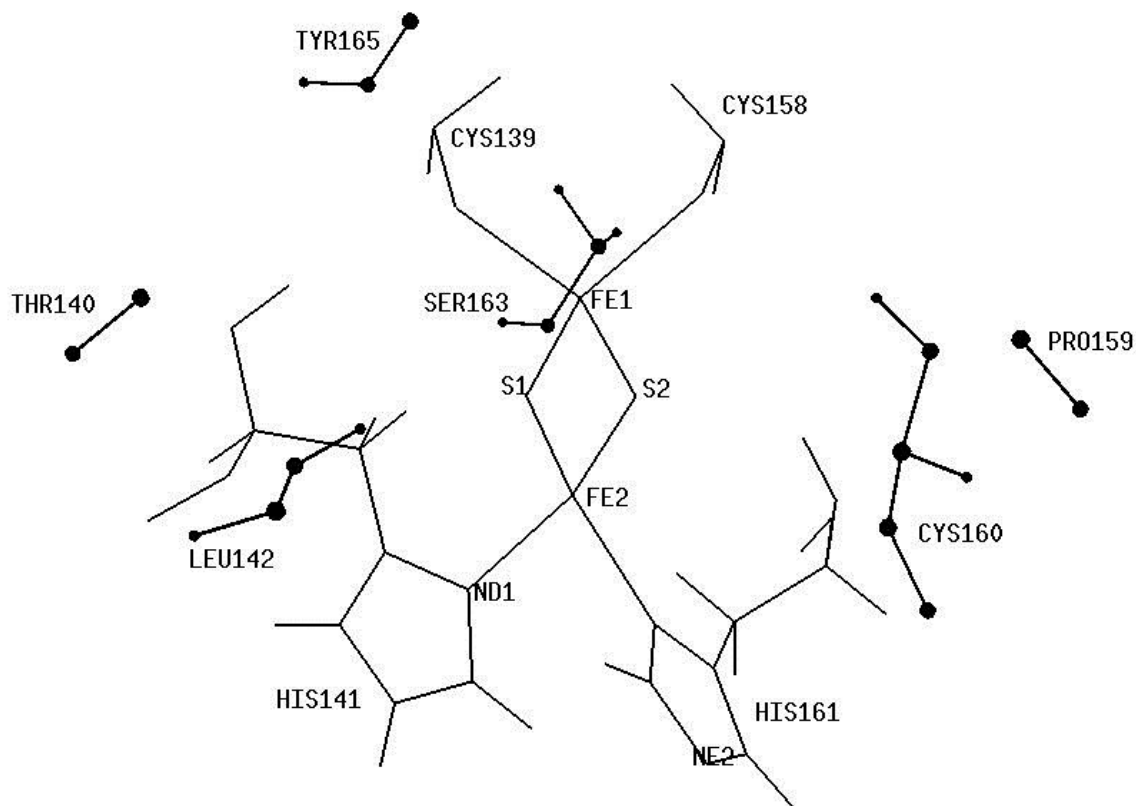
Figure 3.2.1.2: Atoms charges obtained from geometry optimization

Atoms with published charges obtained from geometry optimization using DFT-CE methods for the oxidized ISC, deprotonated His161 and protonated His141 (40). The dashed lines showed hydrogen bond distances between the ISC and neighboring residues, and among these residues themselves.
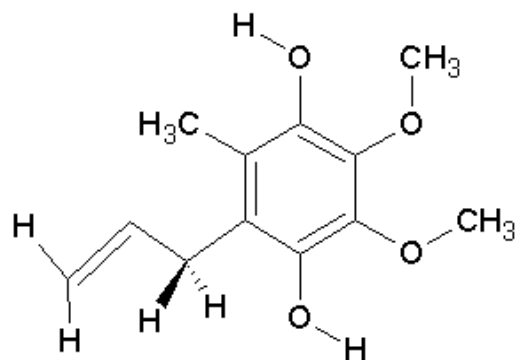
Figure 3.2.1.3: The QH2 model

 The model QH2 with the isoprenyl chain truncated and its methyl group deleted.

The force field parameters for QH2 model were developed and tested by members in the

group. QH2 charges were calculated using B3LYP/6-31G(d) (54),(55) and the CHELPG

scheme (56). QH2 tail was truncated as shown in Figure 3.2.1.3. Force constants were

calculated using the vibrational analysis in Gaussian (42). Non-bonded parameters were

obtained from CHARMM22 (39). For different quinones, including the current QH2

model, electron affinities (41) were calculated using the hybrid HF/DF B3LYP method

(42, 43) and the one electron reduction potentials were calculated in water using FEP/MD

simulations (44-49). The results were within 0.05 eV of experiment, (41, 50-53)

indicating the derived force field parameters for QH2 are reliable. We are aware that

truncation of the QH2 model's isoprenyl tail might affect its binding geometries,

however, this study focuses on testing the hypothesis of QH2 head group forming two

hydrogen bonds, one to the deprotonated His161 and another to the deprotonated Glu271,

as observed in the bound SMA crystal structure. The QH2 model was placed into the

coordinates of its competitive inhibitor stigmatellin (SMA), according to data from

crystal structure 1PP9, in such way that the six membered ring of the QH2 head group

overlaps one of the two six membered rings of SMA and starts as a hydrogen bond donor to deprotonated His161 and Glu271. There are several possible ways to overlay QH2 so that it forms hydrogen bonds to both His161 and Glu271 directly or via a water bridge (see Figure 3.2.1.1). The crystal structure shows that atoms O4 and O5 of the SMA were 2.78Å and 3.14Å away from the NE2 atom of His161, respectively (black dashed lines); atom O8 of SMA is 2.53Å and 2.68Å away from the OE1 of Glu271 and a water molecule, respectively (black dashed lines); and atom O1 of the SMA is 4.75Å away from the water. This water, in turn, can form a hydrogen bond to the OE2 of Glu271 (2.43Å). Figure 3.2.1.1 (left) shows one geometry where we placed the QH2 model (Ubiquinol(1)) so that one of its hydroxyl oxygen atoms overlaps O5 of SMA and the other overlaps O8 of SMA. The hydroxyl hydrogen atoms were rotated so that their distances to the NE2 of His161 and OE1 of Glu271 were minimized (2.51Å and 2.15Å respectively, shown by the red dashed lines in Figure 3.2.1.1). Figure 3.2.1.1 (right) shows the Ubiquinol(2) modeled to superimpose one of its hydroxyl oxygen atoms on SMA atom O4. For this geometry, the distance between the hydroxyl hydrogen and the NE2 atom of His161 is 2.49Å (red dashed line). The ring atom binding the other hydroxyl oxygen atom was placed at the position of SMA atom O1, thus the hydroxyl hydrogen atom of QH2 was 3.14Å from the water molecule that forms a bridge to OE2 of Glu271 (2.43Å). All water molecules from the cytochrome b subunit in the X-ray crystal structure were included in simulations and named differently to distinguish them from the added waters of hydration.

3.2.2 Molecular dynamics simulations

MD simulations are based on Newton's second law of motion stating that the force acting on particle i (F_i) is proportional to the acceleration of particle i (a_i): $F_i = m_i a_i$. The force acting on a system of particles can also be calculated as the negative gradient of the potential energy $F_i = -\nabla_i V$ and thus Newton's equation of motion can be used to relate the derivatives of the potential energy to changes in position as a function of time. Integration of the equations of motion yields a trajectory that describes the positions and velocities (as well as the accelerations) of the particles as they vary with time. From these trajectories, the average values of physical properties can be determined.

The system was solvated with TIP3P water (57) to a distance of 10Å from the protein in each direction. Sodium chloride was added to neutralize and bring the system to the physiological ionic strength using plugins from VMD (7). A one femtosecond time step was used in isothermal, isobaric (constant NPT) simulations, with temperature maintained at 300K using Langevin dynamics with a damping coefficient of 5.0 ps^{-1} and pressure was maintained at 1atm using Langevin piston. The cutoff for electrostatic and van der Waals interactions was 12Å with a switching function on and a switching cutoff of 10Å. Periodic boundary conditions were applied with the Particle Mesh Ewald (PME) (58) grid spacing of 1.0Å for a full system periodic electrostatic potential. One hundred thousand NAMD standard energy minimization steps were performed followed by 2 ns of dynamics where all atoms of the UQ model and the His201 and Asp228 residues were fixed and a restraint of 10kcal/mol•Å^2 was placed on all C-alpha atoms. The restraints were removed slowly in increments of 0.5 kcal/mol•Å^2 for every 1ps to allow the protein's side chains to relax around the hydrogen bonds between the amino acid side

chains and the UQ substrate. After complete removal of the C-alpha's restraints, the constraints on His201, Asp228 and UQ were then removed and the system was allowed to equilibrate for another 2 ns. After equilibration, the RMSD value of the protein backbone relative to the crystal structure fluctuated around 2.2Å. Routine checks for the potential energy over time and the RMSD of protein backbone over time show convergence of the system. A total of 13 ns of dynamics simulation data after equilibration was used for analysis.

3.3. Results and discussion

3.3.1. Hydrogen bond between QH2 model and deprotonated His161 of the ISP is not maintained

Within less than a nanosecond after the removal of all biasing potentials, the hydrogen bond between the deprotonated His161 and QH2 broke, while a hydrogen bonding network including Glu271 was maintained. Trajectories showed that the water molecules bridging the QH2 hydroxyl hydrogen atom and Glu271 remain in place for approximately 1.2 ns before being replaced by another mobile water molecule. These mobile bridging water molecules seem to pull QH2 out of hydrogen bonding range of the deprotonated His161 as they move in and out of the hydrogen bond distance with QH2. The hydrophobic side chains of residues Val145, Leu149 and Leu281 also prevent the charged nitrogen atom of His161 from re-approaching QH2. Figure 3.3.1 shows distributions of distances between QH2's hydroxyl oxygen atoms and the epsilon nitrogen of His161 or the carboxyl oxygen atoms of Glu271, over the entire 13 ns dynamics trajectory. The figure shows approximately normal distributions with an average distance between the NE2 atom of His161 and the hydroxyl oxygen atom of the

QH2 of approximately 6.5Å and 5.3Å for the Ubiquinol(1) starting geometry and Ubiquinol(2) geometry, respectively.

Based on X-ray crystallographic studies with the bound inhibitor SMA, it has been proposed and widely accepted that the hydrogen bond between the epsilon nitrogen NE2 of deprotonated His161 and the head group hydroxyl oxygen of ubiquinol and another hydrogen bond to the carboxylic oxygen of Glu271 directly or via a water molecule stabilize the substrate at the Qo site (2, 21-23, 34, 59). Consequently this binding geometry would allow for deprotonated His161 to serve as the first proton acceptor in the QH2 oxidation (22-24). In our simulations with His161 deprotonated, the initial hydrogen bond between this deprotonated nitrogen and the hydroxyl hydrogen atom of QH2 was not maintained. Thus, it appears unlikely that deprotonated His161 serves as the initial proton acceptor from QH2.
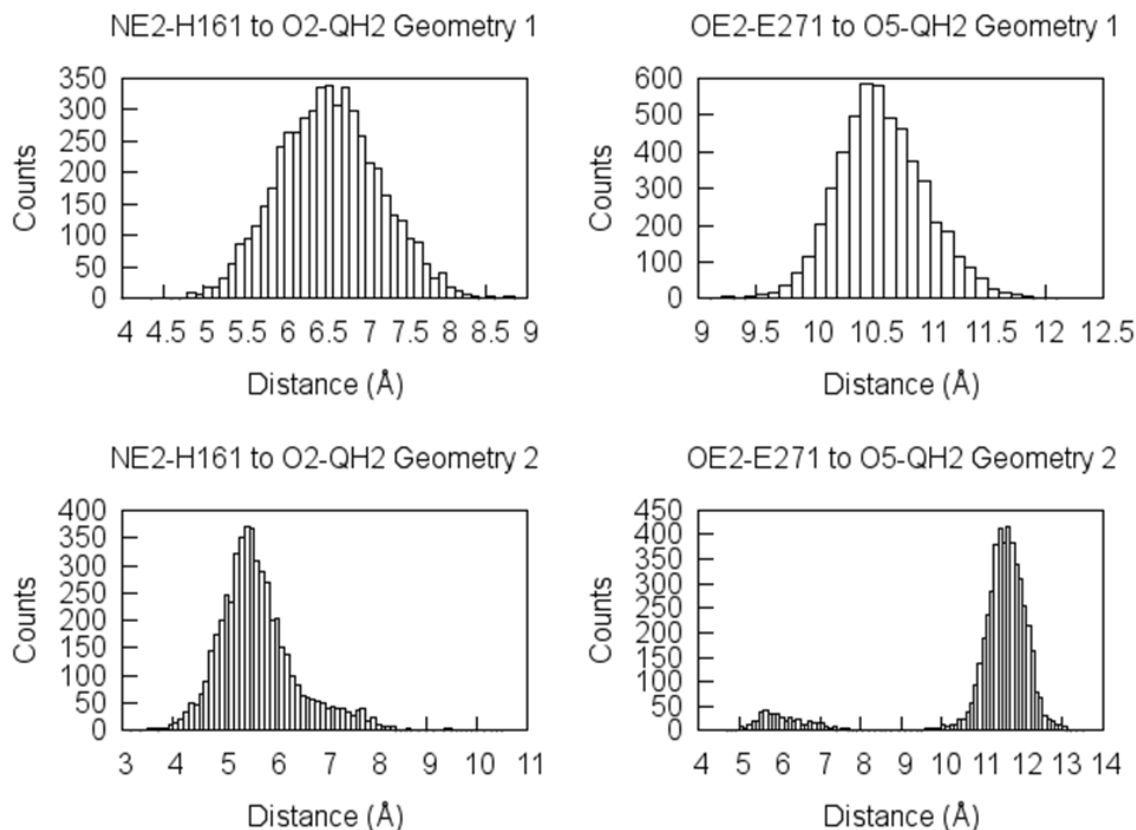
Figure 3.3.1 Distributions of the distances between the epsilon nitrogen atom (NE2) of

His161 and the hydroxyl oxygen atom (O2) of the QH2

Distributions of the distances between the epsilon nitrogen atom (NE2) of His161 and the

hydroxyl oxygen atom (O2) for the Ubiquinol(2) starting geometry over the entire 13 ns

simulation (100 bins). The average distance is maintained near 6.5Å and 5.3Å for the

QH2 starting in geometry 1 and in geometry 2, respectively. Distance distributions

between atom OE2 of Glu271 and the hydroxyl oxygen atom O5 of QH2 over the 13ns

simulation time starting with geometry 1 show a nearly normal distribution with an

average value of 10.5Å; the same distance starting from geometry 2 shows two

approximately normal distributions, one centered at 5.5Å and the other centered at 11.5Å

3.3.2. Deprotonated Glu271 side chain rotates out of the binding pocket

Our results also show that the initial hydrogen bond from the QH2 model to the

deprotonated Glu271 via a water molecule is maintained for a much longer time than a

direct hydrogen bond to the carboxylate oxygen of Glu 271 (or to the deprotonated

His161). Thus, our results support a proposal by Covian et al.(25) and Cape et al.(8) that

the hydrogen bond between deprotonated His161 and QH2 has no role in substrate

stabilization. Instead, the first proton transfer from QH2 may be linked directly to the

protonation state of Glu271 and not His161 (25).

Nonetheless, the hydrogen bond between the Glu271 carboxylate oxygen and QH2 broke

during equilibration for the ubiquinol(1) starting geometry and was maintained for more

than 1ns before breaking for the ubiquinol(2) starting geometry. Note that from geometry

1 the QH2 hydroxyl hydrogen was within the hydrogen bond distance to the carboxylate

oxygen of Glu271, whereas from geometry 2, it was within hydrogen bond distance to a

water molecule that was within hydrogen bond distance to the carboxylate oxygen of

Glu271. A plot of the distance between atom OE2 of Glu271 and the hydroxyl oxygen

atom O5 of QH2 over the 13 ns simulated time of geometry 1 showed an approximately

normal distribution with an average value of 10.5Å; and that of geometry 2 also showed

an almost normal distribution of two populations, one centered at 5.5Å and the other at

11.5Å (Figure 3.3.1). The latter distance was observed after the carboxylate group had

rotated away from QH2. During the entire equilibration (2 ns after all constraints

removed) and the first 1.2 ns of production dynamics, the OE2 atom maintained a distance less than 5.5Å to the hydroxyl oxygen atom O5 and thus forms hydrogen bond to QH2 via a bridging crystallographic water molecule, W8314 (Figure 3.3.2.1). Figure 3.3.2.1 shows distances from the atom OE2 of Glu271 to the oxygen on water molecule W8314 with an average value of 2.8Å and the distances from atom OE1 of Glu271 to W8314 and W5329 with average distances 3.6Å and 2.6Å, respectively (over 1.2ns). Although both water molecules remain within hydrogen bonding distance of the carboxylate oxygen atoms of Glu271, atom OE2 maintains a closer distance to water W8314 and atom is OE1 closer to W5329. The average distance from the oxygen of W8314 to the hydroxyl oxygen O5 of the QH2 is 3.9Å, within a long hydrogen bonding distance. In summary, our results show that deprotonated Glu271 and QH2 have interactions with hydrogen bond character, mediated by the bridging water molecule W8314. This distance is maintained for more than 1.1 ns, before the OE1 rotates 75° degrees around the bond, apparently dragging with it the water W5329. Glu271 thus moves W5329 closer to QH2 and forms the water-bridged hydrogen bond with the hydroxyl oxygen O5 of QH2 (Figure 3.3.2.1). The atom OE1 now acts as the new hydrogen bond donor to water W5329 and this water, in turn, hydrogen bonds to the O5 of QH2. This hydrogen bond persists for approximately 1ps before OE1 rotates again (by approximately 32°) to move the W5329 away from QH2 by breaking the hydrogen bond (Figure 3.3.2.1 bottom). It is important to point out that throughout the simulations other mobile water molecules near the Glu271 also formed hydrogen bond with Glu271, as well as with other water molecules (Figure 3.3.2.2). The hydrogen bonding pattern allows

the water molecules to remain mobile, while at the same time retaining connectivity within a hydrogen-bonded water network.

From these results, we speculate that the roles of Glu271 include: (1) Glu271 remains present near the Qo binding pocket. (2) Glu271 and its charged side chain play a role in orienting and regulating the water molecules near the Qo site; and (3) water molecules near the Qo site most likely play the roles of proton acceptors and proton transporters that mediate the proton transfer path out of the Qo site to the aqueous phase. Although it is very likely that Glu271 is deprotonated under physiological conditions, we performed a pKa calculation for the Glu271 side chain in the presence of QH2, using constant pH molecular dynamics simulations (results shown in chapter 2). These simulations confirm that Glu271 should indeed be deprotonated at pH 7. Meanwhile, our MD simulations imply that this charged side chain ensures that there are always water molecules near the substantially hydrophobic Qo pocket. Our results thus support the proposal by Osyczka et al. (32, 33) of "soft proton management" of putative proton transfer to Glu271by mobile water molecules near the Qo site.
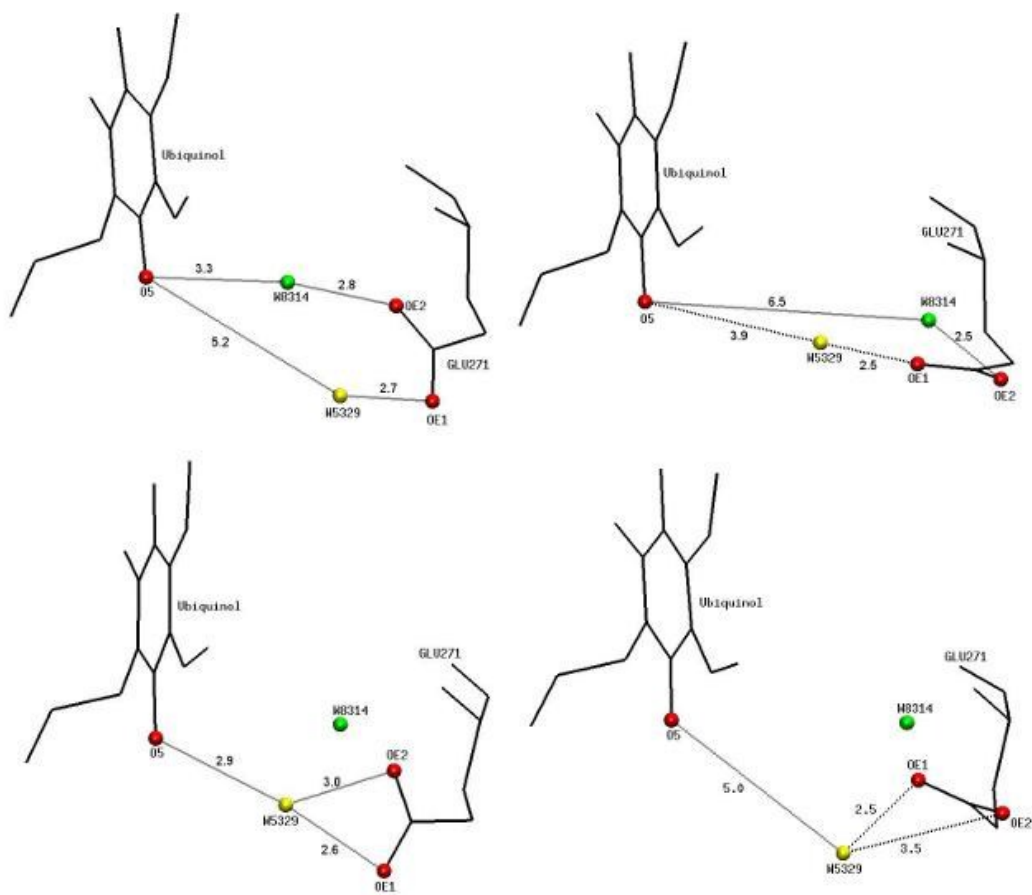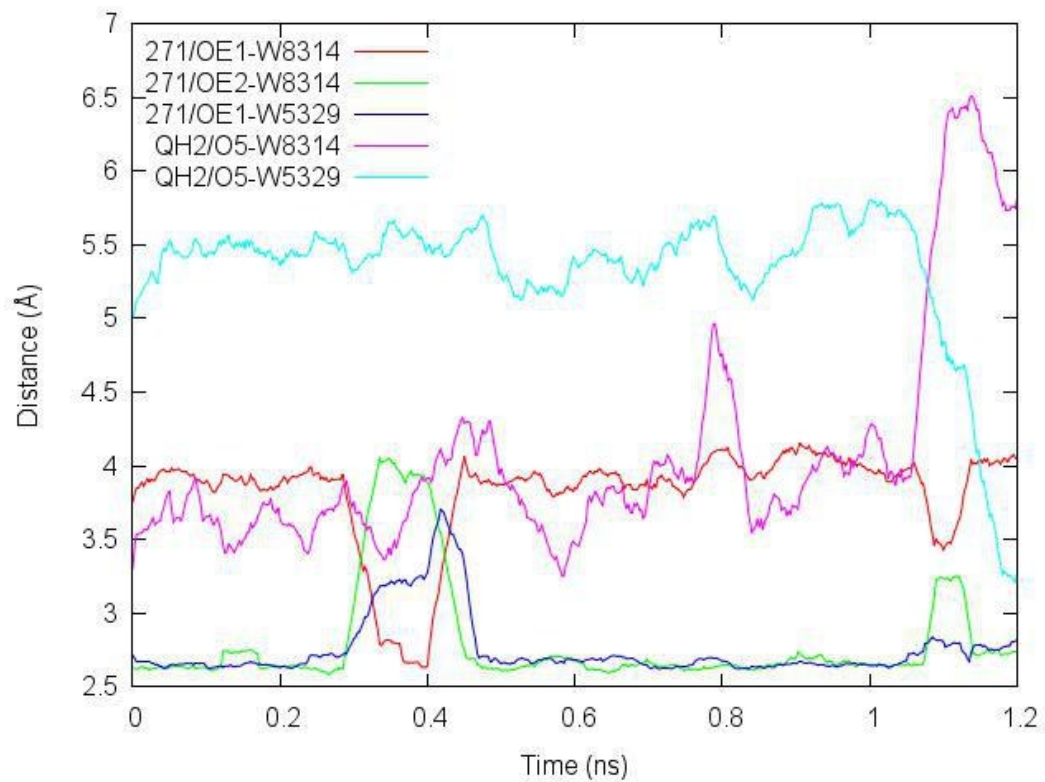
Figure 3.3.2.1 Glu271 oxygen atoms, QH2 hydroxyl oxygen atom, and crystallographic water (W5329 and W8314) hydrogen bonding network

Glu271 oxygen atoms remain in a hydrogen bonding network with the QH2 hydroxyl oxygen atom, water molecule W5329 (light blue), and W8314 (pink) for over 1.2ns. At ~0.3ns, the carboxylic group of Glu271 rotates and OE1 moves closer to QH2, forming a hydrogen bond to W8314 and thus breaking the hydrogen bond between this water molecule and OE2. The hydrogen bond between OE1 and W8314 persists for about 0.1ns before another rotation, when OE2 flips back. The bottom figure shows at ~1.1ns, OE1 rotates 75° degrees around the CG-CD bond, dragging with it the water W5329, thus moving W5329 closer to QH2 and forming a hydrogen bond with the hydroxyl oxygen O5 of QH2. Consequently, the hydrogen bond between QH2 and W8314 breaks. Shortly after the hydrogen bond between water molecule W5329 and oxygen atom OE1 forms a bridge between QH2 and Glu271, OE1 rotates again and pulls W5329 away, breaking its hydrogen bond to QH2.
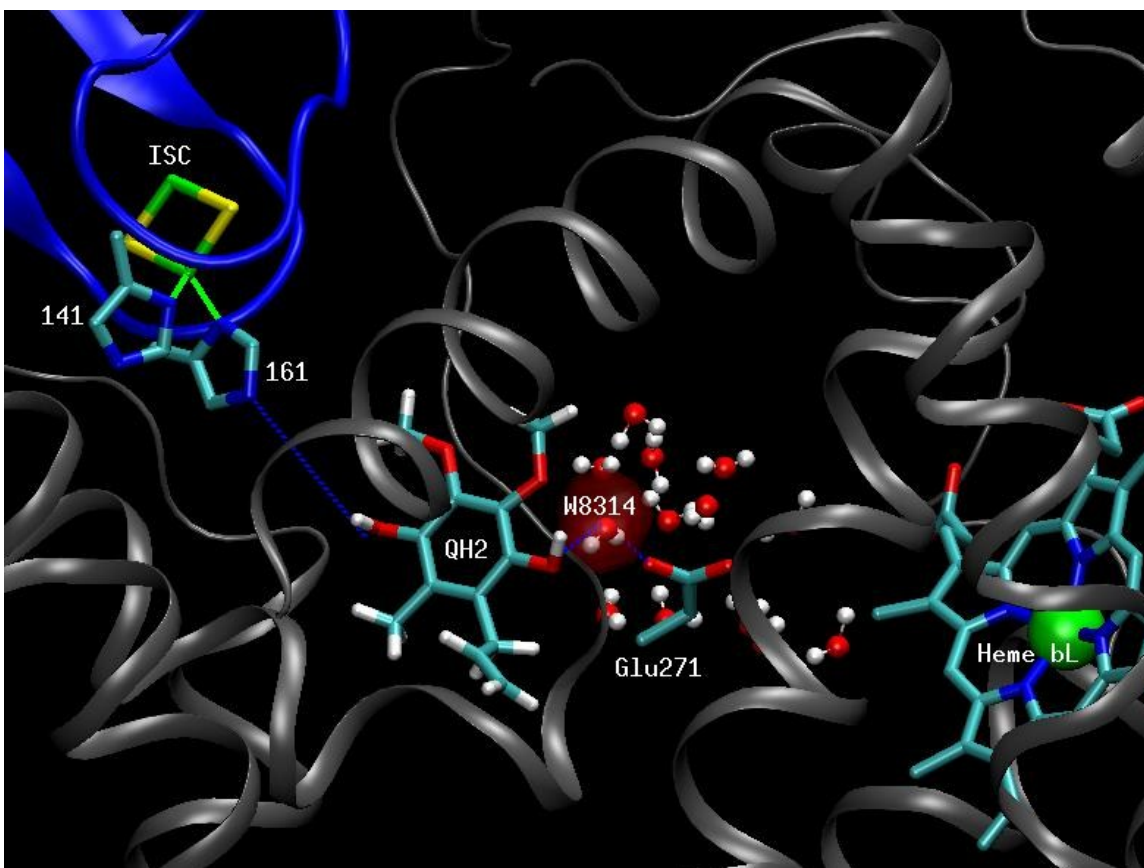
Figure 3.3.2.2: Water molecules clustered around the negatively charged side chain of Glu271

All the water molecules are mobile and within hydrogen bonding distance of at least one other water. Water molecule W8314 is highlighted with a red sphere, because it remains within hydrogen bonding distance from both QH2 and Glu271 for over 1.1ns before being displaced by another water molecule and eventually breaking away from QH2, allowing the Glu271 carboxylate group to rotate toward heme bL (cyan licorice presentation). The distance between the NE2 atom of His161 and the hydroxyl oxygen of QH2 (in blue dashed line) is greater than typical hydrogen bond distance cutoffs (>6.5Å and >5.3Å from geometry 1 and geometry 2, respectively), with no intervening water

molecules. Cytochrome b is showed in gray ribbons and the ISP is showed in blue cartoon representation.

3.3.3. Hydrophobic, aliphatic, and aromatic residues line the QH2 binding pocket

The cytochrome b of the cytochrome bc1 complex consists of eight transmembrane helices labeled A to H and four loops connecting them: AB, CD, DE and EF. The CD loop consists of two short helices cd1 and cd2. The AB and EF loops each contain one short helix and the DE loop has no secondary structure (4). These helices form two helical bundles spanning the membrane. The first helical bundle has five helices (A-E) and houses the two b-type hemes. The second bundle has three helices F-H. Our simulations locate the Qo binding pocket at the interface between the ISP and the cyt b and near the interior of the second helical bundle. The Qo site forms from the following helix fragments: half of the C terminal end of helix C, helix cd1, helix EF, the middle section of helix F and two coils. One coil is where Pro270 and Glu271 are located, at the N terminus of the EF helix and toward the protein inner space close to heme bL. The other coil connects helix cd1 and cd2 and faces toward the surface of the protein (figure 3.3.3.1). The QH2 binding pocket is located within 4Å of the initial position of QH2 and is lined primarily by aliphatic, hydrophobic, and aromatic residues capable of non-polar interactions with QH2.This Qo pocket consists of hydrophobic residues L121, M124, V132, V145, I146, L149, I153, I268, P270, L281 and L194; aromatic residues F128, Y131, F274 and Y278 and small aliphatic residues G142 and A277. These residues participate in helical secondary structure displaying extensive hydrogen bonds along their main chains within helices (as expected), thus surrounding QH2 on four sides, leaving

two "exposed" ends. These two ends are located near the two coils (Figure 3.3.3.2) and contain large voids that allow access to water molecules, suggesting that water molecules might play a role in proton transfer paths at the Qo site (60, 61). The results agree with general features observed in published X-ray crystallographic studies (5, 38). Six of the hydrogen bonds observed in our simulations were also seen in the initial X-ray crystal structure (Table 1).

Table 3.1: The hydrogen bonds proposed in initial X-ray crystal structure

Donor	Acceptor	Donor	Acceptor
TYR278-Side	CYS160-Main (ISP)	ILE146-Main	GLY142-Main
LEU281-Main	ALA277-Main	LEU149-Main	VAL145- Main
PHE128-Main	MET124-Main	TYR278-Main	PHE274-Main

Table 3.2: The hydrogen bonds observed during simulations. The hydrogen bonds highlighted in bold italics were maintained for only 8 ns of the 13 ns simulation.

Donor	Acceptor	Donor	Acceptor	Donor	Acceptor
TYR278-Side	**CYS160-Main**	**LEU281-Main**	**ALA277-Main**	**PHE128-Main**	**MET124-Main**
ILE146-Main	**GLY142-Main**	**LEU149-Main**	**VAL145-Main**	**TYR278-Main**	**PHE274-Main**
LEU150-Main	ILE146-Main	ALA125-Main	LEU121-Main	ILE153-Main	LEU149-Main
GLU271-Main	*GLU271-Side*	PHE274-Main	GLU271-Main	VAL145-Main	TRP141-Main
GLY142-Main	MET138-Main	TYR131-Main	PHE128-Main	*TYR278-Side*	*ILE268-Main*
ALA277-Main	PHE274-Main	*LEU149-Main*	*ILE146-Main*	ILE298-Main	LEU294-Main

Throughout the simulations these six hydrogen bonds in Table 3.1 persist (Figure

3.3.3.2). Moreover, additional hydrogen bonds formed in the simulation when residues

from the connecting loops at the end of helix E moved closer to QH2 and formed helices

surrounding QH2. Table 2 shows the hydrogen bonds observed in the simulations. Those

hydrogen bonds that broke during the last 5ns of the simulation are showed in bold italics

in Table 2. The hydrogen bond between the Glu271 side chain and its main chain atom

broke when the carboxylic oxygen OE1, hydrogen-bonded towater molecule W5329

rotated out of the Qo pocket.
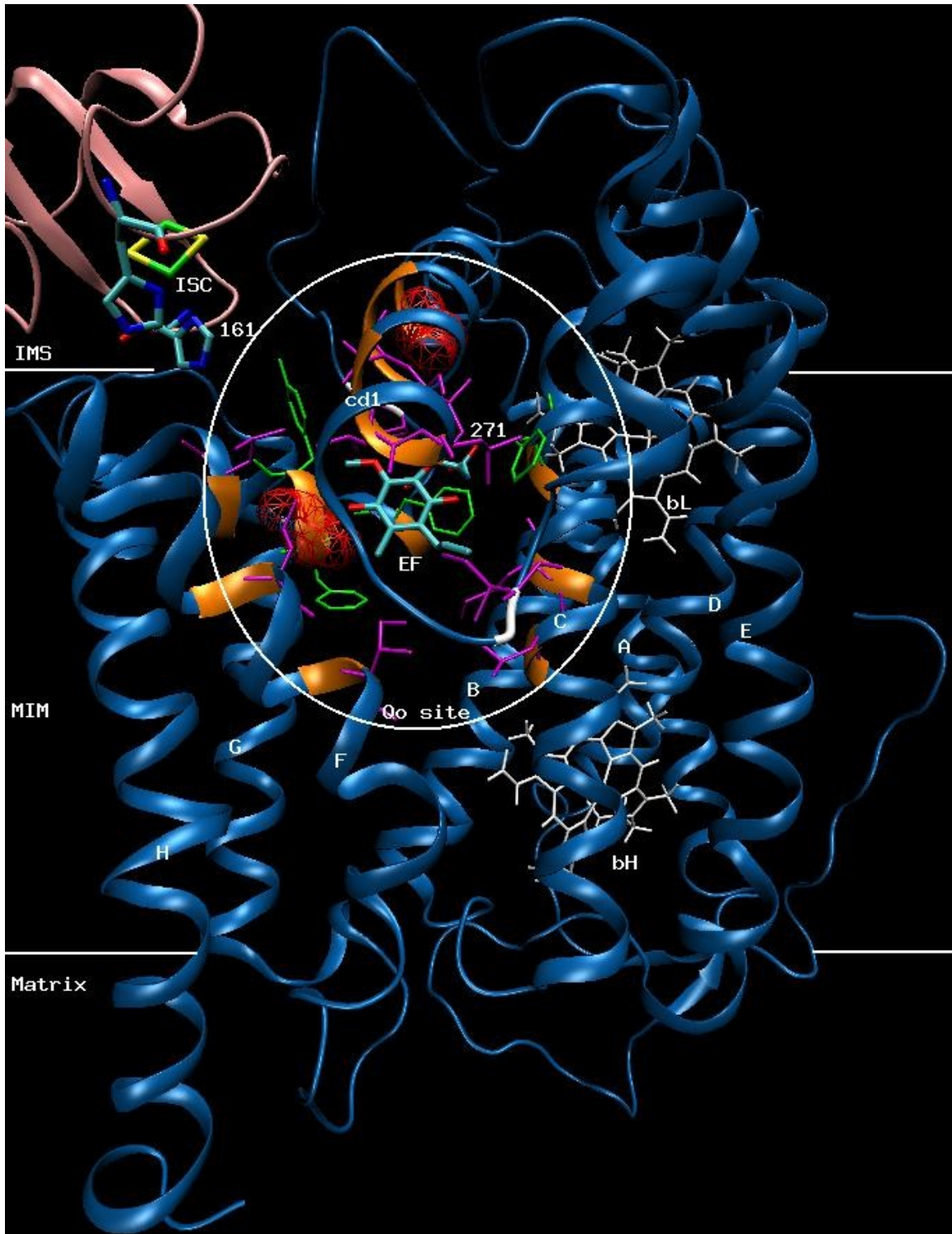
Figure 3.3.3.1: The Qo pocket is imbedded between two helical bundles

Eight transmembrane helices (blue) spanning the mitochondrial inner membrane (MIM) form two helical bundles, A to E and F to H. These two bundles contact each other on the side of the membrane toward the intermembrane space (IMS) and diverge toward the matrix side. The Qo site is within the white circle resting where the two helical bundles make contact. The amino acid backbone atoms defining the Qo site that maintain helical secondary structure throughout the simulations include helices cd1, EF, the C terminal end of helix C and the middle part of helix F(orange). The coil with no secondary structure is shown in white. The ISC, QH2, ligand histidines (His141 and His161) and Glu271 are shown in licorice representation with oxygen atoms red, carbon atoms cyan and hydrogen atoms omitted for clarity. Hydrophobic residues are shown in magenta. Aromatic residues are green and small aliphatic side chain residues are red and shown in a wireframe representation. The b type hemes are shown in tan and the ISP is pink. The Qo site is surrounded on four sides leaving two open ends. One end is oriented toward the matrix and toward the protein surface, where the first coil is located (near the C terminus of helix cd1). The other end is located near the second coil where Glu271 rotates outward, closer to heme bL.
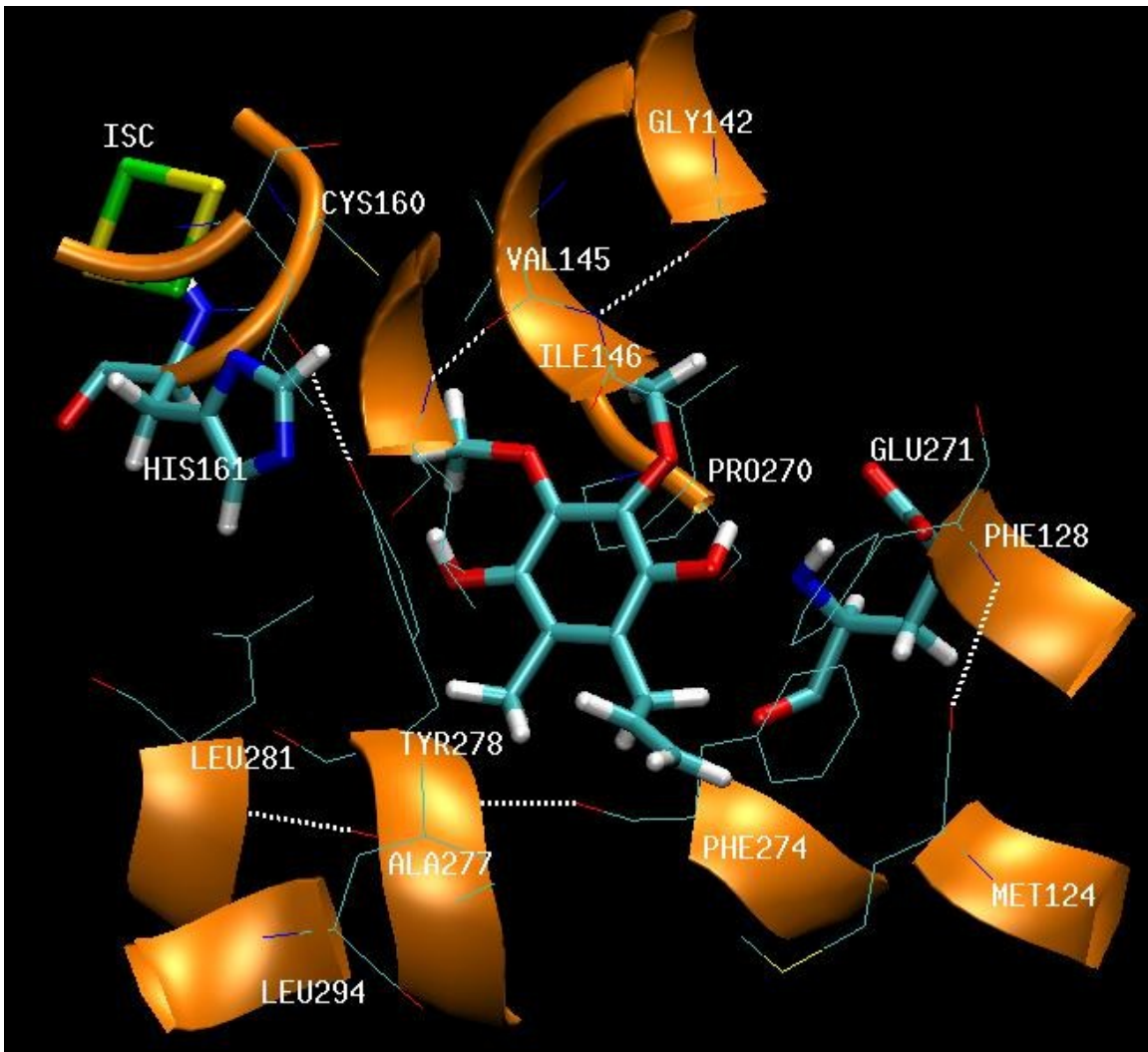
Figure 3.3.3.2: Residues within 4Å of QH2

Residues within 4Å of QH2 are shown in line and orange ribbon representation.

Hydrogen bonds are indicated by white dotted lines; the Iron-Sulfur cluster (ISC), QH2

model, His161 of the Iron-Sulfur protein and Glu271 of cytochrome b are shown in

licorice representation; and the six hydrogen bonds present in the initial X-ray crystal

structure are shown with white dashed lines.
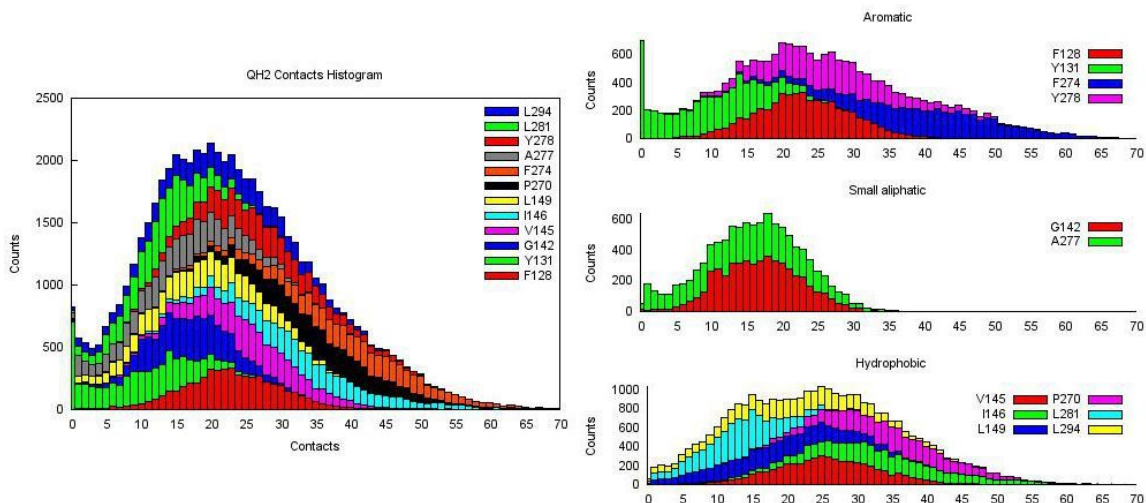
Figure 3.3.3.3: Stacked histogram of number of contacts to QH2 near the Qo site

Stacked histogram of the number of contacts to QH2 from different type of amino acids near the Qo site over the entire 13ns simulation time. Although aromatic and aliphatic residues have larger side chain and are expected to show more contacts than small aliphatic chain residues (Gly142 and Ala277) the small side chain residues also show an average of 17 contacts, meaning that most of their atoms remain within 4Å of the QH2.

Figure 3.3.3.3 shows a stacked histogram plot of the number of contacts between QH2 and hydrophobic, aliphatic, and aromatic side chains near the Qo site over the entire 13ns simulation. The plots show an approximate normal distributions with an average of 22 contacts, with contributions from all residues near the Qo site. We count as a contact any atom found within 4Å of any atom of QH2, at any time step in the simulation. As expected, aromatic and aliphatic residues with larger side chain show more contacts than those of small aliphatic chain residues (Gly, Ala). These same residues were observed to

have heavy atom(s) within 4Å of the inhibitor SMA in the initial X-ray crystal structure
(Table 3). Among those residues within 4 Å of SMA in the initial X-ray structure,
simulations show that all of the same residues, except Ile268 and Met129, make
numerous contacts with QH2 throughout the simulations. At most, only one atom
belonging to each of these two residues, Ile268 and Met129, was seen within 4Å of QH2
throughout 13 ns simulations. We identified two more residues, Leu281 and Leu149, that
also have numerous contacts with QH2, but the X-ray crystal structure failed to reveal
them. We also observed several residues that display multiple contacts to QH2 in a non-
normal distribution of distances. These residues are: Leu121, Met124, Val132, Ile153 and
Ile268.

Table 3.3: Number of contacts to SMA in X-ray crystal structure 1PP9

Cytochrome b	Residue name	Contacts	Residue name	Contacts
	LEU294	1	ILE146	3
	TYR278	1	VAL145	6
	ALA277	1	GLY142	1
	PHE274	4	MET129	1
	PRO270	2	PHE128	4
	ILE268	1		
ISP	CYS160	1	HIS161	1

3.3.4. Orientations of aromatic residues near the Qo binding site

 Residue Phe274 shows the largest number of contacts to QH2 it maintains a close
distance to QH2 and thus it appears to play a role in QH2 binding, perhaps by orienting

the head group. In previously published work,(16) Phe274 mutation was suggested to be responsible for the resistance developed toward the anti-malarial drug atovaquone that targets the Qo site cyt bc1 and its putative role in inhibitor binding was used to propose new anti-malarial, cyt bc1 inhibitors. Our simulations likewise imply that Phe274's aromatic ring plays a role in orienting the QH2 ring, The two rings maintain an average angle between the normals to their ring planes of 150° implying an approximate pi stacking geometry of the two rings (Figure 3.3.4). Together, the residues Phe274, Phe128, Tyr131 and Tyr278 form a pi-stacking network with approximately co-planar geometries with QH2 and with each other (62). Mutations of residue Tyr131 and Tyr278 by Wenz et al. (63). showed that mutation of any individual aromatic residue to another aromatic side chain (e.g. Y131F) gave no change in sensitivity to the inhibitor stigmatellin, whereas mutations to non-aromatic side chains (Y278A, Y278C and Y278S) decreased sensitivity to stigmatellin 5-fold, 4-fold, and completely, respectively. The authors interpreted the results to mean that Tyr278 plays a role to pre-orient the QH2 substrate head group while Tyr131 may not. Although Tyr131 could have some other function in the mechanism of electron and proton transfer at the Qo site, we believe it also plays a role in substrate binding geometries. Mutation of Tyr131 to a non-aromatic residue could test this hypothesis. Moreover, to our knowledge there are no published reports of multiple mutations of these aromatic residues to non-aromatic residues to test the cooperative nature of their stacking at the Qo site. We suggest that disrupting the connectivity of the pi stacking by decreasing the number of aromatic rings would have different effects on substrate binding and multiple points mutations of these aromatic residues to non-aromatic residues can test our results.
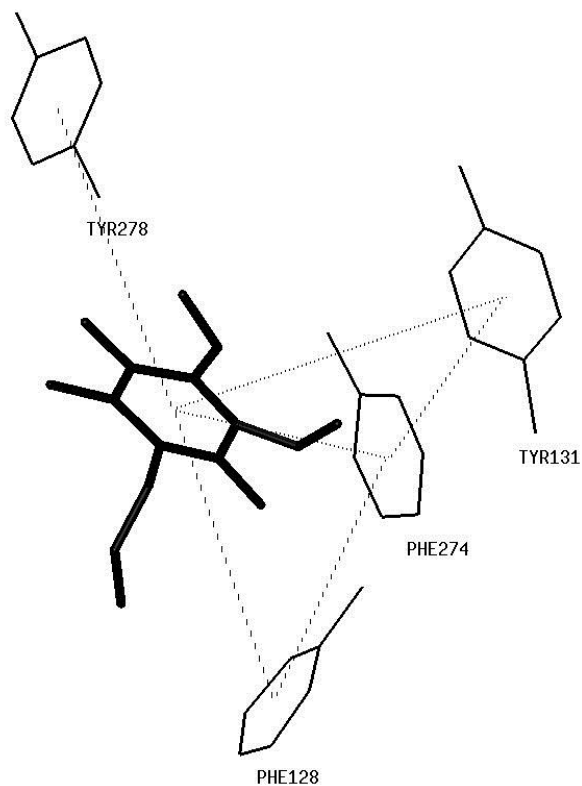
Figure 3.3.4: The orientation of aromatic rings for residues Phe128, Tyr131, Phe274, Tyr278

Their connectivity is shown in black dashed lines and forms a pi network with cooperative π-π orientations that together with the nonpolar interactions of aliphatic residues form the Qo binding pocket and orient the QH2 (bold black line)

3.4. Conclusions

In this work, we show that (1) the hydrogen bond between a ubiquinol model and the deprotonated His161 side chain of the oxidized ISP was not maintained during MD simulation; (2) the direct hydrogen bond between a ubiquinol model and deprotonated Glu271 carboxylate oxygen was also not maintained; (3) *water-mediated hydrogen bonding* between a ubiquinol model and the deprotonated Glu271 side chain remained for

part of the simulation, but broke when the Glu271 side chain rotated by more than100°, out of the Qo pocket and toward a position near heme bL (as suggested by Crofts et el. (22, 23, 27)). Our results agree with kinetic studies by Covian et al. (25) and with EPR spectroscopic measurements by Cape et al. (8) implying that His161 does not stabilize binding of the QH2 substrate. Our simulations also agree with Crofts's proposal that the Glu271 side chain indeed rotates out of the Qo binding pocket (23). The published proposal that Glu271 is very likely to participate in proton transfer from QH2 to the aqueous phase via a water molecule (or a water chain), is also supported by the mobility of Glu271 observed in our simulations. However, our MD trajectories show that the hydrogen atom of the QH2 hydroxyl group remained within hydrogen bonding distance of a free water molecule for a longer time than when the water also hydrogen bonded directly with the carboxylate oxygen atom of Glu271. We also observe that there were always water molecule(s) near Glu271 that could hydrogen bond(s) to the deprotonated Glu271. Therefore, we propose that the proton from QH2 could be transferred first to a water molecule. It appears very likely that Glu271 plays little to no role in substrate binding and its presence is simply to stabilize water molecules near the primarily hydrophobic protein interior between the heme bL and the ISP interface. This could explain why mutation of E271Q reportedly does not change the activation energy of QH2 oxidation, (26) simply because the mutation did not eliminate the true proton acceptor: water. Other mutations of Glu271 showed effects on the protein activities (22, 35), so Glu271 clearly plays an indirect role in proton transfer but it does not necessarily play a role in substrate binding.

Acknowledgments

References

1. Mitchell P. Possible molecular mechanisms of the protonmotive function of cytochrome systems. J Theor Biol. 1976;62(2):327-67.

2. Mulkidjanian AY. Proton translocation by the cytochrome bc1 complexes of phototrophic bacteria: Introducing the activated Q-cycle. Photochem Photobiol Sci. 2007;6(1):19-34.

3. Maloney PC, Kashket ER, Wilson TH. Protonmotive force drives ATP synthesis in bacteria. Proc Natl Acad Sci U S A. 1974;71(10):3896-900.

4. Xia D, Yu C, Kim H, Xia J, Kachurin AM, Zhang L, et al. Crystal structure of the cytochrome bc1 complex from bovine heart mitochondria. Science (Washington, D C). 1997;277(5322):60-6.

5. Gao X, Wen X, Esser L, Quinn B, Yu L, Yu C, et al. Structural basis for the quinone reduction in the bc1 complex: A comparative analysis of crystal structures of mitochondrial cytochrome bc1 with bound substrate and inhibitors at the qi site. Biochemistry. 2003;42(30):9067-80.

6. Esser L, Quinn B, Li Y, Zhang M, Elberry M, Yu L, et al. Crystallographic studies of quinol oxidation site inhibitors: A modified classification of inhibitors for the cytochrome bc1 complex. J Mol Biol. 2004;341(1):281-302.

7. Humphrey W, Dalke A, Schulten K. VDM: Visual molecular dynamics. J Mol Graphics. 1996;14(1):33,8, plates, 27-28.

8. Cape JL, Bowman MK, Kramer DM. A semiquinone intermediate generated at the qo site of the cytochrome bc1 complex: Importance for the q-cycle and superoxide production. Proc Natl Acad Sci U S A. 2007;104(19):7887-92.

9. Droese S, Brandt U. The mechanism of mitochondrial superoxide production by the cytochrome bc1 complex. J Biol Chem. 2008;283(31):21649-54.

10. Muller F, Crofts AR, Kramer DM. Multiple Q-cycle bypass reactions at the qo site of the cytochrome bc1 complex. Biochemistry. 2002;41(25):7866-74.

11. Zhang L, Yu L, Yu C. Generation of superoxide anion by succinate-cytochrome c reductase from bovine heart mitochondria. J Biol Chem. 1998;273(51):33972-6.

12. Yin Y, Yang S, Yu L, Yu C. Reaction mechanism of superoxide generation during ubiquinol oxidation by the cytochrome bc1 complex. J Biol Chem. 2010;285(22):17038-45.

13. Fernandez-Ortuno D, Tores JA, de Vicente A, Perez-Garcia A. Mechanisms of resistance to QoI fungicides in phytopathogenic fungi. Int Microbiol. 2008;11(1):1-9.

14. Looareesuwan S, Chulay JD, Canfield CJ, Hutchinson DBA. Malarone (atovaquone and proguanil hydrochloride): A review of its clinical development for treatment of malaria. Am J Trop Med Hyg. 1999;60(4):533-41.

15. Farnert A, Lindberg J, Gil P, Swedberg G, Berqvist Y, Thapar MM, et al. Evidence of plasmodium falciparum malaria resistant to atovaquone and proguanil hydrochloride: Case reports. Bmj. 2003;326(7390):628-9.

16. Kessl JJ, Lange BB, Merbitz-Zahradnik T, Zwicker K, Hill P, Meunier B, et al. Molecular basis for atovaquone binding to the cytochrome bc1 complex. J Biol Chem. 2003;278(33):31312-8.

17. Huang L, Cobessi D, Tung EY, Berry EA. Binding of the respiratory chain inhibitor antimycin to the mitochondrial bc1 complex: A new crystal structure reveals an altered intramolecular hydrogen-bonding pattern. J Mol Biol. 2005;351(3):573-97.

18. Iwata S, Lee JW, Okada K, Lee JK, Iwata M, Rasmussen B, et al. Complete structure of the 11-subunit bovine mitochondrial cytochrome bc1 complex. Science (Washington, D C). 1998;281(5373):64-71.

19. Hunte C, Koepke J, Lange C, Rossmanith T, Michel H. Structure at 2.3 Ã… resolution of the cytochrome bc1 complex from the yeast saccharomyces cerevisiae co-crystallized with an antibody fv fragment. Structure (London). 2000;8(6):669-84.

20. Iwaki M, Yakovlev G, Hirst J, Osyczka A, Dutton PL, Marshall D, et al. Direct observation of redox-linked histidine protonation changes in the iron-sulfur protein of the cytochrome bc1 complex by ATR-FTIR spectroscopy. Biochemistry. 2005;44(11):4230-7.

21. Trumpower BL. A concerted, alternating sites mechanism of ubiquinol oxidation by the dimeric cytochrome bc1 complex. Biochim Biophys Acta, Bioenerg. 2002;1555(1-3):166-73.

22. Crofts AR, Hong S, Ugulava N, Barquera B, Gennis R, Guergova-Kuras M, et al. Pathways for proton release during ubihydroquinone oxidation by the bc1 complex. Proc Natl Acad Sci U S A. 1999;96(18):10021-6.

23. Crofts AR, Barquera B, Gennis RB, Kuras R, Guergova-Kuras M, Berry EA. Mechanism of ubiquinol oxidation by the bc1 complex: Different domains of the quinol binding pocket and their role in the mechanism and binding of inhibitors. Biochemistry. 1999;38(48):15807-26.

24. Crofts AR. The cytochrome bc1 complex: Function in the context of structure. Annu Rev Physiol. 2004;66:689,733, 4 plates.

25. Covian R, Moreno-Sanchez R. Role of protonatable groups of bovine heart bc1 complex in ubiquinol binding and oxidation. Eur J Biochem. 2001;268(22):5783-90.

26. Covian R, Trumpower BL. The rate-limiting step in the cytochrome bc1 complex (ubiquinol-cytochrome c oxidoreductase) is not changed by inhibition of cytochrome b-dependent deprotonation: Implications for the mechanism of ubiquinol oxidation at center P of the bc1 complex. J Biol Chem. 2009;284(21):14359-67.

27. Crofts AR, Lhee S, Crofts SB, Cheng J, Rose S. Proton pumping in the bc1 complex: A new gating mechanism that prevents short circuits. Biochim Biophys Acta, Bioenerg. 2006;1757(8):1019-34.

28. Snyder C, Trumpower BL. Mechanism of ubiquinol oxidation by the cytochrome bc1 complex: Pre-steady-state kinetics of cytochrome bc1 complexes containing site-directed

mutants of the rieske iron-sulfur protein. Biochim Biophys Acta, Bioenerg. 1998;1365(1-2):125-34.

29. Snyder CH, Gutierrez-Cirlos EB, Trumpower BL. Evidence for a concerted mechanism of ubiquinol oxidation by the cytochrome bc1 complex. J Biol Chem. 2000;275(18):13535-41.

30. Covian R, Pardo JP, Moreno-Sanchez R. Tight binding of inhibitors to bovine bc1 complex is independent of the rieske protein redox state. consequences for semiquinone stabilization in the quinol oxidation site. J Biol Chem. 2002;277(50):48449-55.

31. Shimizu M, Katsuda N, Katsurada T, Mitani M, Yoshioka Y. Mechanism on two-electron oxidation of ubiquinol at the qp site in cytochrome bc1 complex: B3LYP study with broken symmetry. J Phys Chem B. 2008;112(47):15116-26.

32. Osyczka A, Moser CC, Daldal F, Dutton PL. Reversible redox energy coupling in electron transfer chains. Nature. 2004 02/12;427(6975):607-12.

33. Osyczka A, Moser CC, Dutton PL. Fixing the Q cycle. Trends Biochem Sci. 2005 4;30(4):176-82.

34. Trumpower BL. The protonmotive Q cycle. energy transduction by coupling of proton translocation to electron transfer by the cytochrome bc1 complex. J Biol Chem. 1990;265(20):11409-12.

35. Zito F, Finazzi G, Joliot P, Wollman F. Glu78, from the conserved PEWY sequence of subunit IV, has a key function in cytochrome b6f turnover. Biochemistry. 1998;37(29):10395-403.

36. Kim H, Xia D, Yu CA, Xia JZ, Kachurin AM, Zhang L, et al. Inhibitor binding changes domain mobility in the iron-sulfur protein of the mitochondrial bc1 complex from bovine heart. Proc Natl Acad Sci U S A. 1998;95(14):8026-33.

37. Brugna M, Rodgers S, Schricker A, Montoya G, Kazmeier M, Nitschke W, et al. A spectroscopic method for observing the domain movement of the rieske iron-sulfur protein. Proc Natl Acad Sci U S A. 2000;97(5):2069-74.

38. Huang L, Cobessi D, Tung EY, Berry EA. Binding of the respiratory chain inhibitor antimycin to the mitochondrial bc1 complex: A new crystal structure reveals an altered intramolecular hydrogen-bonding pattern. J Mol Biol. 2005;351(3):573-97.

39. Brooks BR, Bruccoleri RE, Olafson BD, States DJ, Swaminathan S, Karplus M. CHARMM: A program for macromolecular energy, minimization, and dynamics calculations. J Comput Chem. 1983;4(2):187-217.

40. Ullmann GM, Noodleman L, Case DA. Density functional calculation of pKa values and redox potentials in the bovine rieske iron-sulfur protein. JBIC, J Biol Inorg Chem. 2002;7(6):632-9.

41. Boesch SE, Grafton AK, Wheeler RA. Electron affinities of substituted p-benzoquinones from hybrid hartree-fock/density-functional calculations. J Phys Chem. 1996;100(24):10083-7.

42. Frisch MJ, Trucks GW, Schlegel HB, Scuseria GE, Robb MA, Cheeseman JR, et al. Gaussian 09, revision A1**
**. 2009.

43. Stephens PJ, Devlin FJ, Chabalowski CF, Frisch MJ. Ab initio calculation of vibrational absorption and circular dichroism spectra using density functional force fields. J Phys Chem. 1994;98(45):11623-7.

44. Straatsma TP, McCammon JA. Computational alchemy. Annu Rev Phys Chem. 1992;43:407-35.

45. Beveridge DL, DiCapua FM. Free energy via molecular simulation: Applications to chemical and biomolecular systems. Annu Rev Biophys Biophys Chem. 1989;18:431-92.

46. Van Gunsteren WF, Berendsen HJC. Molecular dynamics computer simulation. method, application and perspectives in chemistry. Angew Chem. 1990;102(9):1020-55.

47. Kollman P. Free energy calculations: Applications to chemical and biochemical phenomena. Chem Rev (Washington, D C). 1993;93(7):2395-417.

48. Jorgensen WL. Free energy calculations: A breakthrough for modeling organic chemistry in solution. Acc Chem Res. 1989;22(5):184-9.

49. Reynolds CA, King PM, Richards WG. Free energy calculations in molecular biophysics. Mol Phys. 1992;76(2):251-75.

50. Wheeler RA. A method for computing one-electron reduction potentials and its application to p-benzoquinone in water at 300 K. J Am Chem Soc. 1994;116(24):11048-51.

51. Raymond KS, Grafton AK, Wheeler RA. Calculated one-electron reduction potentials and solvation structures for selected p-benzoquinones in water. J Phys Chem B. 1997;101(4):623-31.

52. Wise KE, Grafton AK, Wheeler RA. Trimethyl-p-benzoquinone provides excellent structural, spectroscopic, and thermochemical models for plastoquinone-1 and its radical anion. J Phys Chem A. 1997;101(6):1160-5.

53. Grafton AK, Wheeler RA. Amino acid protonation states determine binding sites of the secondary ubiquinone and its anion in the rhodobacter sphaeroides photosynthetic reaction center. J Phys Chem B. 1999;103(25):5380-7.

54. Becke AD. Density-functional thermochemistry. III. the role of exact exchange. J Chem Phys. 1993;98(7):5648-52.

55. Stephens PJ, Devlin FJ, Chabalowski CF, Frisch MJ. Ab initio calculation of vibrational absorption and circular dichroism spectra using density functional force fields. J Phys Chem. 1994;98(45):11623-7.

56. Breneman CM, Wiberg KB. Determining atom-centered monopoles from molecular electrostatic potentials. the need for high sampling density in formamide conformational analysis. J Comput Chem. 1990;11(3):361-73.

57. Jorgensen WL, Chandrasekhar J, Madura JD, Impey RW, Klein ML. Comparison of simple potential functions for simulating liquid water. J Chem Phys. 1983;79(2):926-35.

58. Essmann U, Perera L, Berkowitz ML, Darden T, Lee H, Pedersen LG. A smooth particle mesh ewald method. J Chem Phys. 1995;103(19):8577-93.

59. Crofts AR, Holland JT, Victoria D, Kolling DRJ, Dikanov SA, Gilbreth R, et al. The Q-cycle reviewed: How well does a monomeric mechanism of the bc1 complex account for the function of a dimeric complex?. Biochim Biophys Acta, Bioenerg. 2008;1777(7-8):1001-19.

60. Palsdottir H, Lojero CG, Trumpower BL, Hunte C. Structure of the yeast cytochrome bc1 complex with a hydroxyquinone anion qo site inhibitor bound. J Biol Chem. 2003;278(33):31303-11.

61. Hunte C, Palsdottir H, Trumpower BL. Protonmotive pathways and mechanisms in the cytochrome bc1 complex. FEBS Lett. 2003;545(1):39-46.

62. Chourasia M, Sastry GM, Sastry GN. Aromatic-aromatic interactions database, A2ID: An analysis of aromatic Ï€-networks in proteins. Int J Biol Macromol. 2011;48(4):540-52.

63. Wenz T, Covian R, Hellwig P, MacMillan F, Meunier B, Trumpower BL, et al.

Mutational analysis of cytochrome b at the ubiquinol oxidation site of yeast complex III.

J Biol Chem. 2007;282(6):3977-88.

CHAPTER 4

DIRECT HYDROGEN BOND FROM HIS201 AND WATER-MEDIATED

HYDROGEN BOND FROM ASP228 ASSIST UBIQUINONE BINDING AT THE Q_i

SITE IN BOVINE CYTOCHROME BC1 COMPLEX

Abstract

The mitochondrial cytochrome bc1 complex and its analogue cytochrome b6f catalyze

electron(s) coupled proton(s) transfer reactions that are essential in almost all organisms.

Many reports regarding the structures and functions of the enzyme's Qi catalytic site

have been presented in the early 2000s. Although a general agreement among workers in

the field regarding the amino acid residues in close contact with ubiquinone at the Qi site

has been established, there is no attempt to address several controversial hydrogen bond

configurations involving mobile water molecules. Such studies can be challenging for

experimental methods. Fortunately, with the rapid development of technologies and

computational methods, such questions can be considered more closely. In this work, we

used molecular dynamics simulations to examine the binding geometries of ubiquinone

(UQ) in order to understand the structural driving factors for reduction of UQ at the Qi

site. Our results show that Asp228 spent 69% and 79% of the simulation time within

hydrogen bonding distance of the ubiquinone via a water molecule, primarily in two

different geometries. His201 spent 68% and 24% of the simulation time directly within

hydrogen bond distance to the ubiquinone, again in the two different geometries. We also

suggest that the face-to-face stacking of UQ with four aromatic residues: Phe18, Trp31,

His201 and Phe20 plays an important role in orienting the substrate in a geometry that

might assist electron and proton transfer at the Qi site. We also identified one orientation of the ubiquinone head group relative to the protein that is more favorable than the other.

4.1. Introduction

4.1.1. Mitochondrial cytochrome bc1 complex operates by a modified Q-cycle

As previously mentioned in the introduction, the mitochondrial cytochrome (cyt) bc1 complex and its homologous cyt b6f complex are essential proteins for the respiratory and photosynthetic electron transport coupled ATP production across all organisms (1). It catalyzes the bifurcated electron transfer from ubiquinol at the Qo site to the high potential cytochrome c and to the low potential cytochrome b, where the electrons reduce ubiquinone to ubiquinol at the Qi site, in two turnovers. The electron transfer is coupled to the translocation of protons across the mitochondrial inner membrane, generating a proton gradient that drives ATP synthesis. This type of proton coupled electron transfer reaction was suggested by Mitchell to operate by a prototypical "Q-cycle" (2).
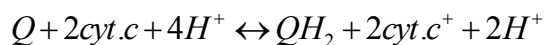
$$Q + 2cyt.c + 4H^+ \leftrightarrow QH_2 + 2cyt.c^+ + 2H^+$$

A modified Q-cycle (Figure 1.2.2) is necessary to describe the bifurcated electron transfer mechanism in which two QH2 molecules are oxidized to generate four electrons at the Qo site and fully reduce a UQ molecule to QH2 at the Qi site.

Although the modified Q-cycle of Figure 1.2.2 is widely accepted by workers in the field as the model that best describes how electrons and protons flow in the cytochrome bc1 complex, many structural features near the ubiquinol reduction site (Qo) and the ubiquinone oxidation site (Qi) remain unclear. These detailed binding geometries and dynamics play an essential role in controlling the chemical mechanism,

113

thermodynamically and kinetically. One profound controversy regarding the mechanism of electron transfer in the cyt bc1 complex is the mechanism of the QH2 oxidation at the Qo site. The fact that there is no known crystal structure with a bound ubiquinol species and an extremely low limit was set on the concentration of semiquinone intermediate(s) near the Qo site (3-6) makes it very difficult to establish a clear and unambiguous mechanism. We discuss the different binding geometries near the Qo site in Chapter 3. Chapter 2 only focuses on the Qi site binding geometries of ubiquinone.

4.1.2. Controversial configurations of the hydrogen bonded ligand, UQ, at the Qi site

The X-ray diffraction structure of the bovine cyt bc1 complex with a natural ubiquinone modeled in was reported for the first time in 2003 by Gao et al. (7). In this structure, the authors suggested a substrate ligand binding geometry involving two water-mediated hydrogen bonds from His201 and Asp228 to the two carbonyl oxygen atoms at positions 1 and 4 on the benzoquinone ring and another hydrogen bond from Ser205 to one of the ubiquinone methoxy oxygens (Figure 4.1.2, left). Two years later, Huang et al. (8) published other structures with bound UQ and various bound inhibitors and suggested that His201 forms a direct hydrogen bond to the UQ with no water involved (Figure 4.1.2, right). The two groups generally agree that the amino acid side chains capable of forming hydrogen bonds to the ubiquinone substrate are His201, Asp228 and Ser205. However, there is disagreement whether His201 contacts UQ via a water-mediated hydrogen bond or a direct hydrogen bond. Moreover, in the cyt bc1 complex from yeast, Hunte et al. (9) suggested that the highly conserved residues His202, Asp229, and Ser206 (yeast numbering) hydrogen bond to UQ. However, they suggested a slightly different

configuration at the Qi site, with a direct hydrogen bond from Asp229 (Asp228 in bovine

cyt bc1) to UQ and a water-mediated hydrogen bond from His202 (His201 in bovine cyt

bc1) to UQ.
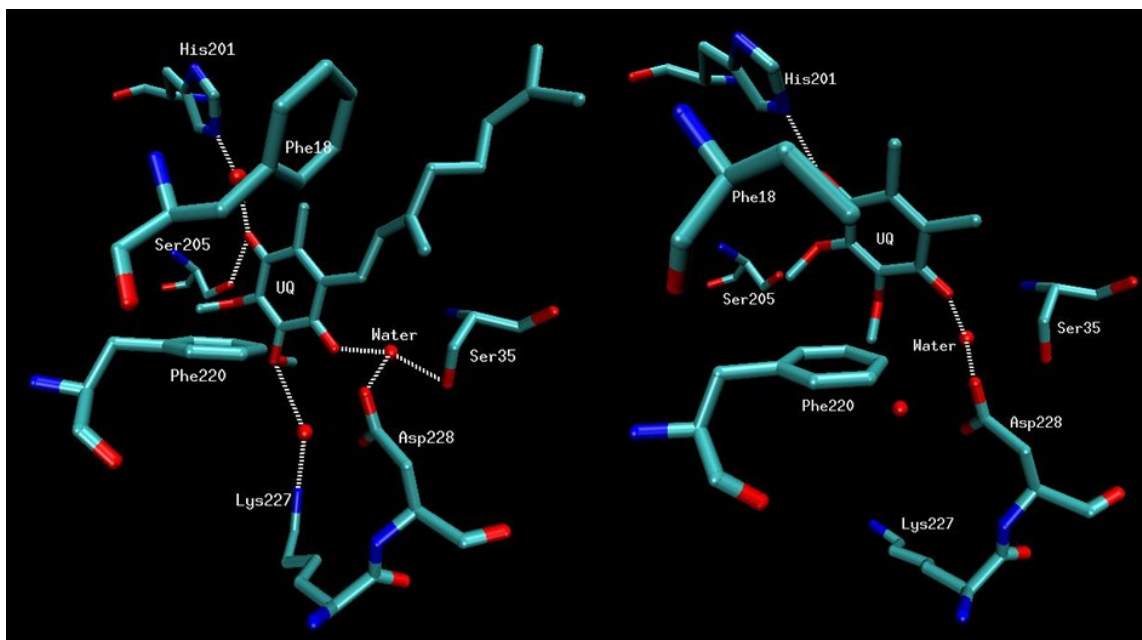
Figure 4.1.2: The Qi binding site defined by two different X-ray crystal structures

Carbon atoms are shown in cyan, oxygen atoms are in red and nitrogen atoms are in blue.

The left figure is from Gao et al.'s structure (1NTZ) with a water-mediated hydrogen

bond at His201.(7) The right figure is from Huang et al.'s structure (1PP9) with a direct

hydrogen bond at His201.(8) Both structures generally agree on the other residues that

may participate in stabilizing UQ bound at the Qi site. Structure representation is

prepared with VMD (10)

Although the Qi pocket is quite hydrophobic, there are numerous crystal structures with

bound inhibitors and partial electron density for the ubiquinone substrate that also show

115

water molecule electron densities near the binding pocket (7-9, 11). Based on a structure with bound antimycin, a competitive UQ inhibitor, Huang et al. suggested a mixture of two alternative conformations of UQ near the His201. One of the proposed conformations includes a water-mediated hydrogen bond to the UQ and the other is a direct hydrogen bond to the UQ (8). This interaction has been used to rationalize the re-protonation of the putative proton donor, His201. It has been further proposed that upon reduction of the UQ its direct hydrogen bond with His201 will be broken by transfer of the proton from His201 to the reduced semiquinone. The His201 side chain moves away and is recharged by taking up a proton from a nearby water molecule. The breaking of the hydrogen bond was thought to induce the release of product to the ubiquinol pool. More experiments will be needed to provide evidence for such extrapolations, but experimental studies of the water contributions in a catalytic mechanism can be challenging. Nonetheless, molecular dynamics simulations can address these questions by exploring and capturing different thermodynamically stable configurations.
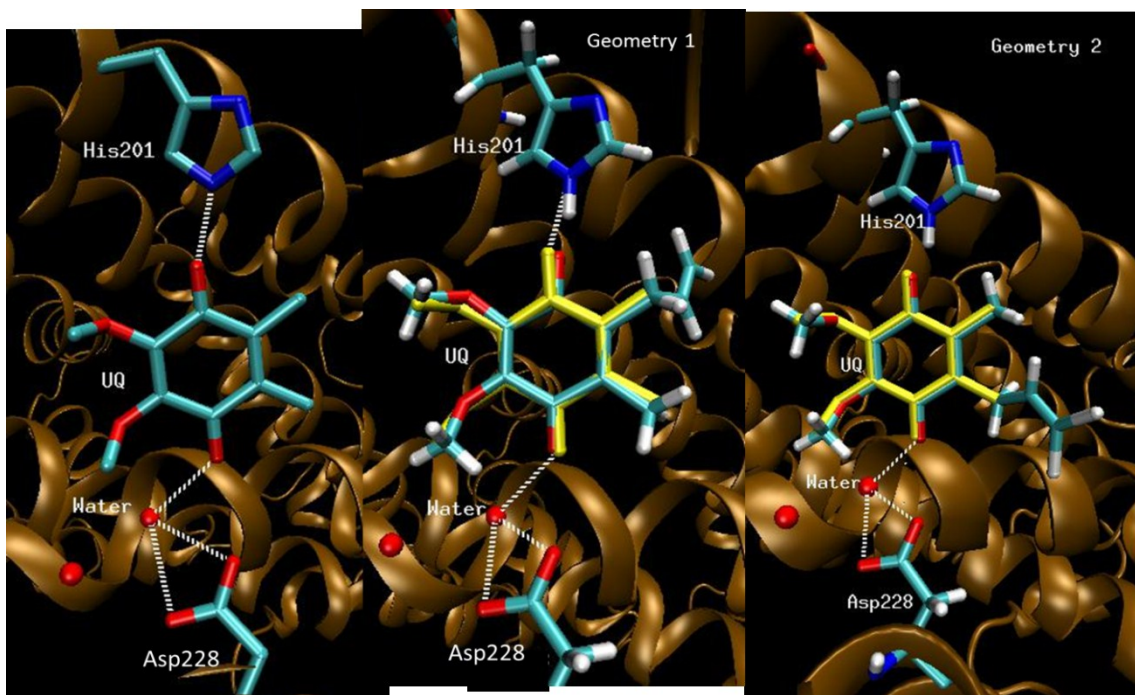
Figure 4.1.3: Two possible geometries to model a natural ubiquinone into the Qi binding site

The left figure is the coordinates obtained from X-ray crystal structure of the bovine cytochrome bc1 complex with side chains of His201, Asp228, a water oxygen atom and ubiquinone shown in a licorice representation, with carbon cyan, oxygen red, and nitrogen blue. The middle and right figures show two geometries different by having the ubiquinone model head group rotated by 180° around an axis perpendicular to the carbonyl C=O bonds. This rotation orients the (model) isoprenyl chain differently in the two geometries.

One limitation that both the yeast and bovine cyt bc1 X-ray structures share is that in both structures, the average B factor for the UQ is twice as large as those for the neighboring residues, indicating a <50% occupancy of the Qi site by UQ. Thus, UQ can be modeled

in two different ways without changing the refinement statistics. The two models differ from each other by flipping the UQ head group 180° as shown in Figure 4.1.3. More studies from X-ray diffraction crystallographic studies were done with various bound inhibitors, in order to refine the Qi binding pocket. A consensus has not been reached regarding the orientation of the UQ head group, the role(s) of mobile water molecules, and the different conformations of His201 and Asp228. The question remains unanswered whether the UQ reduction at the Qi site requires direct proton donation from the hydrogen-bonding residues His201 and Asp228 or indirect proton donation via water molecules and how the product QH2 is discharged from the Qi site to the ubiquinol pool. In addition, it is unknown what structural features or geometries favor the binding of UQ or semiquinone intermediates over binding of QH2. The identification of the proton donors near the Qi site, and consequently the mechanism of UQ reduction, remains debatable. If water molecules indeed play the role of proton donors during UQ reduction, it will be quite challenging for experimental methods to verify. Computational methods to study such large systems are also costly and time consuming. Perhaps this is why there have been no published computational studies to address these different hydrogen bond patterns and the dynamics of water molecules near the Qi site. In this work, we utilize the latest and most powerful computing architecture, an NVIDIA Tesla GPU, to accelerate the high-performance NAMD scalable MD software to study cyt bc1 in water. We examined both of the possible orientations of the UQ head group and observed several favorable binding geometries of UQ. The conformational dynamics of His201 in the protein environment and the mobile water molecules near the Qi site are discussed in terms of structural driving factors for reduction of UQ at the Qi site.

4.2. Material and methods

4.2.1. Ubiquinone force field parameters

Force field parameters for a UQ model, with the isoprenyl chain truncated as shown in

Figure 2.2.1 were developed and tested by members of the group (13-17). For different

quinones, including the current UQ model, electron affinities (13) were calculated using

the hybrid HF/DF B3LYP method (18, 19) and the one electron reduction potentials were

calculated using FEP/MD simulations (20-25). The results were in excellent agreements

with experiments (13-17) indicating the derived force field parameters for UQ are

reliable. UQ charges were calculated using B3LYP/6-31G(d) (26, 27) and the CHELPG

scheme (28). Force constants were calculated using the vibrational analysis in the

Gaussian quantum chemistry program (18). Non bonded parameters were obtained from

similar atom types in the CHARMM22 force field (29).
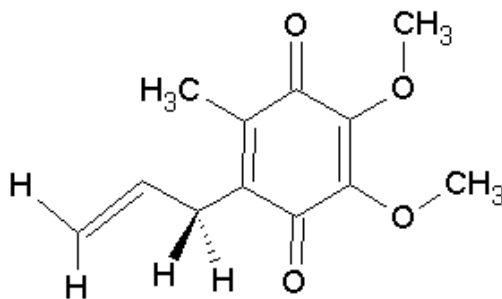

Figure 4.2.1: The ubiquinone model

The ubiquinone model with a methyl group removed from the isoprenyl chain and the

chain truncated after two carbon atoms. Model representation was prepared with

ChemSketch (30).

119

4.2.2. Preparation of initial structures

The initial starting structure included the catalytic core subunits: cytochrome b with two iron containing hemes, bL and bH, and the iron sulfur protein (ISP) head domain with an iron-sulfur cluster (ISC). These subunits were truncated from a bovine cytochrome bc1 complex crystal structure obtained from the Protein Data Bank (http://www.rcsb.org/pdb/home/home.do), PDB ID 1PP9 (8). The 1PP9 structure by Huang et al. was selected because of its well defined nature, with a resolution of 2.1Å and an R-value of 0.25. Because we chose the Huang et al. structure, the initial geometry includes His201 started in the position of a direct hydrogen bond donor. However, mobile water molecules near the Qi site can freely move in within the hydrogen bond distance with His201 and UQ and form water-bridging hydrogen bonds if it is indeed thermodynamically favorable. On the other hand, if we had started the water-mediated hydrogen bonds between His201 and the UQ, it was not likely that the direct hydrogen bond can form. . We also included all crystallographic water molecules from the cytochrome b subunit and named them differently to distinguish them from the solvent water molecules added later.

We used VMD (10) (http://www.ks.uiuc.edu/Research/vmd/) to prepare the starting structure. The N-terminus and C-terminus were capped with acetylate and amidate, respectively. All hydrogen atoms and heavy atoms missing from the X-ray crystal structure were placed using standard values from CHARMM force field parameters (29) and all undefined atoms from the X-ray structure were deleted. The UQ model was placed at the Qi site according to the crystal structure (8) in two possible orientations differing from each other by a 180° rotation around an axis perpendicular to the UQ C=O

bonds (Figure 4.1.3). The His201 initially started as a direct hydrogen bond donor to the UQ model while Asp228 initially started with a water-mediated hydrogen bond to the UQ model.

4.2.3. Molecular dynamics simulations

MD simulations are based on Newton's second law of motion stating that the force acting on particle i (F_i) is proportional to the acceleration of particle i (a_i): $F_i = m_i a_i$. The force acting on a system of particles can also be calculated as the negative gradient of the potential energy $F_i = -\nabla_i V$ and thus Newton's equation of motion can be used to relate the derivatives of the potential energy to changes in position as a function of time. Integration of the equations of motion yields a trajectory that describes the positions and velocities (as well as the accelerations) of the particles as they vary with time. From the trajectories generated by a molecular dynamics simulation, the average values of physical properties can be determined

The CHARMM22/CMAP force field was used for atoms of the protein and for heme groups (29, 31). For the iron-sulfur cluster, atomic charges were taken from published DFT with VWN and PW91 functionals calculations of Uhlmann et al. (32) and Lennard-Jones parameters were from heme iron and dimethyldisulphide of the CHARMM22 were used. Force constant were obtained from Drieding force filed (33). The system was solvated with 10Å of TIP3P water molecules (34) in each direction. Sodium chloride was added to neutralize and bring the system to the physiological ionic strength using plugins from VMD (10). A one femtosecond time step was used in isothermal, isobaric (constant NPT) simulations, with temperature maintained at 300K using Langevin dynamics with a damping coefficient of 5.0 ps^{-1} and pressure was maintained at 1atm using a Langevin

piston. The cutoff for electrostatic and van der Waals interactions was 12Å with a switching function on and a switching cutoff of 10Å. Periodic boundary conditions were applied with the Particle Mesh Ewald (PME) (35) grid spacing of 1.0Å for a full system periodic electrostatic potential. The NAMD standard energy minimization steps were performed followed by 2 ns of dynamics where all atoms of the UQ model and the His201 and Asp228 residues were fixed and a restraint of 10kcal/mol•$Å^2$ was placed on all C-alpha atoms. The restraints were removed slowly in increments of 0.5kcal/mol•$Å^2$ for every 1ps to allow the protein's side chains to relax around the hydrogen bonds between the amino acid side chains and the UQ substrate. Routine checks for the potential energy over time and the RMSD of protein backbone from the X-ray diffraction structure over time show convergence of the system. After complete removal of the C-alpha's restraints, the constraints on His201, Asp228 and UQ were then removed and the system was allowed to equilibrate for another 2ns. After equilibration, the RMSD value of the protein backbone fluctuated around 2.2Å relative to the crystal structure. A total of 13ns of dynamics simulation data after equilibration was used for analysis.

4.3. Results and discussion

4.3.1. Conformational dynamics of His201 and mobile water molecules

Our MD simulations for two different starting geometries of the UQ head group that are 180° different from each other (see Figure 4.1.3) showed that the direct hydrogen bond from His201 to the UQ is maintained for only one geometry. The His201 epsilon hydrogen (HE2) on the imidazole ring remained within hydrogen bonding distance ($\leq$ 2.5Å) to one of the two carbonyl oxygen atoms of the UQ for 68% of the 15 ns simulated time for starting geometry 1. For starting geometry 2, on the other hand, the same direct

hydrogen bond was maintained for only 2.6% of the simulated time. Figure 4.3.1 shows two histograms for the distance between the epsilon hydrogen of His201 and the carbonyl oxygen of UQ from the two starting geometries. Geometry 1 has three populations with an almost-Gaussian distribution for each. The largest population was within hydrogen bond distance, with the most populous distance approximately 2Å. There are two smaller populations, one with the most populous distance of approximately 5Å, which could accommodate a bridging water. However, our trajectories showed water molecules tend to occupy only a region near the delta nitrogen of His201 and instead the His201 side chain breaks its hydrogen bond to UQ and rotates out of the Qi binding pocket. We did not observe any water-bridged hydrogen bonds at the His201. The third and smallest population ranged from 6 - 12Å, too large a distance for a water-bridged hydrogen bond. Geometry 2 also showed three populations at similar distances. However, only 2.6% of the population was within hydrogen bonding distance. A large population (59% of the total) showed the HE2 of His201 was 8 – 11Å away from a UQ carbonyl oxygen. This distance was too large for a water-mediated hydrogen bond and most likely represents an intermediate in the His201 side chain rotation out of the UQ binding pocket. The second largest population (29% of the total) appears at ~13Å and occurs when the His201 side chain has moved completely out of the binding pocket and was exposed to bulk solvent. Thus, we did not observe water-mediated hydrogen bonds involving the His201 epsilon nitrogen. Our trajectories showed water molecules tend to occupy only a region near the delta nitrogen of His201 and direct the His201 side chain to move out of the Qi binding pocket. Thus, starting geometry 1 gave a much higher population of geometries

123

displaying the direct hydrogen bond from His201 epsilon nitrogen to the UQ carbonyl

oxygen than geometry 2.
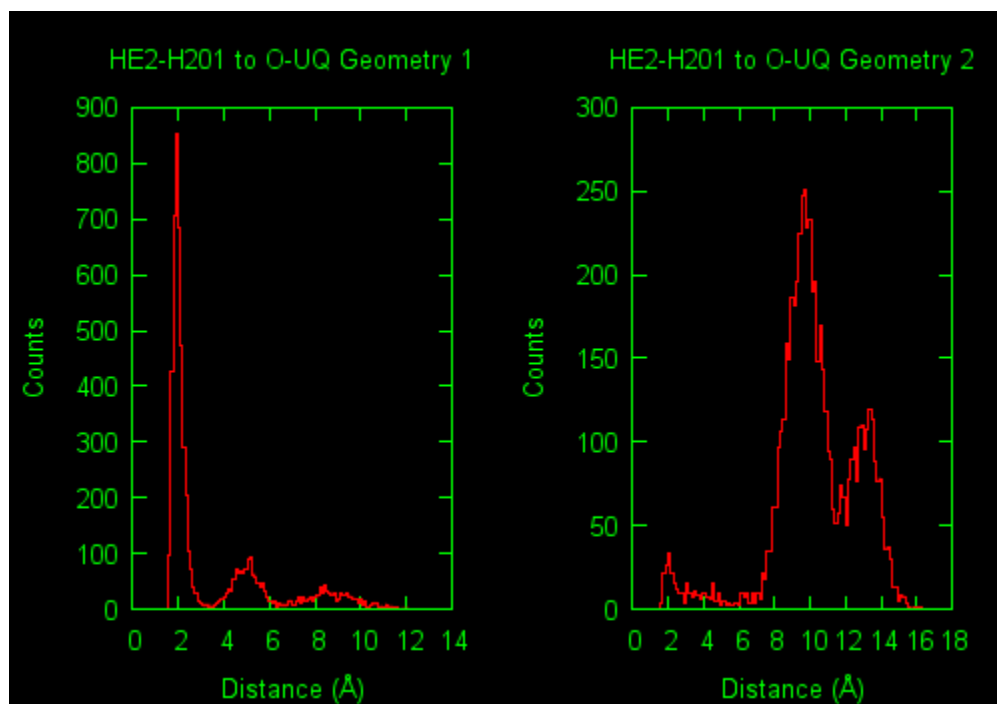
Figure 4.3.1: The distribution of distances between the His201 side chain and the

carbonyl oxygen on ubiquinone

The distribution of distances between the epsilon hydrogen (HE2) on the His201 side

chain and the carbonyl oxygen on the ubiquinone (UQ) ring for starting Geometries 1 and

2, defined in the two right-most panels of Figure 4.3.1. Integrating the distribution to the

position of the first minimum for Geometry 1 shows that the His201 HE2 atom appears

at a distance less than 2.5 Å from UQ i.e., within direct hydrogen bonding distance to the

UQ in 68% of the configurations. Similar integrations of the distribution for Geometry 2

show that the HE2 atom is found less than 2.5 Å from UQ in only 2.4% of configurations,

whereas, it appears within 8-11Å of UQ , too large a distance for even a water-mediated

hydrogen bond to UQ, in 59% of configurations.

In summary, our trajectories identified three predominant conformations of the His201 side chain. The most highly populated geometry included a direct hydrogen bond from the His201 epsilon nitrogen to one of the carbonyl oxygen on the UQ. We did observe the rotation of the His201 side chain out of the binding pocket in our dynamic trajectories. This movement was directed by mobile water molecules hydrogen bonded to the His201 delta nitrogen. These water molecules were not oriented in such a way to form a water-bridged hydrogen bond to the UQ head group. Figure 4.3.2.2 shows the volume map for water occupancy within 3.5 Å of the His201 $N\varepsilon$ atom and the UQ carbonyl oxygen for starting geometries 1 and 2. In geometry 1, this volume has a donut shape with no water occupancy in the middle, where one would expect a water if it were engaged in water-bridged hydrogen bonding. In geometry 2, water molecules predominantly occupied the $N\delta$ side of the His201 side chain. Our trajectories implied movement directed by water molecules hydrogen bonded to the $N\delta$ of His201, resulting in an intermediate population with a distance between His201 and UQ of about 5Å i.e., the direct hydrogen bond at $N\varepsilon$ was not maintained. Once the hydrogen bond no longer exists, more mobile water molecules can freely access the carbonyl oxygen on the UQ and eventually pushed the His201 side chain away, resulting in a third population that was approximately 10Å away from the UQ carbonyl oxygen atom. It is unlikely that the His201 can ever move back into the Qi binding pocket, unless some significant change in conformation occurs, possibly upon substrate reduction or release of the product. Our observation is consistent with the yeast cyt bc1 complex crystal structure from Hunte at el. (9) which showed a geometry including a hydrogen bond between water and the delta nitrogen of His201.

Our results supported Huang et al.'s proposal of a direct hydrogen bond between His201 and UQ in bovine cyt bc1 complex (8). In summary, MD simulations of the conformational dynamics give insights into the various hydrogen bonding patterns between the UQ carbonyl oxygen atom and the His201 side chain, including those involving water molecules.

4.3.2. Conformational dynamics of Asp228 and mobile water molecules

The computed pKa value of Asp228 (chapter 2) allows us to assign the deprotonated state for Asp228 in the initial UQ binding geometry where the carboxylated oxygen appeared within hydrogen bonding distance of a water, which in turn contacted the carbonyl oxygen on the UQ ring within a typical hydrogen-bonding distance (< 2.5 Å between the hydrogen bond acceptor atom and the hydrogen atom). The water-bridged hydrogen bond between the unprotonated Asp228 and the second carbonyl oxygen atom on the UQ was maintained throughout the 15 ns simulation time for both starting geometries 1 and 2. Figure 4.3.2.1 shows two histograms of the distance between Asp228 carboxylate oxygen and the carbonyl oxygen on UQ. Configurations generated from geometry 1 show mainly two populations, shaped almost like a Gaussian distribution. The first population ranged from 3 - 5Å and the most highly populated distance (also the average distance for a pure Gaussian distribution) was 4.4Å. This is probably too small a space to fit a bridging water molecule in a linear hydrogen-bonding geometry between the carboxylic oxygen on Asp228 and the carbonyl oxygen on UQ. However, it will nicely fit a water molecule at an angle less than 180°. The second population ranged from 5 – 7 Å with the most populated distance at 5.7 Å, which can fit a water molecule in a linear hydrogen-bonding geometry. Figure 4.3.2.2 shows the volume map for the water occupancy within 3.5 Å of

the Asp228 carboxylic oxygen and the UQ carbonyl oxygen. For geometry 1, the water occupied a large area covering almost the entire carboxylate group, thus the hydrogen bond can hop between carboxyl oxygen atoms OD1 or OD2 throughout the simulation. In contrast, configurations generated from geometry 2 show that only the OD1 has access to water and consequently geometry 2 shows only one population, with a nearly Gaussian distribution. The most populated distance (approximately the average distance) is 4Å. We did not observe any stable conformations with a direct hydrogen bond between the Asp228 side chain and the carbonyl oxygen of UQ. Although it is unlikely for Asp228 (pKa ~ 4) to be protonated at physiological pH, we protonated Asp228 to test its ability to form a direct hydrogen bond to the carbonyl oxygen of UQ. Even in this hypothetical situation, the protonated Asp228 still did not form a hydrogen bond to the UQ carbonyl oxygen. On the other hand, the water molecules near UQ and Asp228 are extremely mobile and continuously move in and out of the bridging position so that there was always one water-mediated hydrogen bond from the Asp228 side chain to the UQ carbonyl oxygen.
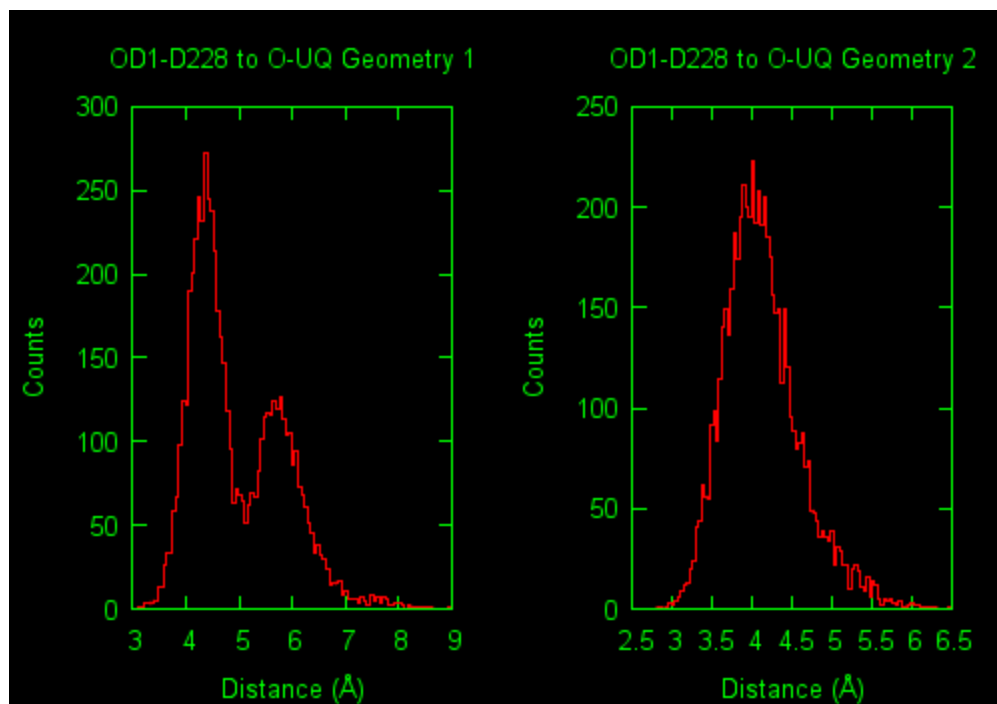
Figure 4.3.2.1: The distribution of distances between the carboxylate oxygen on Asp228 side chain and the carbonyl oxygen on ubiquinone

The distribution of distances between the carboxylate oxygen on the Asp228 side chain (OD1) and the carbonyl oxygen on the ubiquinone (UQ) ring for starting geometries 1 and 2. Geometry 1 shows two primary populations with the distance from OD1 spanning 3 – 5Å and 5 - 7Å from the carbonyl oxygen atom on UQ. The most populous distances are 4.4 Å and 5.7 Å, consistent with a bridging water molecule oriented to form a linear hydrogen bond with the Asp228 OD1 atom and the UQ carbonyl oxygen atom. Geometry 2 shows one peak with an almost Gaussian distribution. The most populous distance (approximately the average distance) is 4 Å and is consistent with a bridging water molecule to form hydrogen bonds with both Asp228 and UQ. Both geometries maintain a stable water-bridged hydrogen bond distance from the Asp228 side chain to UQ.
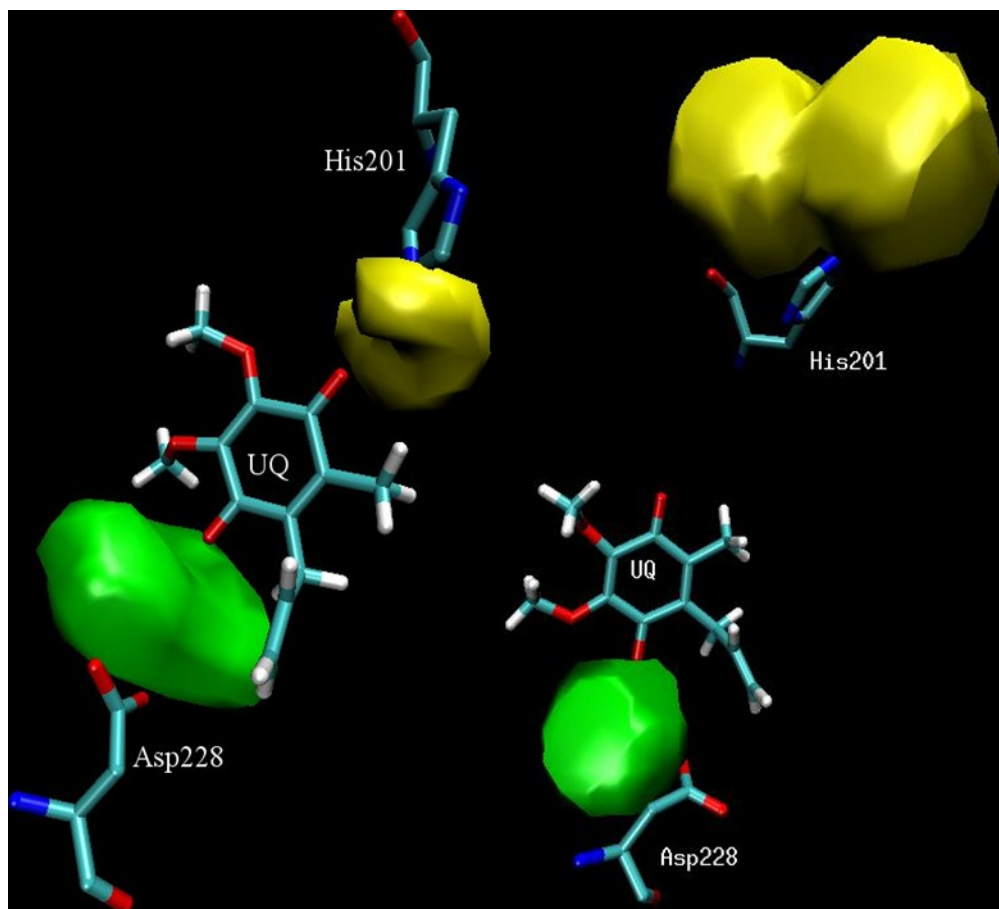
Figure 4.3.2.2: The volume map for water occupancy within 3.5 Å of the Asp228 carboxylic oxygen and the UQ carbonyl oxygen

For geometry 1, the water occupies a large area (green) covering almost the entire carboxylate group whereas in geometry 2, only the OD1 has access to water. Consequently, the water-mediated hydrogen bond in geometry 1 can hop from either carboxylate oxygen OD1 or OD2 while that in geometry 2 can only form a hydrogen bond at OD1. The volume map for the water occupancy within 3.5 Å of the His201 epsilon nitrogen and the UQ carbonyl oxygen (yellow) has a donut shape in geometry 1, indicating no water-bridging hydrogen bond to UQ. Both geometries show water-accessible sites near the delta nitrogen of His201.

In summary, for both bovine cyt bc1 structures from Gao et al. and Huang et al. the Asp228 was suggested to interact with UQ via a water-bridging hydrogen bond. Our MD simulation trajectories confirmed that the Asp228 did not form a direct hydrogen bond the carbonyl oxygen on the UQ head group. Although Asp228 is highly conserved in both bovine and yeast, we did not observe any stable conformation with Asp228 directly forming a hydrogen bond to UQ as shown in the yeast cyt bc1 complex by Hunte et al (9). Another critical point drawn from MD simulations was the hydrogen bonds formed by mobile water molecules near the UQ and Asp228 in the Qi site, which ensures free access to a nearly endless source of proton donors, the bulk solvent. Although the well-defined Qi pocket borders the hydrophobic core of the inner membrane phospholipid, which was omitted (a limitation of this work), we included the well-defined crystallographic water molecules in the spacious Qi pocket. It is also noteworthy to report a direct opening from the Qi pocket to the aqueous phase via a highly flexible loop at the N terminus of cytochrome b consisting of charged and highly flexible Lys12 and Met11 which will be discussed later.

4.3.3. Orientation and dynamics of the aromatic residues near the Qi site

Residues Phe18 and Phe220 are conserved in most species except yeast. Based on various X-ray diffraction crystal structures with bound inhibitors and substrate, Phe220 was suggested to have pi-pi interactions (40) possibly to hold the UQ ring in a proper orientation for electron transfer reactions and Phe18 was suggested to make contact with antimycin, a UQ inhibitor (7, 8). To examine the orientations of the Phe220 aromatic ring around the UQ ring, we measured the angle between the normals to the ring planes of Phe220 and the UQ. We calculated the normal to the ring plane by taking the cross

130

products of two vectors formed from the center of mass of the ring to two different atoms on the ring plane. From the magnitudes of the dot products of these normals to the ring vectors, the angle between them can be calculated. Because of the way we calculated this angle, θ and $180° - \theta$ essentially describe equivalent orientations of the two rings (Figure 4.3.3.1).
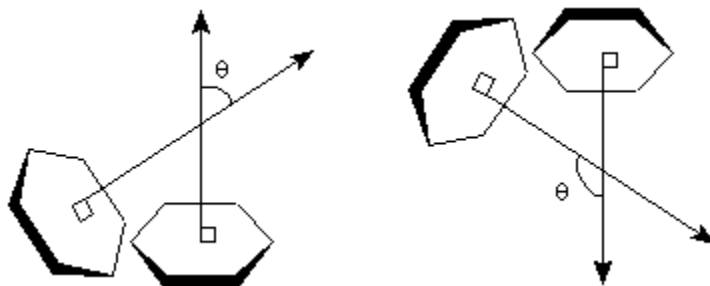
Figure 4.3.3.1: The normal to the ring plane vectors and the angles (θ) between these normals

The angles (θ) between these normal vectors are calculated from their dot product. Both θ and $180° - \theta$ angles correspond to equivalent orientation of the rings

Figure 4.3.3.2 shows the distributions of this angle for starting geometries 1 and 2. From geometry 1, we observed two populations, one with the most populated angle at 55° and another at 96°. The Phe220 aromatic ring is not parallel to the UQ ring, and thus there was no $\pi - \pi$ stacking interaction. However, the two predominant arrangements represent an approximate edge (Phe220) to face (UQ) orientation (Figure 4.3.3.2) probably because the partially positively charged hydrogen on the Phe220 exhibits dipole-dipole interactions with the negatively charged atoms on the UQ ring. Studies of protein folding

established that such interactions can contribute to protein stabilization up to 1.3 kcal/mol in free energy (41). Phe220 was reported to form an angle of about 77° to the salicyl ring on antimycin, a UQ inhibitor, in a published X-ray crystal structure (8). Geometry 2 shows an angle distribution that closely approximates a Gaussian distribution with the most populated angle (in this case, almost the average angle) of 105°. The biological implication for this observation is that the interaction of Phe220 contributes to orient UQ at the Qi site in an edge to face interaction.

Figure 4.3.3.2: : Distributions of the angle θ between normals to the Phe220 aromatic ring and the UQ ring

Distributions of the angle θ between normals to the Phe220 aromatic ring and the UQ ring from simulations starting in geometries 1 and 2. Geometry 1 has two primary populations spanning 40° to 120° with the most populous angles at 55° and 96°.

Geometry 2 has an approximately Gaussian distribution and an average angle of 105°,
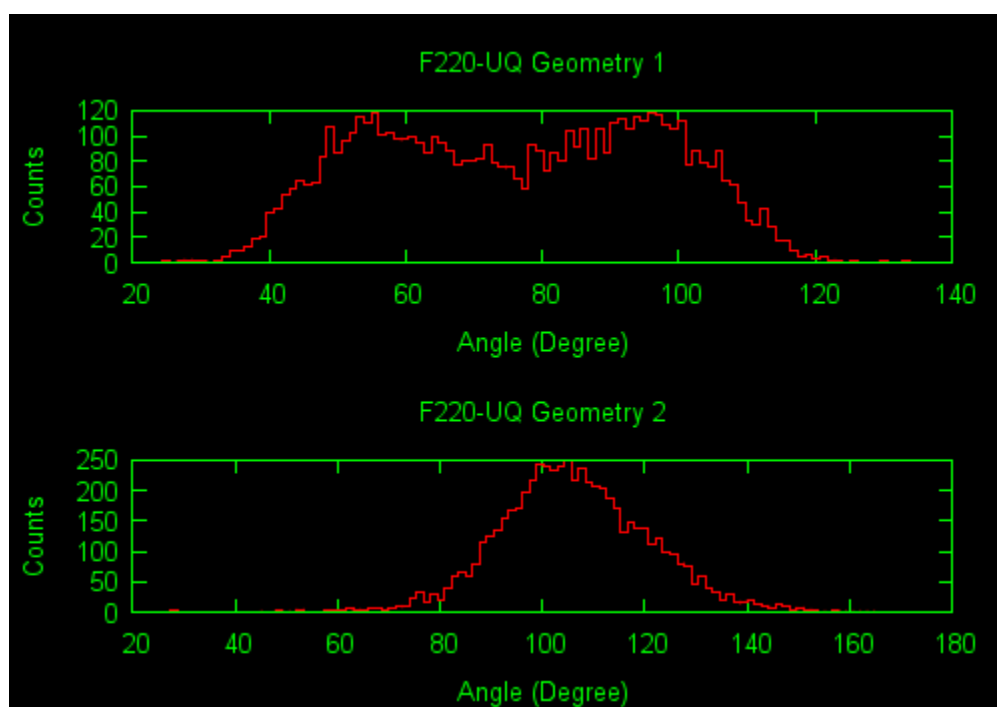corresponding to an edge-to-face   interaction.
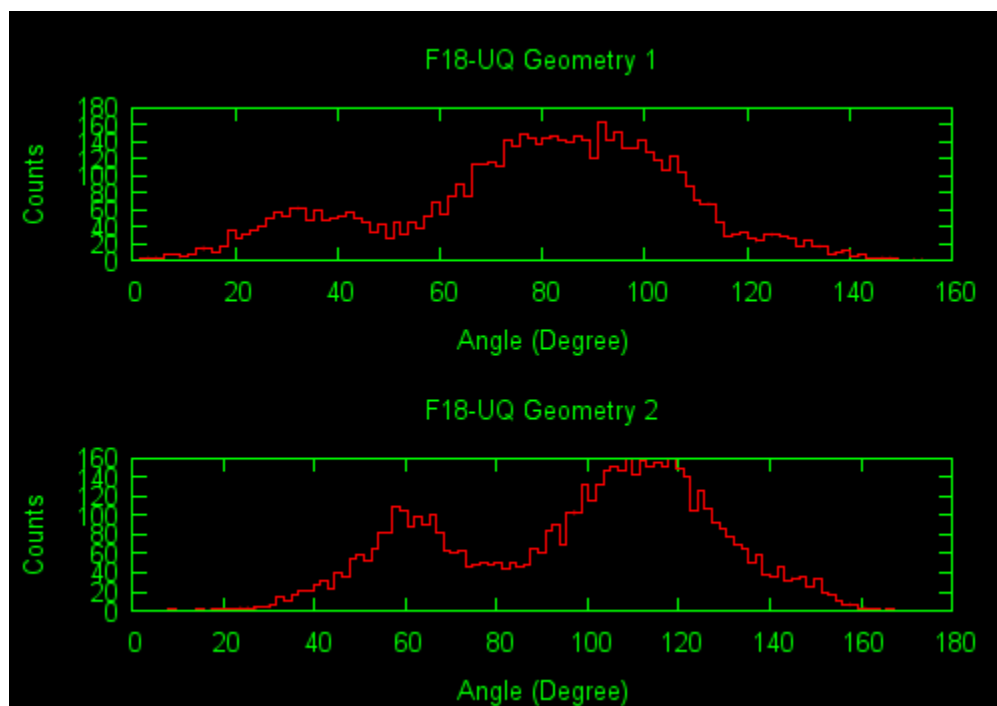
Figure 4.3.3.3: Distributions of the angle θ between normals to the Phe18 aromatic ring
and the UQ ring
 Distributions of the angle θ between normal to the Phe18 aromatic ring and the UQ ring
from simulations starting in geometries 1 and 2. Both geometries have two primary
populations. One corresponds to the open form and the other corresponds to the closed
form of the Qi entrance, where the cytochrome b N-terminus is exposed outward toward
bulk solvent or closed inward to the protein interior, respectively. In all cases, an edge to
face orientation between the rings is preferred

Phe18 has received less attention than Phe220, because it is located further away from the UQ position and closer to the cyt b N-terminal loop in the X-ray structure. Our trajectories show that Phe18 moves closer to the Qi binding pocket as the N-terminal loop flexes toward the protein interior. Figure 4.3.3.3 shows the distribution of the angles between the normal to the ring planes of UQ and Phe18 for starting geometries 1 and 2. Both have two predominant populations. One accounts for a set of conformations with the N-terminal tail pointing outward to the bulk solvent and the other is a set of conformations with the N-terminus pointing toward the Qi pocket (Figure 4.3.3.4). The latter geometry brings the Phe18 side chain close to the UQ head group as His201 moves away. For geometry 1, the larger population spans 80° to 100° and describes an edge to face orientation of the rings. The smaller population is centered about 30° and accounts for Phe18 when the N-terminus of cyt b points toward bulk solvent. For geometry 2, we also observed two primary populations, one near 60° and one near 120°. Both of these populations describe an edge to face orientation of the two rings. Although the trajectories did not show any π - π stacking they did show that the most favorable geometries have the edge (C - H) of the aromatic rings pointing at the face of the UQ ring (Figure 4.3.3.4).
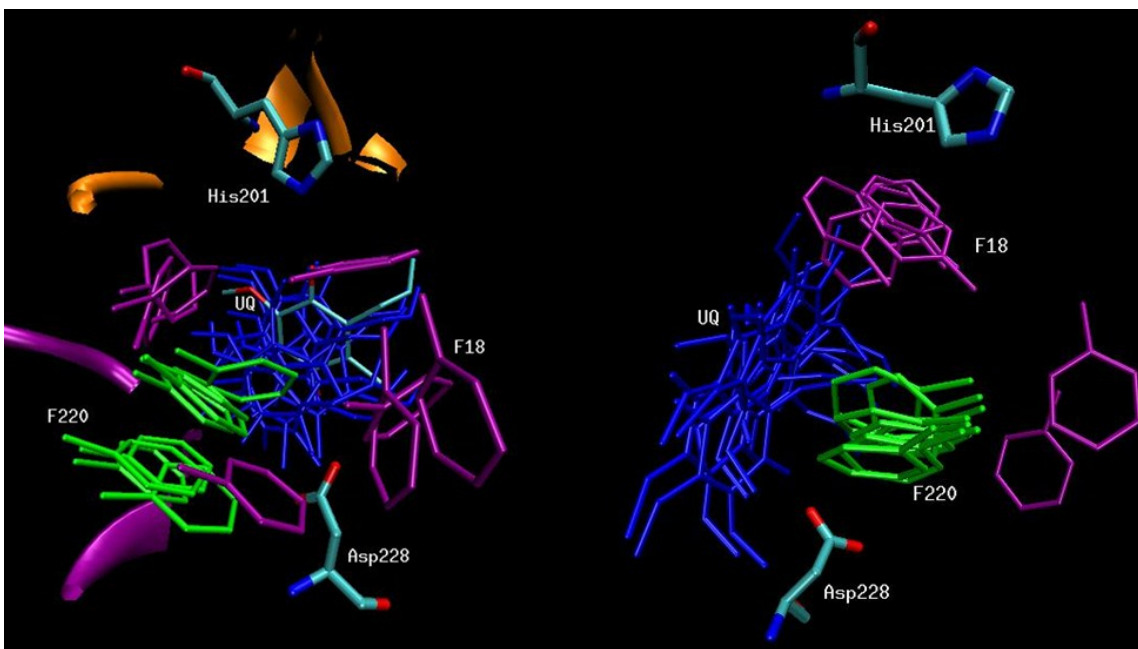
Figure 4.3.3.4: Multiple frames of UQ and the aromatic residue side chains near the Qi site

Multiple frames of UQ and the aromatic residue side chains near the Qi site for starting geometries 1 (left) and 2 (right). In geometry 1, the aromatic ring of Phe220 (green) has predominantly two edge to face orientations toward the UQ ring (blue); the ring of Phe18 (purple) also prefers two geometries: both are edge to face orientations toward the UQ ring, corresponding to two different geometries of the cytochrome b N-terminal loop.

4.3.4.   Conformational dynamics of other significant residues near the Qi site

Ser205 is conserved in most species and was suggested to participate in UQ binding based on X-ray diffraction structures with bound inhibitors and substrate (7). Ser205 in the bovine cyt bc1 complex is within hydrogen bonding distance of the methoxy oxygen of UQ. Our results show that from starting geometry 1, the hydroxyl hydrogen of Ser205 maintains a close distance (the most populous distance was 3.5Å) to the methoxy oxygen

atom on the UQ. We observed that Ser205 also maintains a hydrogen bond with a crystallographic water molecule, (W3033) throughout the simulation. This water also maintained a hydrogen bond with the carbonyl oxygen atom on the bH heme throughout the entire simulation. Our observations indicate that the Ser205 geometry close to the methoxy oxygen of the UQ and within 3.5 Å of the heme bH (with a bridging water (W3033) in between) is indeed favorable (Figure 4.3.4). The results from geometry 2 show similar behavior, with distances between the Ser205 hydroxyl hydrogen and the methoxy oxygen on UQ spanning a larger range, from 2.5Å to 7Å. A crystallographic water also bridged and maintains a distance of 2Å and 2.6Å to Ser205 and to the heme bH respectively.
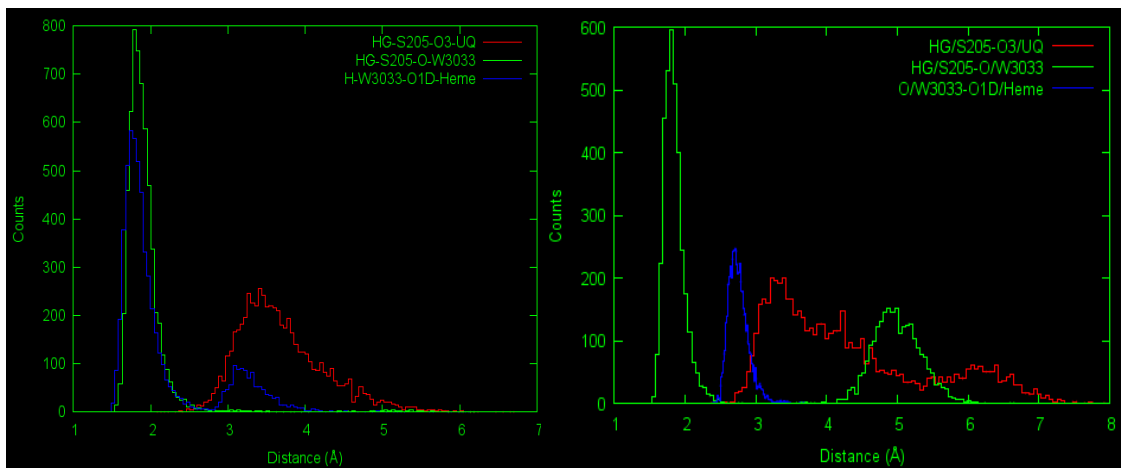
Figure 4.3.4: Distributions of distances from the hydroxyl hydrogen of Ser205 to a UQ and a structural water
 Distributions of distances from the hydroxyl hydrogen of Ser205 to a UQ methoxy oxygen and to a structural water molecule for starting geometries 1 and 2. The Ser205 hydroxyl hydrogen atom maintained a close distance (< 3.5Å) indicating hydrogen-bonding interactions. Ser205 also maintained hydrogen bonding distance to a structural

136

water molecule present in the X-ray structure. This water also remained within hydrogen bonding distance of the carboxylate group on heme bH.

Lys227 was suggested by Gao et al. to participate in UQ reduction by fetching a proton from the matrix into the Qi site. The protonated Lys227 together with the deprotonated Asp228 can stabilize a water molecule close to UQ (5) that might act as a proton donor. A different study of the yeast cytochrome bc1 complex proposed a similar role for Lys227, in which it participates in a proton uptake pathway (although alignment of these two structures results in Lys227 pointing in different directions) (7, 11). We did not observe such significant behavior for Lys227. The flexible side chain of Lys227 indeed interacts with bulk solvent, but never comes close to the UQ head group nor leads any water molecules to come closer to the Asp228.

4.3.5. Open and closed arrangements of the Qi pocket near the cyt b N-terminus

Figure 4.3.5 shows multiple frames (every 500 picoseconds) of the N-terminal loop of cyt b. The figure shows two distinct geometries. In one geometry, the loop is oriented toward the matrix side and away from the Qi entrance, as observed in the X-ray structure from Gao et al. (the starting structure for this work) (7). In the other geometry, the loop points toward the protein interior and closes the Qi entrance, shielding it from the bulk solvent. Throughout the 15ns simulation, the N-terminus spent most of the time in the latter orientation, implying that the Qi entrance is most often closed from bulk solvent by the N-terminal loop. It is also noteworthy to mention that this N-terminus consists of mostly hydrophobic residues, except Ly12. Thus, our trajectories show that the hydrophobic N-

terminus favors a geometry that allows it to interact with the hydrophobic Qi entrance. We observe that the hydrophobic Met11, located in the N-terminal loop, prefers an arrangement that allows it to be close to Met190, located on helix D, which helps define the Qi binding site. The long hydrocarbon chains of Lys12, located at the beginning of the N-terminal loop, and Met194, located on helix D, show similar behaviors: prefer to be close to each other. And because these residues all have long and flexible side chains, they all remain in close proximity to one another. The change in conformation of the N-terminal loop to close the entry to the Qi site also results in Phe18 moving closer to the UQ ring as discussed previously. Met190 and Met194 were suggested to establish "contact" with the bound antimycin tail at the Qi site (7). Our result suggests that the hydrophobic residues Met190, Met194, Met11 and Lys12, located on opposite sides of the entrance to the Qi site, favor a geometry close to each other. While somewhat speculative, it is likely that the long hydrophobic chain of UQ may also be stabilized by these residues because of their hydrophobic nature. Thus, the primary role of the hydrophobic residues Met190, Met194, Met11 and Lys12 may be to control entry of UQ to and exit of QH2 from the Qi site.
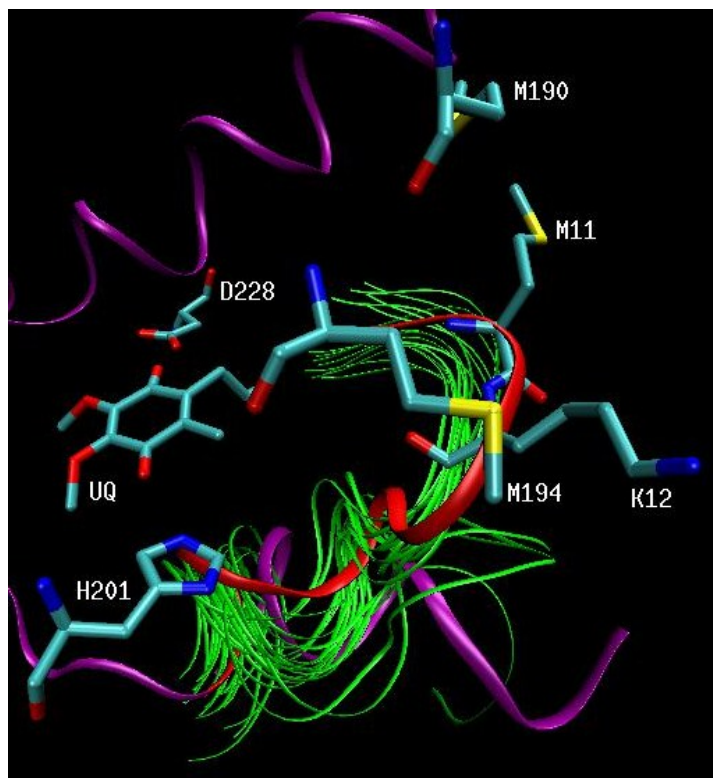
Figure 4.3.5: Multiple frames of the cytochrome b N-terminal loop

The initial and final geometries are shown in purple and red, respectively. The hydrophobic residues with long and flexible side chain are shown in licorice representation, with carbon cyan, nitrogen blue, sulfur yellow and oxygen red. There are two preferred geometries for this N-terminal loop. One is observed in the X-ray structure and shows the loop pointing into the bulk solvent, leaving the Qi pocket open. The other preferred geometry was observed in our dynamics simulations and shows the loop oriented toward the Qi pocket, closing the pocket and resulting in significantly less water exposure of the hydrophobic residues.

139

4.4. Conclusions

Our molecular dynamics simulations tested two possible UQ binding geometries (see Figure 4.1.3) previously reported in both yeast and bovine cyt bc1 structures with less than 50% occupancy for UQ. For simulations starting from geometry 1, the direct hydrogen bond from residue His201 to the carbonyl oxygen atom on the UQ was maintained for 68% of the simulation time. A water-mediated hydrogen bond from residue Asp228 to the UQ carbonyl oxygen in simulations from both starting geometries is also observed, however, from the starting geometry 1, where a direct hydrogen bond is more favorable, the UQ binding geometry appears more prevalent. In contrast, starting geometry 1 also allows more mobile water molecules to access the site near the Asp228. Consequently, water-mediated hydrogen bonds can form with both oxygen atoms on the carboxylic acid group of Asp228. In addition, Asp228 is more flexible and rotates continuously, with highly mobile water replacing one another to bridge the hydrogen bond with UQ. Although the UQ geometry with a water-mediated hydrogen bond to Asp228 appears quite favorable, the fact that these bridging waters are highly mobile means that eventually the water-mediated hydrogen bond will easily break and re-form. In simulations starting from geometry 2, where the direct hydrogen bond between Asp228 and UQ broke rather quickly, the water-mediated hydrogen bond at Asp228 is maintained throughout more of the simulation. Starting from this geometry, we observe less frequent rotation of the carboxylic group and less movement of the bridging water molecule(s). The water occupancy is concentrated near one carboxylate oxygen, OD1, and we observe an almost Gaussian distribution of the distance between OD1 of Asp228 and the carbonyl O2 of UQ. The distribution shows only one population and the most

populated distance can fit a bridging water between Asp228 OD1 and the carbonyl oxygen of UQ. In simulations starting from both geometries, Phe220 remains in edge to face orientations relative to the UQ ring, and thus is very likely to contribute to orienting the UQ headgroup for the proton coupled electron transfer at the Qi site. Of course, more intensive experimental and theoretical work is needed to provide mechanistic details. Nonetheless, our simulations provides structural and dynamical details relevant to the loose binding of substrate UQ near the Qi site and may help explain why the occupancy of UQ in published X-ray structures is low.

Other notable geometrical features include the conformation of the cyt b N-terminal loop, where the hydrophobic Met190, Met194, Met11 and Lys12 side chains, located on opposite sides of the channel leading from bulk solvent to the Qi site, cluster when the loop moves to close off the Qi binding pocket from bulk solvent. Although inclusion of a model for the membrane might hinder the motion of the N-terminal loop, our simulations imply that the loop's dynamics may serve to control substrate and inhibitor access to the Qi site in bovine cytochrome bc1. Site-directed mutagenesis experiments for Met190, Met194, Met11, and/or Lys12 could test this hypothesis.

Acknowledgments

References

1. Gray MW, Burger G, Lang BF. The origin and early evolution of mitochondria. Genome Biol. 2001;2(6):REVIEWS1018.

2. Mitchell P. Possible molecular mechanisms of the protonmotive function of cytochrome systems. J Theor Biol. 1976;62(2):327-67.

3. Lee D, El Khoury Y, Francia F, Zambelli B, Ciurli S, Venturoli G, et al. Zinc inhibition of bacterial cytochrome bc1 reveals the role of cytochrome b E295 in proton release at the qo site. Biochemistry. 2011;50(20):4263-72.

4. Samoilova RI, Kolling D, Uzawa T, Iwasaki T, Crofts AR, Dikanov SA. The interaction of the rieske iron-sulfur protein with occupants of the Q0-site of the bc1 complex, probed by electron spin echo envelope modulation. J Biol Chem. 2002;277(7):4605-8.

5. Zhang H, Osyczka A, Dutton PL, Moser CC. Exposing the complex III qo semiquinone radical. Biochim Biophys Acta, Bioenerg. 2007;1767(7):883-7.

6. Cape JL, Bowman MK, Kramer DM. A semiquinone intermediate generated at the qo site of the cytochrome bc1 complex: Importance for the q-cycle and superoxide production. Proc Natl Acad Sci U S A. 2007;104(19):7887-92.

7. Gao X, Wen X, Esser L, Quinn B, Yu L, Yu C, et al. Structural basis for the quinone reduction in the bc1 complex: A comparative analysis of crystal structures of

mitochondrial cytochrome bc1 with bound substrate and inhibitors at the qi site. Biochemistry. 2003;42(30):9067-80.

8. Huang L, Cobessi D, Tung EY, Berry EA. Binding of the respiratory chain inhibitor antimycin to the mitochondrial bc1 complex: A new crystal structure reveals an altered intramolecular hydrogen-bonding pattern. J Mol Biol. 2005;351(3):573-97.

9. Hunte C, Koepke J, Lange C, Rossmanith T, Michel H. Structure at 2.3 Ã… resolution of the cytochrome bc1 complex from the yeast saccharomyces cerevisiae co-crystallized with an antibody fv fragment. Structure (London). 2000;8(6):669-84.

10. Humphrey W, Dalke A, Schulten K. VDM: Visual molecular dynamics. J Mol Graphics. 1996;14(1):33,8, plates, 27-28.

11. Lange C, Nett JH, Trumpower BL, Hunte C. Specific roles of protein-phospholipid interactions in the yeast cytochrome bc1 complex structure. Embo J. 2001;20(23):6591-600.

12. Lee MS, Salsbury FR, Jr., Brooks CL,III. Constant-pH molecular dynamics using continuous titration coordinates. Proteins: Struct , Funct , Bioinf. 2004;56(4):738-52.

13. Boesch SE, Grafton AK, Wheeler RA. Electron affinities of substituted p-benzoquinones from hybrid hartree-fock/density-functional calculations. J Phys Chem. 1996;100(24):10083-7.

14. Wheeler RA. A method for computing one-electron reduction potentials and its application to p-benzoquinone in water at 300 K. J Am Chem Soc. 1994;116(24):11048-51.

15. Raymond KS, Grafton AK, Wheeler RA. Calculated one-electron reduction potentials and solvation structures for selected p-benzoquinones in water. J Phys Chem B. 1997;101(4):623-31.

16. Grafton AK, Wheeler RA. Amino acid protonation states determine binding sites of the secondary ubiquinone and its anion in the rhodobacter sphaeroides photosynthetic reaction center. J Phys Chem B. 1999;103(25):5380-7.

17. Wise KE, Grafton AK, Wheeler RA. Trimethyl-p-benzoquinone provides excellent structural, spectroscopic, and thermochemical models for plastoquinone-1 and its radical anion. J Phys Chem A. 1997;101(6):1160-5.

18. Frisch MJ, Trucks GW, Schlegel HB, Scuseria GE, Robb MA, Cheeseman JR, et al. Gaussian 09, revision A1**
**. 2009.

19. Stephens PJ, Devlin FJ, Chabalowski CF, Frisch MJ. Ab initio calculation of vibrational absorption and circular dichroism spectra using density functional force fields. J Phys Chem. 1994;98(45):11623-7.

20. Straatsma TP, McCammon JA. Computational alchemy. Annu Rev Phys Chem. 1992;43:407-35.

21. Beveridge DL, DiCapua FM. Free energy via molecular simulation: Applications to chemical and biomolecular systems. Annu Rev Biophys Biophys Chem. 1989;18:431-92.

22. Van Gunsteren WF, Berendsen HJC. Molecular dynamics computer simulation. method, application and perspectives in chemistry. Angew Chem. 1990;102(9):1020-55.

23. Kollman P. Free energy calculations: Applications to chemical and biochemical phenomena. Chem Rev (Washington, D C). 1993;93(7):2395-417.

24. Jorgensen WL. Free energy calculations: A breakthrough for modeling organic chemistry in solution. Acc Chem Res. 1989;22(5):184-9.

25. Reynolds CA, King PM, Richards WG. Free energy calculations in molecular biophysics. Mol Phys. 1992;76(2):251-75.

26. Becke AD. Density-functional thermochemistry. III. the role of exact exchange. J Chem Phys. 1993;98(7):5648-52.

27. Stephens PJ, Devlin FJ, Chabalowski CF, Frisch MJ. Ab initio calculation of vibrational absorption and circular dichroism spectra using density functional force fields. J Phys Chem. 1994;98(45):11623-7.

28. Breneman CM, Wiberg KB. Determining atom-centered monopoles from molecular electrostatic potentials. the need for high sampling density in formamide conformational analysis. J Comput Chem. 1990;11(3):361-73.

29. Brooks BR, Bruccoleri RE, Olafson BD, States DJ, Swaminathan S, Karplus M. CHARMM: A program for macromolecular energy, minimization, and dynamics calculations. J Comput Chem. 1983;4(2):187-217.

30. Advanced Chemistry Development, Inc. (ACD/Labs). ACD/ChemSketch freeware. 2009.

31. MacKerell AD, Jr., Feig M, Brooks CL,III. Improved treatment of the protein backbone in empirical force fields. J Am Chem Soc. 2004;126(3):698-9.

32. Ullmann GM, Noodleman L, Case DA. Density functional calculation of pKa values and redox potentials in the bovine rieske iron-sulfur protein. JBIC, J Biol Inorg Chem. 2002;7(6):632-9.

33. Mayo SL, Olafson BD, Goddard WA,III. DREIDING: A generic force field for molecular simulations. J Phys Chem. 1990;94(26):8897-909.

34. Jorgensen WL, Chandrasekhar J, Madura JD, Impey RW, Klein ML. Comparison of simple potential functions for simulating liquid water. J Chem Phys. 1983;79(2):926-35.

35. Essmann U, Perera L, Berkowitz ML, Darden T, Lee H, Pedersen LG. A smooth particle mesh ewald method. J Chem Phys. 1995;103(19):8577-93.

36. Khandogin J, Brooks CL,III. Toward the accurate first-principles prediction of ionization equilibria in proteins. Biochemistry. 2006;45(31):9363-73.

37. Wallace JA, Wang Y, Shi C, Pastoor KJ, Nguyen B, Xia K, et al. Toward accurate prediction of pKa values for internal protein residues: The importance of conformational relaxation and desolvation energy. Proteins: Struct , Funct , Bioinf. 2011;79(12):3364-73.

38. Shepherd RE. Association of imidazoles and L-histidine with the pentacyanoiron(II) and -(III) moieties. J Am Chem Soc. 1976;98(11):3329-35.

39. Kokhan O, Shinkarev VP. All-atom molecular dynamics simulations reveal significant differences in interaction between antimycin and conserved amino acid residues in bovine and bacterial bc1 complexes. Biophys J. 2011;100(3):720-8.

40. Gao X, Wen X, Yu C, Esser L, Tsao S, Quinn B, et al. The crystal structure of mitochondrial cytochrome bc1 in complex with famoxadone: The role of aromatic-aromatic interaction in inhibition. Biochemistry. 2002;41(39):11692-702.

41. Burley SK, Petsko GA. Aromatic-aromatic interaction: A mechanism of protein structure stabilization. Science (Washington, D C , 1883-). 1985;229(4708):23-8.

CHAPTER 5

SUMMARY AND FUTURE WORK

Coupled electron and proton transfer (CEPT) reactions are fundamental for many bioenergetic conversions, conversions that involve approximately 100 times greater energy than all human energy usage combined, including fossil fuels (gas, oil) and nuclear power. This dissertation contributes some information critical to understand the efficient way nature converts energy through the use of enzymes, in this case the bovine cytochrome bc1 complex. The results provide various structural and thermodynamic driving factors including the computed pKa values for ionizable amino acid side chains near the catalytic Qo and Qi sites and for the histidines coordinating the Iron-Sulfur Cluster (ISC) (chapter 2). Different binding geometries of QH2 near the Qo site (chapter 3) and of UQ near the Qi site (chapter 4) are also studied computationally. The information from this dissertation not only has mechanistic implications that support several current hypotheses and but should also stimulate more experimental and computational work on the cyt bc1 complex in order to achieve a more thorough understanding of the CEPT reactions carried out by the cyt bc1 complex.

Chapter 1 gives an overall introduction including [1] the theoretical framework of the CEPT reactions and the challenges of studying such reactions in general and in biological systems; [2] the biological background on the mitochondrial electron transport chain, where the cyt bc1 complex is located; [3] the structures, functions, malfunctions and their consequences for CEPT in the bovine cyt bc1 complex, probably the most well-characterized biological CEPT system; [4] the modified Q-cycle that describes the cyt

bc1 complex; and [5] the controversies surrounding the different proposed mechanisms of QH2 oxidation and UQ reduction near the Qo and Qi sites, respectively.

Chapter 2 reports the computed pKa value of 5.1 for Glu271 near the Qo site. The result is in good agreement with the experimentally reported pKa values of 5.2 and 5.7, measured by Covian et al. (1) from the effects of pH on the binding affinity of the quinone analogues decylbenzoquinone and decylbenzoquinol, respectively. Our results support these authors' hypothesis that an acidic amino acid residue, probably Glu271, near the Qo site has to be deprotonated for the QH2 oxidation to occur. In chapter 2, we also report that the computed pKa values for His201, Asp228 and Lys227 near the Qi binding site are 6.7, 3.9 and 8.9, respectively. Near the physiological pH, His201 is singly protonated and capable of playing the role of hydrogen bond donor to the UQ. On the other hand, Asp228 near pH 7 is deprotonated and thus cannot act as a hydrogen bond donor in a direct hydrogen bond to the UQ. However, extensive water accessibility to the site implies that Asp228 very likely forms a water-bridged hydrogen bond to the UQ. The computed pKa value for Lys227 is 8.9, which provides direct evidence that Lys227 is protonated in the protein at pH near 7. However, a pKa shift of -1.5 pKa units compared to a free lysine in water implies that Lys227 is buried in the protein and not likely to play the role of fetching water molecule(s) from solvent to the Qi site, suggested suggestion made by Gao et al. (2). The computed pKa values of residues near the Qi site provide direct evidence for the protonation states of the His201 and Asp228. Together with the binding geometries from dynamics simulations, our results (described in Chapter 4 and briefly discussed below) support the roles of His201 and Asp228 in substrate binding near the Qi site.

Chapter 2 also reports the computed pKa values for the histidine ligands to the ISC near the Qo site. . Our computed pKa values for His141 (7.8 ± 0.5) and His161 (9.1 ± 0.6) are in excellent agreement with the experiment pKa values of 7.63 ± 0.15 and 9.16 ± 0.28 for the two histidines, obtained by measuring the redox potentials of the ISC of the ISP as a function of pH (3). The pKa values of these two iron-ligated histidines are of interested because of their implications for the different CEPT mechanisms at the Qo site, as explained in Chapter 1.Thus pKa values for these histdine residues were studied experimentally (3) and computationally (4). The previously calculated pKa values of 6.9 and 8.8 were obtained from calculations with the Density Functional Theory (DFT) treatment for the ISC and a continuum electrostatics (CE) environment to model the protein (4). Because of the nature of the DFT-CE method and the experimental method mentioned above, neither study was able to assign pKa values to either of the individual hisditines, His141 and His161.

In addition to the problem of assigning individual pKa values to His141 and His161, Crofts et al. proposed a sequential mechanism for the CEPT reactions near the Qo site, with His161 as the first proton acceptor (5-7). Under this hypothesis, a deprotonated His161 near physiological pH is required for the QH2 oxidation to occur. Therefore, it is tempting to assign the lower pKa value (pKa ~7) to His161 and not His141. However, there has been no direct evidence that His161 is indeed deprotonated in the protein and or that His161 must be deprotonated in order to initiate the QH2 oxidation. This work unambiguously assigns pKa values to His141 (7.8±0.5) and to His161 (9.1 ± 0.6) for the first time. Structural analysis of the dynamics trajectory also shows that the sulfur atom of Cys160 moves within hydrogen bonding distance of the epsilon hydrogen of His161

and helps to stabilize His161 in the protonated form. Although this work reports results that are in disagreement with the hypothesis by Crofts et al., we hope to stimulate workers in the field to perform more work to measure and compute the individual pKa values of these iron-ligated histidines in order to provide more information regarding the mechanism(s) of QH2 oxidation at the Qo site. We suggest mutations of residues Cys160 to amino acids with different side chain charge states (acidic residues, basic residues and non-polar residues) to affect the His161 pKa. We also suggest FEP calculations using hybrid Quantum Mechanic/Molecular Mechanics (QM/MM) to compute the difference free energy changes upon deprotonation of the hisditines coordinated to the ISC, in water and in the protein. Such calculations should be able to model polarizability changes upon deprotonation of the histidine(s), a physical effect omitted from the force fields used in the current work. Furthermore, the computed pKa values reported in this work are done for the oxidized ISC. Similar calculations can be done on the reduced ISC to study the pH dependent redox potential of the Rieske ISP as well as to provide information regarding the protonation states of the amino acid chains after the electron transfer from QH2 to the ISC.

Chapter 3 describes results for the Qo binding geometry simulations. We observe that [1] the hydrogen bond between a ubiquinol model and the deprotonated His161 side chain of the oxidized ISP is not maintained during MD simulation; [2] the direct hydrogen bond between a ubiquinol model and deprotonated Glu271 carboxylate oxygen is also not maintained; [3] *water-mediated hydrogen bonding* between a ubiquinol model and the deprotonated Glu271 side chain remains for part of the simulation, but break when the Glu271 side chain rotates out of the Qo pocket and toward a position near heme bL (as

suggested by Crofts et el. (5, 6, 8)). Our results therefore support kinetic studies by Covian et al. (1) and EPR spectroscopic measurements by Cape et al. (9) implying that His161 does not stabilize binding of the QH2 substrate. Our simulations also agree with Crofts's proposal that the Glu271 side chain indeed rotates out of the Qo binding pocket (6). Calculated structures show that non-polar contacts to the QH2 model from hydrophobic, aromatic, and aliphatic amino acid residues form the Qo pocket that captures QH2.

This work tests the hypothesis that QH2 binds to the Qo site of the cyt bc1 complex near the same site where stigmatellin (SMA) was observed in X-ray diffraction strucutres (5, 7, 8). These proposed binding geometries for QH2 would place one hydroxyl group of QH2 within a hydrogen bonding distance of His161and the other hydroxyl group of QH2 within a hydrogen bonding distance of Glu271. These binding geometries would presumably allow His161 and Glu271 to serve as proton acceptors in the QH2 oxidation (5, 8). Our results show that the putative hydrogen bonds between a deprotonated His161 and the QH2 model is not maintained in the MD simulations. Together with the computed pKa value of 9.1 ± 0.6 for His161 in the protein environment (chapter 2) i.e., only a very small fraction ($\sim 10^{-9}$) of the His161 is actually in the deprotonated form, our result argue strongly against a deprotonated His161 serving as the initial proton acceptor in QH2 oxidation. Similar binding geometry simulations should also be done for different ubiquinol radical intermediates (negative and neutral) proposed to appear during QH2 oxidation. Together with further pKa calculations (see future work for Chapter 2), the information from these simulations will provide a more complete picture for the mechanism of CEPT reaction at the Qo site.

Chapter 4 tests two possible UQ binding geometries (see Figure 4.1.3) previously

reported in both yeast and bovine cyt bc1 structures (with less than 50% occupancy for

UQ). Current published X-ray diffraction structures for bovine cyt bc1 complex from two

different groups showed two hydrogen bonds stabilized the UQ at the Qi site however,

they had a disagreement. In 2003, Gao et al. suggested a substrate ligand binding

geometry involving two water-mediated hydrogen bonds from His201 and Asp228 to the

two carbonyl oxygen atoms at positions 1 and 4 on the benzoquinone ring (2). In 2005,

Huang et al. (10) suggested a direct hydrogen bond from His201 to the UQ instead of the

water-mediated hydrogen bond. Our results show that a direct hydrogen bond from

residue His201 to the carbonyl oxygen atom on the UQ and a water-mediated hydrogen

bond to Asp228 are maintained. Our results support the structure reported by Huang et

al.(10) with a direct hydrogen bond from His201 to the UQ. No stable water-mediated

hydrogen bond from His201 to the UQ, as suggested by Gao et al. (2), is observed in our

simulations. In the two different binding geometries tested, the water-mediated hydrogen

bonds from Asp228 to the UQ model are maintained. We suggest that the bridging water

molecule(s) can act as the proton donor for the UQ reduction at the Qi site. Our results

present a challenge for experiments to test the role of water as a proton donor in the

water-mediated hydrogen bond between Asp228 and UQ. Computational studies to

provide more evidence for the role of water as proton donors are also challenging, yet

may be done using QM/MM simulations to map the potential of mean force along several

reaction coordinates moving the proton from different water molecules to the UQ.

In summary, this work addresses several critical points regarding the structural and

thermodynamic driving factors for the CEPT reactions of the bovine cyt bc1 complex,

including the protonation equilibria of amino acid side chains near the catalytic Qo and Qi sites and the different possible binding geometries of QH2 and UQ models at the Qo and Qi sites, respectively. Our results support some current hypotheses and also raise multiple questions that we hope will stimulate more experimental and computational work to study the cyt bc1 complex, as well as CEPT reactions in this and other proteins.

References

1. Covian R, Moreno-Sanchez R. Role of protonatable groups of bovine heart bc1 complex in ubiquinol binding and oxidation. Eur J Biochem. 2001;268(22):5783-90.

2. Gao X, Wen X, Esser L, Quinn B, Yu L, Yu C, et al. Structural basis for the quinone reduction in the bc1 complex: A comparative analysis of crystal structures of mitochondrial cytochrome bc1 with bound substrate and inhibitors at the qi site. Biochemistry. 2003;42(30):9067-80.

3. Link TA, Hagen WR, Pierik AJ, Assmann C, Von Jagow G. Determination of the redox properties of the rieske [2Fe-2S] cluster of bovine heart bc1 complex by direct electrochemistry of a water-soluble fragment. Eur J Biochem. 1992;208(3):685-91.

4. Ullmann GM, Noodleman L, Case DA. Density functional calculation of pKa values and redox potentials in the bovine rieske iron-sulfur protein. JBIC, J Biol Inorg Chem. 2002;7(6):632-9.

5. Crofts AR, Hong S, Ugulava N, Barquera B, Gennis R, Guergova-Kuras M, et al. Pathways for proton release during ubihydroquinone oxidation by the bc1 complex. Proc Natl Acad Sci U S A. 1999;96(18):10021-6.

6. Crofts AR, Barquera B, Gennis RB, Kuras R, Guergova-Kuras M, Berry EA. Mechanism of ubiquinol oxidation by the bc1 complex: Different domains of the quinol binding pocket and their role in the mechanism and binding of inhibitors. Biochemistry. 1999;38(48):15807-26.

7. Crofts AR. The cytochrome bc1 complex: Function in the context of structure. Annu Rev Physiol. 2004;66:689,733, 4 plates.

8. Crofts AR, Lhee S, Crofts SB, Cheng J, Rose S. Proton pumping in the bc1 complex: A new gating mechanism that prevents short circuits. Biochim Biophys Acta, Bioenerg. 2006;1757(8):1019-34.

9. Cape JL, Bowman MK, Kramer DM. A semiquinone intermediate generated at the qo site of the cytochrome bc1 complex: Importance for the q-cycle and superoxide production. Proc Natl Acad Sci U S A. 2007;104(19):7887-92.

10. Huang L, Cobessi D, Tung EY, Berry EA. Binding of the respiratory chain inhibitor antimycin to the mitochondrial bc1 complex: A new crystal structure reveals an altered intramolecular hydrogen-bonding pattern. J Mol Biol. 2005;351(3):573-97.